Electromagnetically induced modification of metal optical properties

by

Peyman Feizollah

B.S., University of Isfahan, Iran, 2008

M.S., University of Tehran, Iran, 2012

M.S., Kansas State University, USA, 2018

AN ABSTRACT OF A DISSERTATION

submitted in partial fulfillment of the
requirements for the degree

DOCTOR OF PHILOSOPHY

Department of Physics
College of Arts and Sciences

KANSAS STATE UNIVERSITY
Manhattan, Kansas

2021

Abstract

The reflection of light from a metal film is among the most fundamental and well-understood effects in optics. If the film thickness is greater than the wavelength, reflection is explained in simple terms with the electromagnetic boundary conditions. For film thickness much less than the wavelength, reflection is incomplete and more exotic physical effects become possible. This is especially so if the light illuminating the film is pulsed at the femtosecond time-scale. In this work, a new phenomenon is proposed where few-femtosecond laser pulses temporarily modify a thin metal film's optical properties. By casting a pulsed standing-wave pattern across the metal surface, conduction electrons are redistributed to create temporary regions of partially enhanced or depleted density. This constitutes a temporary change to the conductivity of the metal, and thus, a change to the transmittance and reflectance of the film. In regions where the density is enhanced (depleted), the transmittance is decreased (increased). The process is possible because the period of action of the applied electric field is shorter than the relaxation time for the conduction electrons. An experiment is conducted that tests the concept by measuring the change in reflectance and transmittance for films with thickness ranging from 20–400 Angstroms. A pair of calibrated photodiodes are used to monitor the reflection and transmission modulation of the sample. The data is collected over many laser pulses and is averaged which cancels the random power fluctuation effects of the laser.

Our findings show that the film's transmittance decreases only when the standing-wave pattern is present. In other words, the metal sample is found to be less transparent hence a "better" conductor in the presence of the conditioning beams compared to when there is no standing wave on the sample. As the pulse length of the pattern is increased, or as the film thickness is increased, these changes disappear. To gain further insight, the

Drude free-electron model is used to develop a theoretical description for the process, which qualitatively agrees with the observed changes in reflectance and transmittance.

Electromagnetically induced modification of metal optical properties

by

Peyman Feizollah

B.S., University of Isfahan, Iran, 2008

M.S., University of Tehran, Iran, 2012

M.S., Kansas State University, USA, 2018

A DISSERTATION

submitted in partial fulfillment of the
requirements for the degree

DOCTOR OF PHILOSOPHY

Department of Physics
College of Arts and Sciences

KANSAS STATE UNIVERSITY
Manhattan, Kansas

2021

Approved by:

Major Professor
Matthew J. Berg

Copyright

Abstract

The reflection of light from a metal film is among the most fundamental and well-understood effects in optics. If the film thickness is greater than the wavelength, reflection is explained in simple terms with the electromagnetic boundary conditions. For film thickness much less than the wavelength, reflection is incomplete and more exotic physical effects become possible. This is especially so if the light illuminating the film is pulsed at the femtosecond time-scale. In this work, a new phenomenon is proposed where few-femtosecond laser pulses temporarily modify a thin metal film's optical properties. By casting a pulsed standing-wave pattern across the metal surface, conduction electrons are redistributed to create temporary regions of partially enhanced or depleted density. This constitutes a temporary change to the conductivity of the metal, and thus, a change to the transmittance and reflectance of the film. In regions where the density is enhanced (depleted), the transmittance is decreased (increased). The process is possible because the period of action of the applied electric field is shorter than the relaxation time for the conduction electrons. An experiment is conducted that tests the concept by measuring the change in reflectance and transmittance for films with thickness ranging from 20–400 Angstroms. A pair of calibrated photodiodes are used to monitor the reflection and transmission modulation of the sample. The data is collected over many laser pulses and is averaged which cancels the random power fluctuation effects of the laser.

Our findings show that the film's transmittance decreases only when the standing-wave pattern is present. In other words, the metal sample is found to be less transparent hence a "better" conductor in the presence of the conditioning beams compared to when there is no standing wave on the sample. As the pulse length of the pattern is increased, or as the film thickness is increased, these changes disappear. To gain further insight, the

Drude free-electron model is used to develop a theoretical description for the process, which qualitatively agrees with the observed changes in reflectance and transmittance.

Table of Contents

List of Figures

Acknowledgments

As far as I remember, the first time I heard about laser, I was in elementary school. I became fascinated by whatever I could understand, which was not much, from what I was watching. So, I should start acknowledging people at least from back then. There is no way I can mention everyone by name here. I appreciate all of my friends, the ones that are mentioned by name and the ones that are not.

First and foremost, I would like to thank my PhD advisor Professor Matthew J. Berg, who very kindly agreed to be my mentor. Before he was my advisor, I had the chance of having him as my Electrodynamics Professor. Classical Electrodynamics being one of my favorite topics, I really enjoyed and learned a lot sitting in the "ED" lectures. Matt is truly interested in and fascinated by the topic, and that means a lot considering the fact that I think teaching Electrodynamics with as much detail as we saw in class, is not a trivial task at all.

During my undergraduate, I learned about holography. I was interested in recording holograms back then, which did not happen until almost the end of my undergraduate studies. I think it was the last summer when I was an undergraduate that I spent a lot of time in a lab trying to record analog holograms. This very fun effort was successful, and I managed to record a few holograms, including the best one, which was of the coins of the Iranian currency. Back then, I knew some about digital holography, but I never got to work on it. After joining Matt's group, I worked on digital holography for a short time. We explored a lot of topics during this short time, which helped me learn and have some experience with digital holography and its challenges. Ironically, the best hologram I recorded during this time was also from a coin, this time part of a New York state quarter. I would like to thank Matt for the useful and enjoyable discussions that resulted in me

learning about digital holography, help and support so that we can figure out what I was doing wrong, and all the encouragement and excitement when I was doing something right.

Then, I started working on the project that is presented in this dissertation. During the work on this project, Matt and I had a lot of discussions about the idea behind project and how to design and perform the experiment. I needed a lot of guidance in order to understand the theoretical idea behind the project, which Matt gave it to me patiently. Also, the discussions we had about designing the experiment were great opportunities for me to learn detailed and useful experimental techniques and tricks.

I would also like to thank my colleagues in Matt's group. During this time, I worked with Dr. Justin Jacquot, Ramesh Giri, Peter Anderson, Michael D. Sanchez, and Dr. Osku Kemppinen in the lab and in the field. This was related to the digital holography research of our group. Working and discussing different aspects of the projects helped me learn more about their research.

I got my second Master's degree in AMO physics working in Professor Itzik Ben-Itzhak's group at KSU. I gained a lot of experience during this time that helped me during my PhD work. I learned from Itzik how to think about performing an experiment, how to make the experiments work in the lab, and how to analyze and think about the analyzed data collected in the lab. When I decided to leave the group, he was supportive and tried to make the transition a smooth process. I would also like to thank Professor Eric Wells for all the fun time in the lab working on different projects.

During my first Master's degree in atomic and molecular physics in the department of physics of the University of Tehran, I was a member of Professor Atamalek Ghorbanzadeh's group. We had many scientific and nonscientific discussions in the lab over tea. We had a lot of fun in the lab. I would like to thank my friends and colleagues from that time. A special thanks to Ali Rastegari, Amir Mahdian, and Professor Arazi Siabi that were graduate students at the same time. Ali and I worked countless hours on a pulsed CO_2 laser. Ali, Amir, Araz, and I had a lot of interesting conversations and discussions.

During my undergraduate in the University of Isfahan, I was inspired by Professor Mahmood Soltanolkotabi and Professor Ahmad Kiasatpour, RIP. Working in the laser and spectroscopy lab under the supervision of Professor Soltanolkotabi and spending many hours working with different telescopes under the supervision of Professor Kiasatpour shaped my career and made me sure that I love spending time in a lab. During this time, learned from and worked with many people. I want to especially thank my friend Professor Ardalan Armin. He was a Master's student back then. He saw my interest in experimental physics and let me help him in his research. It was fun working with him and trying to grasp as much as I could.

A special thanks to the committee members for their time and effort to help me in my project. I got useful comments from Professor Cosmin Blaga, Professor Uwe Thumm, and Professor Shuting Lei during my preliminary oral exam, which I used to proceed with the project. I would like to thank the outside chair Professor Scott Thompson.

I would like to thank my family for their love and support. A very special thanks to my beloved wife Bethany for your constant love, encouragement, and support. I cannot wait for us to be "real people" someday soon. My dad Razagh, RIP, was always encouraging me to pursue what makes me happy. My mom, Fati, has always been very supportive and encouraging. Going to a different country for pursuing your dreams is very exciting and challenging. I cannot thank you enough mom for all your support. Thank you Mike, Loretta, Joel, Loni, Pat, and Steve for all the fun we have together. I would like to thank my uncle Fattah, RIP for his love and support. I will always be indebted to you. A special thank to my aunts especially Soheila, Amireh, and Mansoureh. A special thanks to all my cousins, especially Ashkan, an inspiring human being, Arash, Soheil, Soroush, Sahand, Farzad, Pegah, Mehran, and Negar for all the fun we had. I would like to also thank all of my friends that became my family at KSU. A very special thanks to my dear friends Mohammad Zohrabi, Amy Rouinfar, Sajed Hosseini, Dina Zohrabi, Amir Shaghaghi, Ameneh Tavakol, Negar Orangi-Fard, Masoumeh Tavakol, Daniel Brooks, Kanaka Raju

Pandiri, Manasa Thirugnanasambandam, Kimia Alizadeh, and Justin Wright.

I also had many great teachers when I was in high school and before that. I would like to sincerely thank them for all they taught me.

This work was supported by the the Air Force Office of Scientific Research (AFOSR) grant number FA9550-19-1-0078. I would like to acknowledge the program manager Dr. Ali Sayir, for his interesting and challenging questions during the review sessions.

Dedication

Dedicated to my beloved family.

Chapter 1

Introduction

Light-matter interaction is one of the most important phenomena in the universe. It is also broadly used to study nature by us in science and technology. Such interactions are used to study matter using different spectroscopic methods, see for example [1–4], that allow us to understand matter and broaden our understanding of nature.

Another important aspect of light-matter interaction is the possibility of altering and controlling different properties of matter, see for example [5, 6]. Such control can in principle lead to many new technological advancements such as the development of materials with new characteristics, more efficient renewable energy sources, faster optical communications, and many other possibilities.

From a practical point of view, recording information on a CD, DVD, or Blu-ray is done by using a laser light that "writes" the information on the storage device. This results in a permanent change in the solid used. Another laser is then used to read the recorded data. This is a common use of laser light to alter solids for a practical use, such as watching a movie or playing Gears of War! Similarly, we use two laser beams to alter the properties of a solid and then monitor the change using another laser beam.

The focus of this dissertation is on using light in order to temporarily modify the properties of solids. We present a novel idea in order to alter the optical properties of noble metals

using femtosecond (one femtosecond is 10^{-15} or 0.000000000000001 of a second) laser pulses. We call this phenomenon *electromagnetically induced modification* (EIM) of metal optical properties. A proof of principle experiment and its results are also presented to discuss the possibility of such modification of optical properties of metals.

In the simplest model to describe metals, they are considered as positive ions and a number of free electrons. In other words, the electrons in a metal form a "sea" of free electrons [7, 8]. If these electrons are disturbed by any means, say an electric field applied to the two sides of a metal rod, they tend to go to their relaxed state very rapidly. This relaxation time for electrons in metals is of the order of a few tens of femtoseconds [7–9]. The fact that the relaxation time for metals is so short limits the light source we can use for our study. In other words, in order to observe any effect on the optical properties of metal in time domain, we should use a laser with a shorter pulse duration than the relaxation time. This is why ultrafast lasers are used to perform the experiment.

Ultrafast laser pulses have been extensively used in order to study and manipulate properties of matter in the past few decades, see for example [10–31] and references within. The interaction of few cycle laser pulses and solid materials is of particular interest. One of the interesting aspects of manipulating solids is the possibility of processing signals on an ultrafast timescale [10]. Different methods have been used in order to modify the properties of conductors, semiconductors, and insulators. In some of these studies, a sample is irradiated by ultrafast pulses, and a time-dependent change in its properties due to thermalization of the electron distribution is observed [19–32]. This redistribution of the electron density is due to the intraband transitions and is on the timescale of a few hundred femtoseconds to a few picoseconds.

On the other hand, faster modification of the properties of a sample have been observed to occur when few cycle lasers are used [10–16]. This process relies on interband transitions of electrons. For such excitation to happen, the wavelength and the intensity of the laser should be chosen carefully.

The experimental results presented here show that EIM decreases the transmission of gold and platinum temporarily. We hypothesize that EIM depends only on the free electrons of a thin-film metal at room temperature. We discuss that no significant presence of interband transitions is expected in our experimental scheme, but an effect that can be observed at a timescale of $\sim$10 fs is present in the results. This effect could be applied, in principle, using any wavelength of light for which the metal film is reflective as long as interband transitions do not occur. A classical model is also developed in order to describe EIM. We show that this classical model both predicts EIM and is in qualitative agreement with the experimental observations.

Chapter 2

Theoretical background

In order to discuss the experimental and theoretical aspects of EIM in metals, we need to review a few topics, which are key to understand later concepts. We start with a short description of ultrafast lasers and the challenges of working with them, then briefly explain the characterization method used to measure the laser pulse duration. We then briefly discuss how noble metals are described in a classical picture. Lastly, a brief description of the main features of plasmonic effects are presented so that a comparison between EIM and plasmonic effects can be considered. Note that we will not talk about these topics in detail, so looking at the references presented in this chapter is strongly recommended for more in depth information.

2.1 Ultrashort laser pulses

Different types of lasers have been used for research and industry purposes over the past 60 years [33–35]. Continuous-wave (CW) lasers can have extremely narrow bandwidth [33–35]. On the other hand, pulsed lasers can create bursts of light with pulse durations of just a few femtoseconds, which corresponds to a very large spectral bandwidth [36, 37]. Both types of lasers, which are on very opposite sides of the spectrum of the types of lasers, have

significant applications in the world of science and technology in many fields. I do not think anyone can walk into a room in which there are not a few lasers in use, or have been used in different devices or to make one of the objects around. Although the history of lasers and their development is a fascinating topic, I refer you to some references (and references therein) for more information.

For the purpose of studying EIM, it is essential for the laser to be pulsed and have ultrashort time duration, of the order of less than 20 fs. The importance of having short pulses will be explained. Ultrafast lasers and the challenge of keeping the laser pulses short [36, 37] after many optical elements, such as mirrors and beamsplitters, and traveling in air is briefly discussed here.

2.1.1 An ultrafast laser system

Ultrafast lasers have a broad spectral bandwidth, from tens to hundreds of nanometers. This opens up the possibility for these lasers to have very short pulses, of the order of a few to few hundred femtoseconds. In order to understand the relation between spectral and temporal profile, we can write the electric field of an ultrafast laser as [36, 37]

$$E(t) = \frac{1}{2\pi} \int_{-\infty}^{\infty} E(\omega) e^{i\omega t} \, d\omega \tag{2.1}$$

in the time domain. In the frequency domain, we have

$$E(\omega) = \int_{-\infty}^{\infty} E(t) e^{-i\omega t} \, dt. \tag{2.2}$$

For a Gaussian temporal $E(t)$ profile of a laser the time bandwidth product is

$$c \frac{\Delta\lambda}{\lambda^2} \tau \geq 0.441, \tag{2.3}$$

where c is the speed of light, λ is the central wavelength of the laser, $\Delta\lambda$ is full width at half maximum (FWHM) [36, 37] of the the spectral bandwidth of the laser, and τ is the FWHM pulse duration. Equation (2.3) limits the shortest possible pulse for a spectral bandwidth of $\Delta\lambda$, which is called the Fourier transform limited (FTL) laser pulse. In an FTL pulse, all of the frequency components of the laser reach a certain point in space at the same time. For example, the laser used in our experiments has a central wavelength of ∼790 nm with a spectral bandwidth of ∼124 nm. This means that the shortest output pulse from this laser with a Gaussian temporal profile is ∼7.4 fs. However, keeping such a pulse short after propagating in air and being reflected off or transmitted through optical elements is challenging. This is because of the dependence of the refractive index on the light wavelength, i.e., dispersion. How one can keep such pulses short is explained later.

2.1.2 Dispersion of ultrafast laser pulses

Consider white light going through a prism. We know that this results in the different colors of the light being separated spatially. This is because of the wavelength dependent refractive index, which is larger for shorter wavelength components of the light. The same concept is true for ultrafast pulses. The dispersion of all the materials in the visible region, such as optical elements used in a setup or even air, makes the pulses longer. Let's take the example of a short-pulse laser with central wavelength of 790 nm propagating in air. As mentioned before, the refractive index value increases as the light wavelength decreases. This means that longer wavelength components travel faster than the shorter wavelength components ($v = \frac{c}{n}$, where v is the speed of light in air and n is the refractive index) resulting in a longer pulse than the initial FTL laser pulse.

A laser pulse that is not FTL is called a chirped pulse. If the longer wavelength components, lower frequency, come before the shorter wavelength, higher frequency, in time, this pulse is called positively-chirped [36, 37]. If the order is swapped, then we have a negatively-chirped laser pulse.

To understand the dispersion effect in chirping the laser pulses, we can look at the problem from a more mathematical point of view. The electric field of a laser pulse after passing thorough a medium like air or a piece of glass with a length of L can be written as [36, 37]

$$E_{\text{out}}(t) = \frac{1}{2\pi}\int_{-\infty}^{\infty} E_{\text{in}}(\omega)e^{i\omega t}e^{-i\beta(\omega)L}\,d\omega, \tag{2.4}$$

where $E_{\text{in}}(\omega)$ is the electric field of the pulse before the medium in frequency domain, $E_{\text{out}}(t)$ is the electric field of the pulse after the medium in time domain, ω is the angular frequency of the laser, and $\beta(\omega)$ is spectral phase accumulated by the pulse in the medium per unit length. Taylor expansion of $\beta(\omega)$ helps us understand the effect of the material on the laser pulse

$$\beta(\omega) = \beta(\omega_0) + \frac{\partial\beta}{\partial\omega}(\omega-\omega_0) + \frac{1}{2!}\frac{\partial^2\beta}{\partial\omega^2}(\omega-\omega_0)^2 + \frac{1}{3!}\frac{\partial^3\beta}{\partial\omega^3}(\omega-\omega_0)^3 + ... \tag{2.5}$$

We can write Eq. (2.5) as

$$\beta(\omega) = \beta_0 + \beta_1(\omega-\omega_0) + \frac{1}{2!}\beta_2(\omega-\omega_0)^2 + \frac{1}{3!}\beta_3(\omega-\omega_0)^3 + ..., \tag{2.6}$$

where $\beta_n = \frac{\partial^n\beta}{\partial\omega^n}$ is the nth order dispersion. Consider the case in which only the first two terms in Eq. (2.6) are nonzero. In this case, it is easy to see that

$$E_{\text{out}}(t) = E_{\text{in}}(t-\beta_1 L) \tag{2.7}$$

So, the output pulse is the same as the input but delayed. This does not change the pulse characteristics. Considering the first three terms in Eq. (2.6), we find the group velocity

$$v_g = (\frac{d\beta}{d\omega})^{-1} = \frac{1}{\beta_1 + \beta_2(\omega-\omega_0)}. \tag{2.8}$$

If we calculate the time difference for each frequency component ω with respect to the

central frequency ω_0 to travel the length L, we find

$$\Delta t = t(\omega) - t(\omega_0) = \frac{L}{v_g(\omega)} - \frac{L}{v_g(\omega_0)} = \beta_2 L(\omega - \omega_0). \tag{2.9}$$

In equation (2.9), β_2 is the group velocity dispersion (GVD) and has the unit of fs^2/m. GVD is the group delay dispersion (GDD) per unit length. The group delay dispersion is presented in the unit of fs^2. If no GDD or higher order dispersion is added to the laser pulses, as discussed before they are called FTL, as shown in Fig. 2.1 (a).

For visible light in most materials, β_2 is positive [36, 37]. This means that the lower frequency components, longer wavelength, travel through the distance L faster, and the higher frequency components travel slower compared to ω_0. This results in a time dependent arrival of the frequency components which is called positively-chirped laser pulses, as seen in Fig. 2.1 (b). On the other hand, if the lower frequency components travel slower and the higher components faster, then the pulses are called negatively-chirped pulses, as shown in Fig. 2.1 (c).

2.1.3 Dispersion compensation

There are a few methods used in order to compensate for the positive GDD added to the laser pulses due to propagation in air and optical elements [36, 37]. Prism-based compressors, grating-based compressors, or chirped mirrors are often used for this purpose. Prism- and grating-based compressors are extremely sensitive and hard to align. These compressors are useful if one wants to have the capability of changing the GDD over a relatively wide range. For example, if multiple experimental groups use a laser to do their experiments, and their setups are located in different places in a lab, having such a compressor is crucial so that the shortest pulse is available to different groups, if pulse duration is an important factor for their experiments of course. This allows them to also have positively- and negatively-chirped pulses if needed.

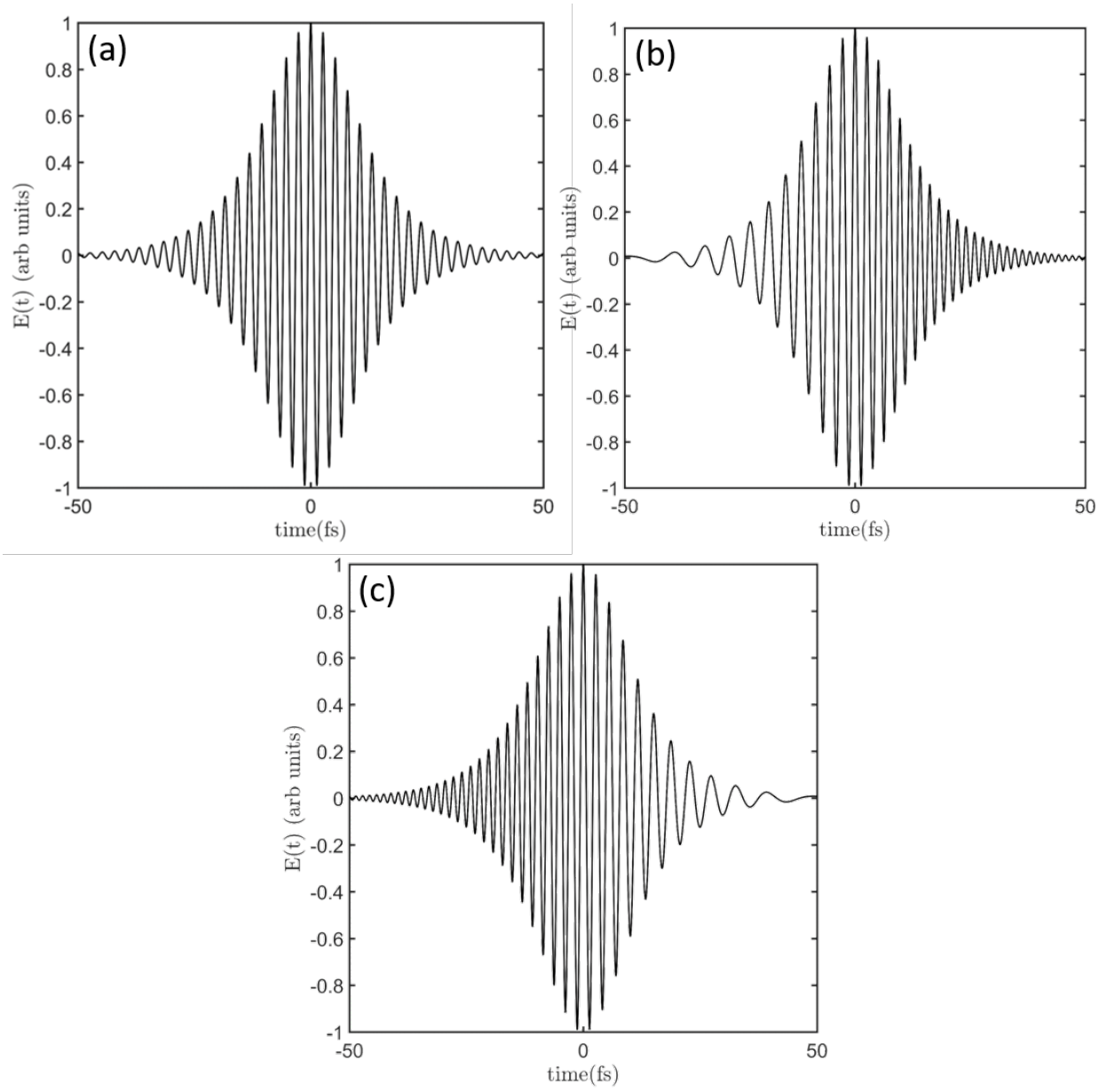

Figure 2.1: Electric field of (a) FTL, (b) positively-chirped , and (c) negatively-chirped laser pulses as a function of time.

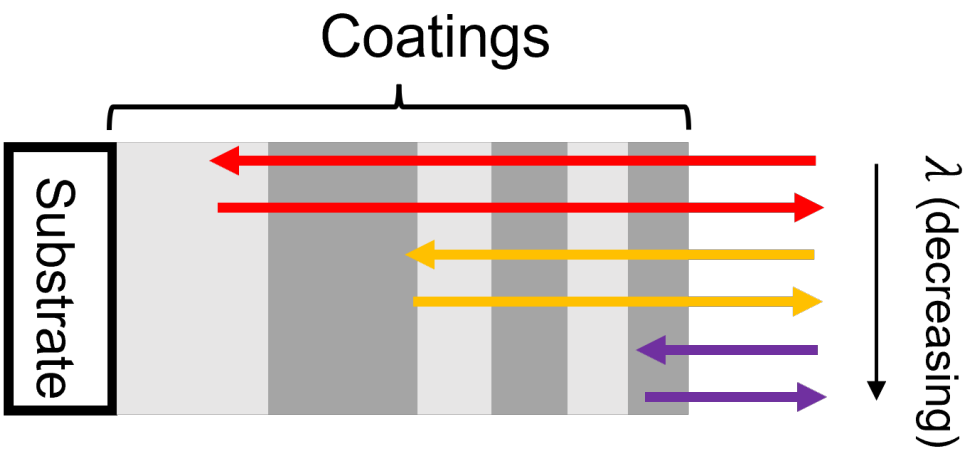

Figure 2.2: Schematic of the layers of a chirped mirror. Longer wavelengths of the spectrum penetrate deeper into the layers, and hence the chirped mirror introduces negative GDD to the laser pulse.

It is also possible to use chirped mirrors [38] in order to compensate for the GDD. They are a set of mirrors in which the penetration depth into the many layers of the mirror coating depends on the wavelength of the light. They are designed such that the longer wavelengths of the spectrum travel deeper in the coating layers compared to the shorter wavelength, as seen in Fig. 2.2. This means that the longer wavelengths travel longer compared to the shorter wavelength, which results in a negative GDD added to the laser pulse. By designing the setup carefully, and figuring out the proper number of bounces off the chirped mirrors, one can compensate for the positive GDD added to the laser pulses in the beam path.

2.1.4 Temporal characterization of ultrashort laser pulses

When one takes a picture of a moving object, the shutter of the camera should open and close faster than the object motion to have a clear photo. We all have seen those interesting videos showing how a bullet penetrates an apple or a water droplet falling into a bowl full of water, as seen in Fig. 2.3. In all of these images or videos, the camera shutter is faster than the event.

Figure 2.3: An image of a water droplet recorded with a camera fast enough so that the details in the image can be captured.

Cross correlation

The idea is the same for characterizing laser pulses. The temporal profile of an unknown pulse, $I_{\mathrm{un}}(t)$, can be determined if a shorter reference pulse, $I_{\mathrm{r}}(t)$, is available. This can be done by measuring the cross correlation of the intensity of the two pulses.

$$I_{\mathrm{CC}} = \int_{-\infty}^{\infty} I_{\mathrm{un}}(t) I_{\mathrm{r}}(t-\tau) dt. \tag{2.10}$$

The challenge for characterizing ultrashort laser pulses temporally is that a shorter pulse than the unknown pulse might not exist. Ultrashort laser pulses are the shortest temporal phenomena that have been created by mankind. The question is how can we measure such events in time then? The short answer to this question is that it is possible to use the ultrafast laser pulse to measure and characterize itself temporally. This is done by measuring the autocorrelation of the pulses.

Interferometric autocorrelation

We use an interferometric autocorrelator in order to characterize the ultrashort laser pulses used in our experiment. The idea is shown schematically in Fig. 2.4 (a), which is a Michelson interferometer. A beamsplitter divides the input beam in two identical intensity replicas.

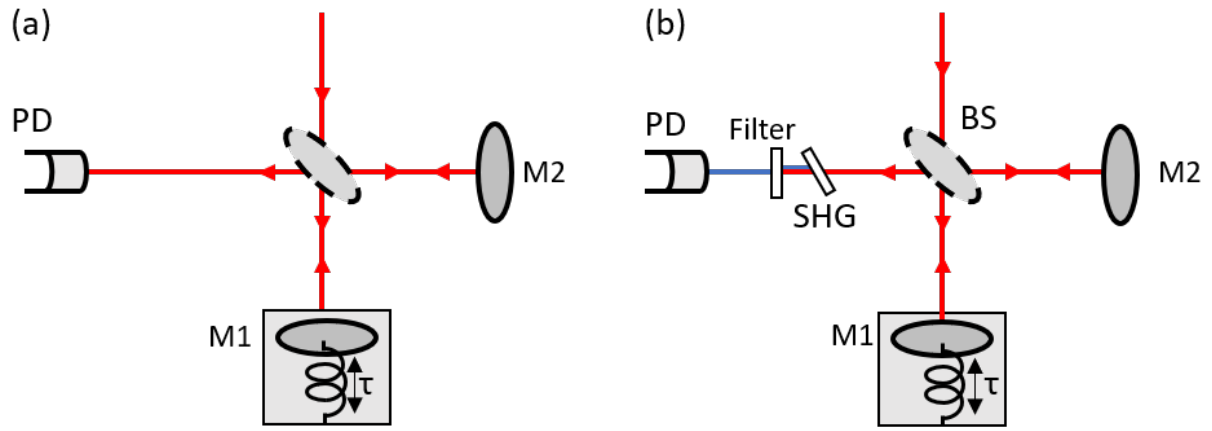

Figure 2.4: Schematic of an interferometric autocorrelator setup. (a) No nonlinear process happens in this case. As discussed in text, this configuration cannot be used to measure the laser pulse duration. (b) The same setup as (a) with the addition of a SHG crystal and a filter to generate and separate second harmonic from the fundamental IR light. This configuration allows us to characterize ultrafast laser pulses temporally.

Then, the delay between the two beams is changed and a signal is recorded using a photodiode. It can be shown that if no nonlinear process is involved in the measurement, the result is always the inverse Fourier transform of the laser spectrum. This is the Fourier-transform limited (FTL) laser pulse duration, which means that the measurement results in the same outcome for an FTL and a longer pulse (chirped) with the same spectral bandwidth.

In order to overcome this issue, a second harmonic generation (SHG) crystal is added right before the photodiode, as seen in Fig. 2.4. The electric field before the SHG crystal is

$$E_{\text{out}} = E(t) + E(t-\tau), \tag{2.11}$$

where τ is the delay between the two arms. The electric field of the second harmonic generated is proportional to the square of the input [36, 37]

$$E_{\text{SHG}} \sim E_{\text{out}}^2 = E^2(t) + E^2(t-\tau) + 2E(t)E(t-\tau). \tag{2.12}$$

So, the intensity of the signal recorded by the photodiode is [36, 37]

$$I_{IAC}(\tau) \sim \int_{-\infty}^{\infty} |E^2(t) + E^2(t-\tau) + 2E(t)E(t-\tau)|^2 dt. \tag{2.13}$$

As the detector is slow compared to the pulse, what is measured by the photodiode is the total time-integrated intensity [36, 37]. This is why we integrate over time in the above equation. Expanding this equation, we get the interferometric autocorrelation (IAC) expression

$$\begin{aligned} I_{IAC} \sim & \int_{-\infty}^{\infty} (I^2(t) + I^2(t-\tau))dt + 4\int_{-\infty}^{\infty} I(t)I(t-\tau)dt - \\ & 2\int_{-\infty}^{\infty} (I(t) + I(t-\tau))E(t)E^*(t-\tau)dt + c.c. + \int_{-\infty}^{\infty} E^2(t)(E^*(t-\tau))^2 dt + c.c. \end{aligned} \tag{2.14}$$

The first term in this equation does not depend on τ. This is the constant background in the interferometric autocorrelation trace. The second term is the intensity autocorrelation term, which varies relatively slowly as a function of τ. The third and fourth terms are interferometric terms, which oscillate relatively fast as τ is scanned. If the interferometric terms are not suppressed by averaging the second harmonic signal, one obtains an interferometric autocorrelation trace.

The electric field and the interferometric autocorrelation trace of a 9 fs FTL laser pulse are shown in Fig. 2.5 (a) and (b), respectively. The ratio between the peak and the background of the trace in an ideal case is 8:1, as can be seen in Fig. 2.5 (b). Note that in the interferometric autocorrelator we use, this ratio is lower. This is mainly because of the imperfections in the optical elements used in the device. So, a ratio of $\sim$ 7:1 is what we usually get from the aligned interferometric autocorrelator. It is also worth mentioning that in the interferometric autocorrelator we use, the nonlinear process is a two-photon absorption that occurs in the photodiode. This results in identical outcome compared with having an SHG crystal.

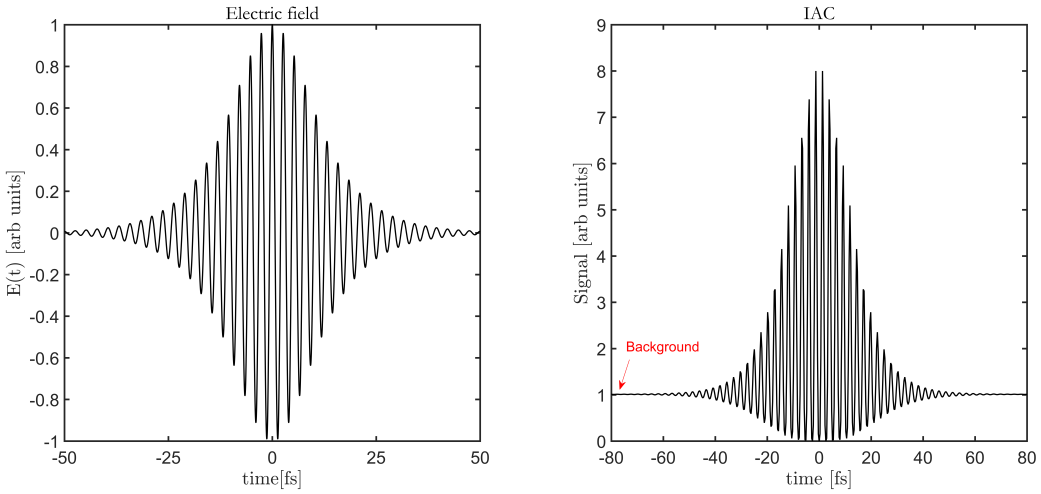

Figure 2.5: (a) and (b): theoretical electric field and interferometric autocorrelation (IAC) trace of a 9 fs FTL laser pulse, respectively.

Interferometric autocorrelation traces do not include any information about the spectral phase of the pulses. However, they show a visual indicator of the presence of chirp in the laser pulse, the intensity autocorrelation behavior at the edges of the trace, which can be helpful in many cases. This is because the temporal coherence of the pulses is shorter than the pulse duration, and so the temporal fringe pattern is not present at the edges of the trace [37]. Figure 2.6 (a) and (b) shows the amplitude of the electric field and interferometric autocorrelation trace of a positively-chirped laser pulses, respectively. One can easily say that the pulses are not FTL by looking at the interferometric autocorrelation trace. Figure 2.6 (c) and (d) show negatively-chirped laser pulses with the same GDD. As one can see, the interferometric autocorrelation traces are identical in both cases, so we cannot find the sign of the chirp using this technique.

To contrast interferometric autocorrelation with intensity autocorrelation, let's assume the last two terms in Eq. (2.14) are averaged out due to for example the experimental method. In this case, what provides us with the temporal information about the laser pulse is the second term, i.e., the intensity autocorrelation. But intensity autocorrelation is

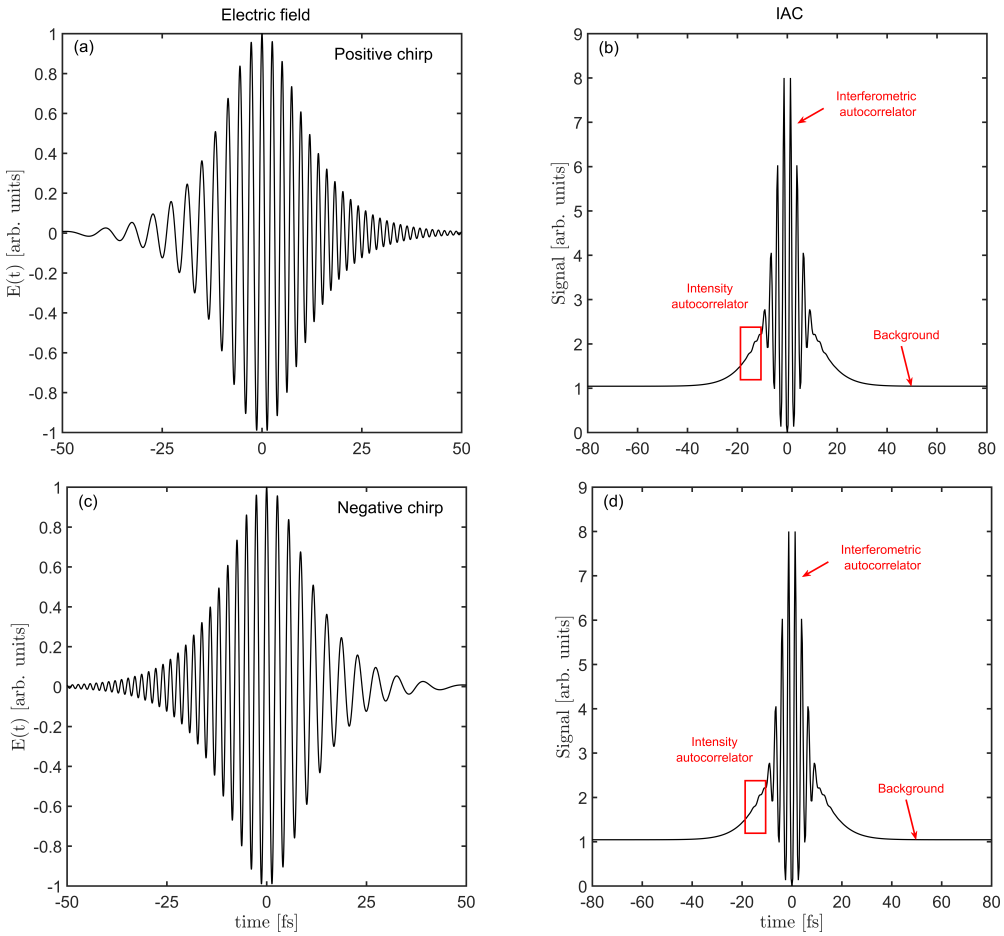

Figure 2.6: (a) and (b): electric field and interferometric autocorrelation trace of a positively-chirped laser pulse. (c) and (d): electric field and interferometric autocorrelation trace of a negatively-chirped laser pulse. Note that the interferometric autocorrelation traces are identical for the two cases. This means that one cannot tell whether the pulses are positively- or negatively- chirped just by looking the the traces.

calculated from the intensity profile of the pulses. This means that it does not include the temporal phase of the laser pulses, see Eq. (2.14). Figure 2.7 (a) and (c) show the electric field of an FTL and a positively chirped laser pulse, respectively. As it can be seen in Fig. 2.7 (b) and (d), the intensity autocorrelation of the two pulses are identical, as the temporal phase of the pulses are ignored in calculating it.

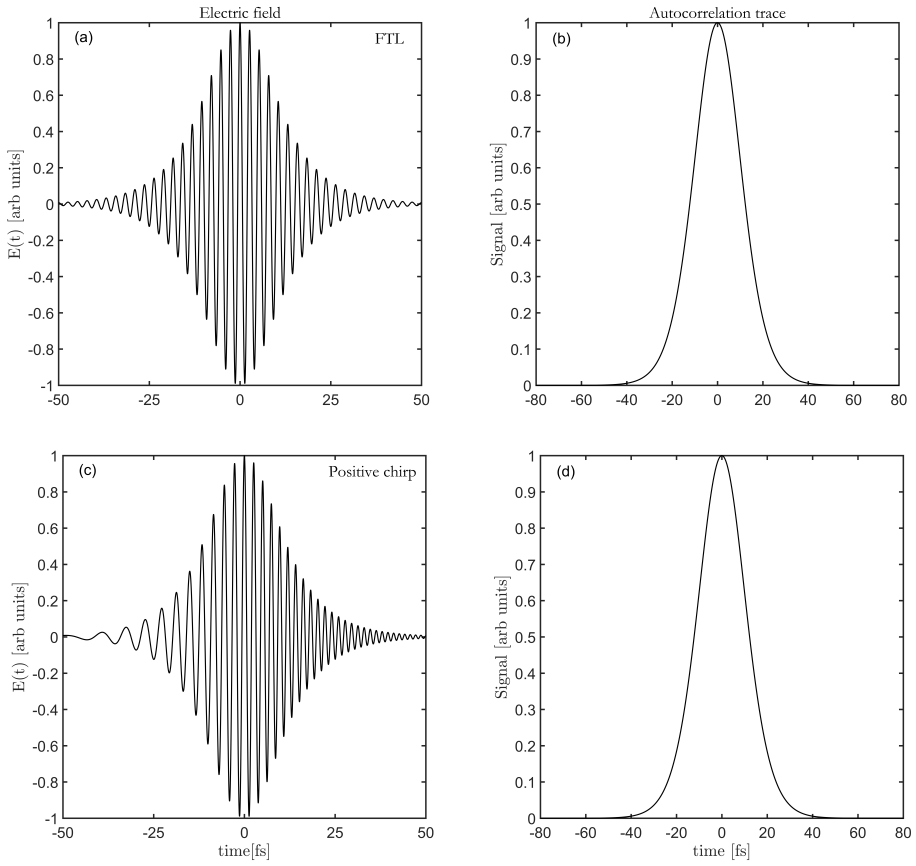

Figure 2.7: (a) and (c): electric field of an FTL and a positively-chirped laser pulse, respectively. (b) and (d): Identical intensity autocorrelation traces of (a) and (c)

2.2 Noble metals

As the metal films used in this work are noble metals, we discuss how the optical properties can be found, see [7, 8, 39–42]. This discussion is mainly from Refs. [41, 42]. Note that all the discussion here is based on the Drude free electron model [7–9], with a correction to include interband transitions, which is a classical picture of describing noble metals. This classical picture is used in the next chapter to present a model for describing EIM.

2.2.1 The role of free electrons

Like other materials, the optical properties of metals are described by their dielectric function, $\epsilon(\omega)$, which is complex for metals [7, 8]. Note that the refractive index of materials depends on the real part, and the absorption depends on the imaginary part. Two main assumptions are used to describe metals interacting with the electric field of a laser light. The first one is that conduction electrons move freely, and the second one is that interband excitation processes are possible. As will be discussed, the wavelength or the intensity of the light should be carefully chosen for the interband transitions to occur.

In this picture, which is the Drude free electron model [7–9], the electric field results in a displacement of electrons by $\mathbf{r}$ giving a dipole moment $\mathbf{d} = e\mathbf{r}$, where e is the charge of electron. The sum of all the dipole moments gives the macroscopic polarization per volume

$$\mathbf{P} = n\mathbf{d} = ne\mathbf{r}, \tag{2.15}$$

where n is the density of electrons. In order to find $\mathbf{P}$, we should find $\mathbf{r}$. Assuming a simple plane wave $\mathbf{E} = \mathbf{E}_0(\omega)\exp(-i\omega t)$, with amplitude $\mathbf{E}_0(\omega)$ and the frequency of the light ω, we can solve the following classical equation of motion,

$$m_e\frac{\partial^2\mathbf{r}}{\partial t^2} + m_e\Gamma\frac{\partial\mathbf{r}}{\partial t} = e\mathbf{E_0}(\omega)\exp(-i\omega t), \tag{2.16}$$

where m_e is the effective mass. The damping factor Γ depends on the Fermi velocity and the electron mean free path between scattering events with the ions. Assuming a periodic dependence of the motion of electrons, $\mathbf{r}(t) = \mathbf{r_0}\exp(-i\omega t)$ and substituting it in Eq. (2.16) we get

$$-m_e\omega^2\mathbf{r}(t) - i\omega m_e\Gamma\mathbf{r}(\mathbf{t}) = e\mathbf{E_0}(\omega)\exp(-i\omega t), \tag{2.17}$$

which gives us

$$\mathbf{r}(t) = -\frac{e\mathbf{E}_0(\omega)\exp(i\omega t)}{m_e\omega^2 + im_e\omega\Gamma}. \tag{2.18}$$

Note that only the particular solution is included, as the homogeneous solution decays to zero very rapidly (for gold, Γ is $\sim 1 \times 10^{14}$ s^{-1} [41]). On the other hand, the macroscopic polarization is

$$\mathbf{P} = \epsilon_0\chi_e(\omega)\mathbf{E}, \tag{2.19}$$

where ϵ_0 is the vacuum permittivity and χ_e is the electric susceptibility. Substituting $\mathbf{P}$ that we find from combining Eqs. 2.15 and 2.18 in Eq. (2.19)

$$\chi_e(\omega) = -\frac{ne^2/(m_e\epsilon_0)}{\omega^2 + i\omega\Gamma}. \tag{2.20}$$

Also, we know $\mathbf{D} = \epsilon_0\epsilon(\omega)\mathbf{E} = \epsilon_0\mathbf{E} + \mathbf{P}$, where $\mathbf{D}$ is the displacement field. So, we can write

$$\epsilon(\omega) = 1 - \frac{\omega_p^2}{\omega^2 + i\Gamma\omega}, \tag{2.21}$$

where $\omega_p = \sqrt{ne^2/m_e\epsilon_0}$ is the plasma frequency. It is straightforward to write this equation in real and imaginary parts

$$\epsilon(\omega) = 1 - \frac{\omega_p^2}{\omega^2 + \Gamma^2} + i\frac{\Gamma\omega_p^2}{\omega(\omega^2 + \Gamma^2)}, \tag{2.22}$$

Figure 2.8 shows the real and imaginary parts of $\epsilon(\omega)$ as a function of wavelength. As can be seen, the real part of the dielectric function is negative. This means that light cannot go through much thickness of metal. Skin depth is defined as the thickness in which the electric field of the penetrating light drops by a factor of 1/e. So, in essence our ultimate goal is to explore an ultrafast method for manipulating the skin depth.

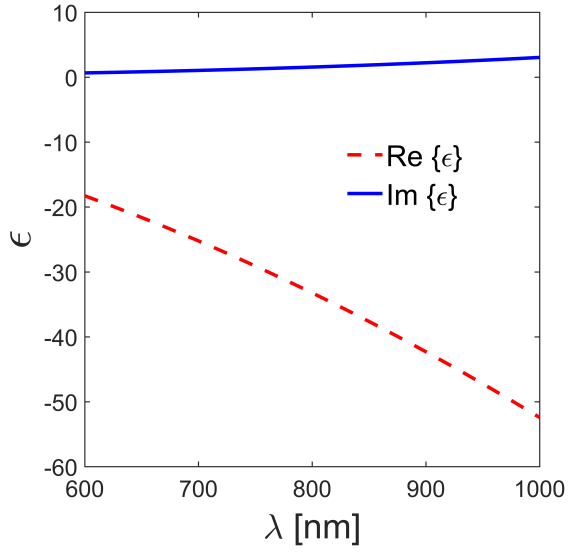

Figure 2.8: Real and imaginary components of ϵ for gold derived based on the classical Drude free electron model. We use $\omega_p = 13.8 \times 10^{15} s^{-1}$ and $\Gamma = 1.075 \times 10^{14} s^{-1}$ [43] for this plot. The negative value of the real part indicates that light cannot penetrate metal films [41, 42].

2.2.2 The role of bound electrons

One important question that we should answer about EIM is the role of bound electrons in the observed effect that will be discussed later. So, we need to understand how we can include the absorption of light by the bound electrons. For gold at wavelengths shorter than 550 nm, the imaginary part of ϵ does not follow Fig. 2.8. This is because high energy photons can be absorbed by the bound electrons, which take them to the conduction band. In other words, the Drude model provides us with accurate optical properties of metals as long as no interband transitions occur. We can include such transitions in the classical picture used here by adding a term that represents a simple harmonic oscillator (SHO). To do so, we can write the equation of motion for these bound electrons absorbing photons as

$$m_{bound}\frac{\partial^2 \mathbf{r}}{\partial t^2} + m_{bound}\gamma\frac{\partial \mathbf{r}}{\partial t} + \alpha \mathbf{r} = e\mathbf{E_0}\exp(-i\omega t), \tag{2.23}$$

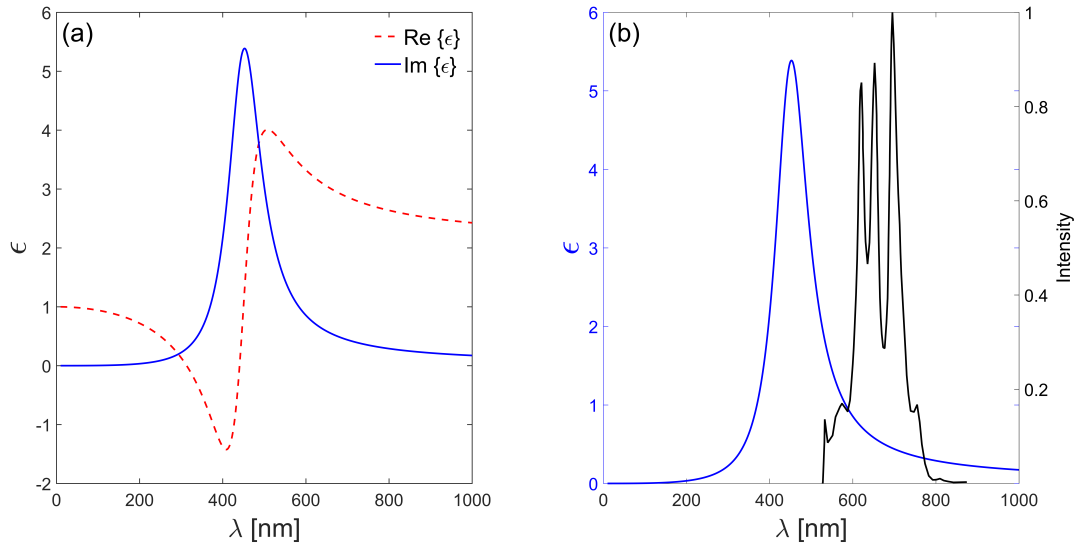

Figure 2.9: (a) Real, red curve, and imaginary, blue curve, components of ϵ for the contribution of the bound electrons. There is a resonant behavior in the imaginary part, which indicates gold has a strong absorption around ~ 450 nm. (b) imaginary components of ϵ as a function of wavelength compared with the spectral components of the laser used in the experimental efforts discussed later. It is shown in the black curve, and the peak normalized to unity in intensity. Note that the spectrum of the laser does not overlap significantly with the wavelengths in which gold has strong absorption, blue curve.

where m_{bound} is the effective mass of the bound electrons, γ is the damping constant for the bound electrons, and α is the spring constant of the SHO. Solving this differential equation, and following the same steps as we used to find Eq. (2.22) results in

$$\epsilon_{bound}(\omega) = 1 + \frac{\tilde{\omega}_p^2}{(\omega_0^2 - \omega^2) + i\gamma\omega}, \tag{2.24}$$

which can be simplified to

$$\epsilon_{bound}(\omega) = 1 + \frac{\tilde{\omega}_p^2(\omega_0^2 - \omega^2)}{(\omega_0^2 - \omega^2)^2 + \gamma^2\omega^2} + i\frac{\gamma\omega\tilde{\omega}_p^2}{(\omega_0^2 - \omega^2)^2 + \gamma^2\omega^2}, \tag{2.25}$$

where $\tilde{\omega}_p = \sqrt{\tilde{n}e^2/\epsilon_0 m_{bound}}$ ($\tilde{n}$ is the density of bound electrons) and $\omega_0 = \sqrt{\alpha/m_{bound}}$.

Figure 2.9 (a) shows the part of the dielectric function that is from the bound electrons

in gold. The imaginary part, which describes absorption has a resonant behavior, with a peak at $\lambda \sim$450 nm [41, 44, 45]. As can be seen in Fig. 2.9 (b) and will be discussed later, no single-photon interband absorption is expected [41] to play a major role in EIM. Note that we only included the lowest required photon energy for the interband transition to occur. So, while Fig. 2.9 does not show the whole picture, it supports our assumption of including only the free electrons in order to develop the model describing EIM in the next chapter.

2.3 Surface plasmons

The field of research of plasmonic effects is very interesting and much work has been done in this field. See [41, 42] and references within for more information. Here, only a few key points about it are discussed so that we can explore whether the observed phenomenon here is simply due to plasmonic effects.

For this work, surface plasmon polaritons (SPPs) are significant to consider, as the metal films used are fused silica coated with thin metal films. SPPs are electromagnetic excitations that propagate at the interface of a conductor, gold for example, and a dielectric [42], glass for example. This is due to the interaction between the light and the free conduction electrons in the metal. Let's assume the SPPs propagate in the x direction shown in Fig. 2.10. We can describe this wave using the Helmholtz equation

$$\nabla^2 \mathbf{E} + k_0^2 \epsilon \mathbf{E} = 0, \tag{2.26}$$

where k_0 is the wave vector in vacuum. Assuming that the wave propagates in the x direction, and it has no spatial variation y direction, which means that the metal-glass interface is in the xy plane, the electric field can be written as $\mathbf{E}(\mathbf{r}) = \mathbf{E}(z)\exp(ik_x x)$. Using this solution in Eq. (2.26), we get

$$\frac{\partial^2 \mathbf{E}(z)}{\partial z^2} + (k_0^2 \epsilon - k_x^2)\mathbf{E}(z) = 0. \tag{2.27}$$

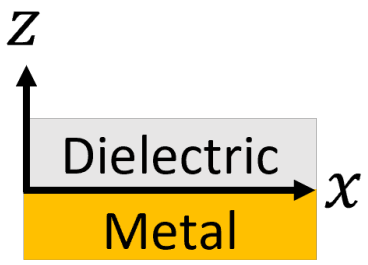

Figure 2.10: The metal-dielectric interface that the SPPs propagate on. We are assuming the SPPs are propagated in the x direction only.

With $\nabla \times \mathbf{E} = -\frac{\partial \mathbf{B}}{\partial t}$, and $\nabla \times \mathbf{H} = \frac{\partial \mathbf{D}}{\partial t}$, where $\mathbf{H}$ is the magnetic field inside a medium, one can find the differential equations that couple the electric and magnetic fields, assuming that propagation is in the x direction [42]

$$\begin{cases} \frac{\partial E_y}{\partial z} = -i\omega\mu_0 H_x \\ \frac{\partial E_x}{\partial z} - ik_x E_z = i\omega\mu_0 H_y \\ ik_x E_y = i\omega\mu_0 H_z \\ \frac{\partial H_y}{\partial z} = i\omega\epsilon\epsilon_0 E_x \\ \frac{\partial H_x}{\partial z} - ik_x H_z = -i\omega\epsilon_0\epsilon E_y \\ ik_x H_y = -i\omega\epsilon_0\epsilon E_z \end{cases}, \tag{2.28}$$

where μ_0 is the vacuum permeability. This system of coupled differential equations results in two sets of solutions [42]. One set with the magnetic field in the y direction and one set with the electric field in the y direction.

Using Eq. (2.27) and 2.28, the electric and magnetic components for the case in which

the magnetic field is in the y-direction can be found to be [42]

$$\begin{cases} H_y(z) = A_2 \exp(ik_x x) \exp(-k_{2,z} z) \\ E_x(z) = iA_2 \frac{1}{\omega \epsilon_0 \epsilon_2} k_2 \exp(ik_x x) \exp(-k_{2,z} z) \quad z > 0. \\ E_z(z) = -A_1 \frac{k_x}{\omega \epsilon_0 \epsilon_2} \exp(ik_x x) \exp(-k_{2,z} z) \end{cases} \tag{2.29}$$

and

$$\begin{cases} H_y(z) = A_1 \exp(ik_x x) \exp(k_{1,z} z) \\ E_x(z) = -iA_1 \frac{1}{\omega \epsilon_0 \epsilon_1} k_1 \exp(ik_x x) \exp(k_{1,z} z) \quad z < 0, \\ E_z(z) = A_1 \frac{k_x}{\omega \epsilon_0 \epsilon_2} \exp(ik_x x) \exp(k_{1,z} z) \end{cases} \tag{2.30}$$

where A_1 and A_2 are constants. Using the continuity condition at $z = 0$, we find that $A_1 = A_2$. Also, we find [42]

$$\frac{k_{2,z}}{k_{1,z}} = -\frac{\epsilon_2}{\epsilon_1}, \tag{2.31}$$

and, the condition on H_y results in [42]

$$k_{i,z}^2 = k_x^2 - k_0^2 \epsilon_i, \tag{2.32}$$

where $i = 1, 2$ denotes the two regions of of $z < 0$ and $z > 0$, respectively. Combining Eqs. 2.31 and 2.32, we find

$$k_x^2 = \frac{\epsilon_1 \epsilon_2}{\epsilon_1 + \epsilon_2} \frac{\omega}{c}. \tag{2.33}$$

This equation represents the energy conservation condition for SPPs [41]. Also, momentum conservation should be satisfied [41, 42]. So, the only way to excite SPPs is if both conditions are fulfilled [41, 42]. This puts limitations on how this excitation can be done. In other words, careful arrangement of the experimental conditions is required in order to excite SPPs.

One important fact about SPPs that we will use in understanding the experimental results is that if the electric field does not have any component perpendicular to the interface, which is in the z-direction, SPPs cannot be excited. To show that, let's look at the electric and magnetic components of this case on the interface. It can be shown, see [42] for details and derivation of these equations, that they are

$$\begin{cases} E_y(z) = A_2 \exp(ik_x x) \exp(-k_2 z) \\ H_x(z) = -iA_2 \frac{1}{\omega\mu_0} k_2 \exp(ik_x x) \exp(-k_2 z) \quad z > 0. \\ H_z(z) = A_2 \frac{k_x}{\omega\mu_0} \exp(ik_x x) \exp(-k_2 z) \end{cases} \tag{2.34}$$

and

$$\begin{cases} E_y(z) = A_1 \exp(ik_x x) \exp(k_1 z) \\ H_x(z) = iA_1 \frac{1}{\omega\mu_0} k_1 \exp(ik_x x) \exp(k_1 z) \quad z < 0. \\ H_z(z) = A_2 \frac{k_x}{\omega\mu_0} \exp(ik_x x) \exp(k_1 z) \end{cases} \tag{2.35}$$

Using the continuity condition at the interface, we find

$$A_1(k_1 + k_2) = 0. \tag{2.36}$$

We also know that the real part of k_1 and k_2 should be positive [42], which leads to the conclusion that $A_1 = A_2 = 0$. This means that no surface modes exist on this interface. So, no SPPs exist if there is no electric field component in the z-direction in Fig. 2.10. As will be discussed later, performing the experiment with two polarizations can give us a clue whether SPPs are responsible for a possible observed phenomenon, or not, as one of the polarizations does not excite them.

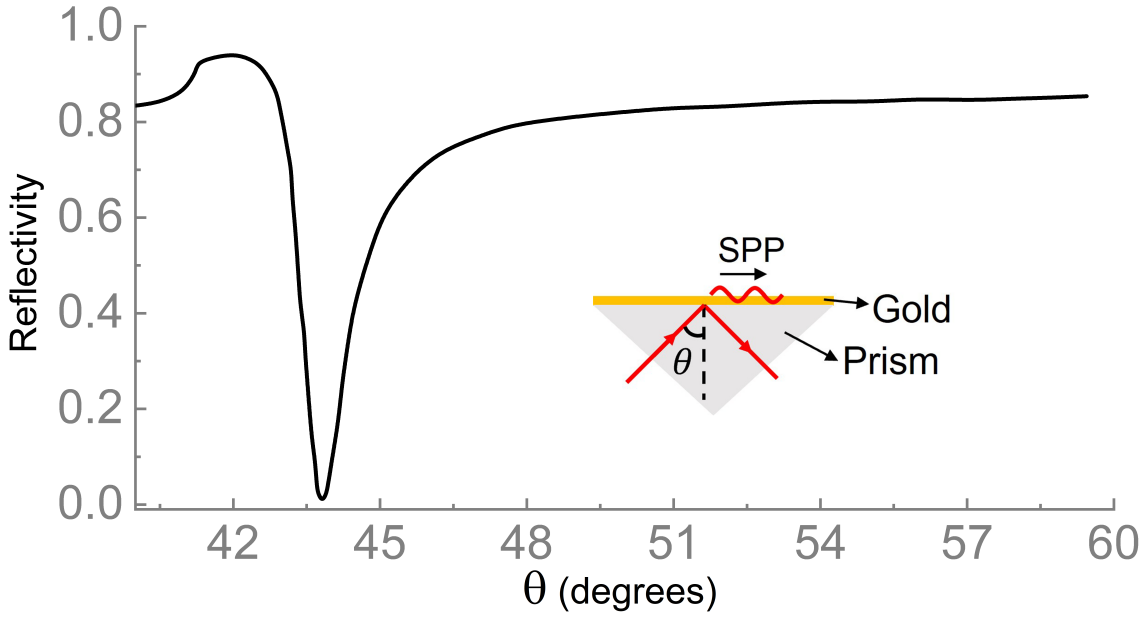

Figure 2.11: Reflectivity of 500 Å gold deposited on top of a prism as a function of the incident angle θ that is shown schematically in the inset. Adapted from [41]. The light reflection drops to zero at an incident angle of 43.5 degrees [41]

2.3.1 Excitation of SPPs

As discussed before, energy and momentum conservation should be satisfied so that SPPs are excited. Also, light should interact with the metal surface from the dielectric side of Fig. 2.10, and the dielectric should have a refractive index that is larger than one [41]. From another aspect, the excitation of SPPs is sensitive to the metal thickness. If the metals are too thick, the absorption in the metal suppresses the excitation of SPPs. If the metal is too thin, radiation damping into the glass damps it [41]. For gold, the optimum thickness is $\sim$ 500 Å. Figure 2.11 shows the reflectivity as a function of angle of incidence θ for a 500 Å gold metal film deposited on top of a prism [41]. Note that the excitation of SPPs results in a sharp decrease and minimum in the reflectivity of light.

This discussion brings us to the conclusion that the presence of surface plasmonic effects in what we call EIM is highly unlikely. First, the thickness of the metal films used here is much less than 500 Å. Second, in our experiments the light interacts with the metal thin

film in the air-metal interface as long as there is no oxidation of metal happening. We use gold and platinum, which do not oxidize. This further excludes the possibility of plasmonic effects. Also, for momentum and energy conservation requirements to be satisfied, the experimental conditions need to be carefully chosen. We do not optimize the experimental setup for observing plasmonic effects. One last possibility is the presence of physical holes in the metal film smaller than the light wavelength, which can excite plasmonic effects [41, 46–49]. There is a detailed discussion of why this cannot be the reason for the observed phenomenon in the coming sections.

Chapter 3

A model describing EIM

In this chapter, a model is developed in order to describe how one can alter the optical properties of metals. EIM is described using the Drude free electron model, which is the most simple description of conduction in metals [7–9]. The model developed is time averaged, and does not discuss time dependence of the process. Although this model explains EIM qualitatively, it captures the quantitative behavior of the transmission of light, and there is good agreement with the experimental results seen in Chapter 5.

A few things should to be mentioned to understand how the model is developed to describe EIM. These points are explained in more detail in Chapter 4. An unltrafast laser is used in our experiment. The temporal full width half maximum (FWHM) of the laser pulses is about 10 fs. This means that the laser used is a broadband laser with a FWHM spectral wavelength of more than 100 nm. The metal films used in the experiment are thin metal films of gold and platinum on fused silica substrates. The thickness range of the metal films is 20-400 Å.

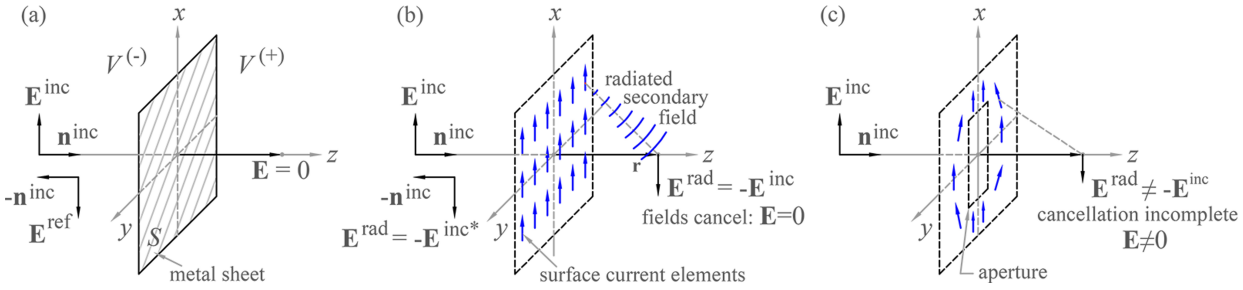

Figure 3.1: (a) A perfect conductor (S) is irradiated by a monochromatic light source. Boundary conditions dictate that no light is transmitted to the right, i.e. $V^{(+)}$ region. Assuming no absorption, all of the incident light is reflected back to the $V^{(-)}$ region . (b) Same problem considering the radiation from the surface current on the conductor. The radiated secondary field has the same magnitude and a opposite phase in comparison with the incident beam in the $V^{(-)}$. In the $V^{(+)}$, the radiated secondary field results in no transmission of light. (c) If we cut an aperture in the conductor, the secondary radiation is altered. As a result, there is a transmission from the sample, and the reflection is different in this case.

3.1 Basic concept

Reflection and transmission of light from metals, among the most basic yet most important phenomena in optics, are usually described in terms of boundary conditions [50, 51]. An alternative method for describing such phenomenon is by considering secondary radiation of the free electrons on the surface of metal [39, 52, 53]. Consider a perfect conductor sheet S, as seen in Fig. 3.1, that is illuminated by light along the z direction. Since no wave can exist inside a perfect conductor, the Maxwell boundary conditions (BC's) on S dictate that a reflected wave exists on the illuminated side of S and no light is transmitted. The BC's also result in a surface current $\mathbf{K}$. The lack of transmission can be explained in the following way as well [53]. At first, the incident wave is present on both sides of the sheet. Then, over a transient period, the sheet responds to the wave, and the surface current forms. In the steady state, radiation from this current generates the reflected wave observed on the sheets illuminated side, whereas on the dark side, the radiated wave exactly cancels the incident wave, as seen in Fig. 3.1. Thus, reflection from and the absence of transmission through the conductor can be understood as wave interference.

We can approximate a well collimated incident laser beam as

$$\mathbf{E}^{inc} = E_0^{inc} e^{i(kr\hat{\mathbf{z}}\cdot\hat{\mathbf{r}}-\omega t)}\hat{\mathbf{x}}, \tag{3.1}$$

where E_0^{inc} is the magnitude of the incident electric field, k is the wave vector, and r represents the position. Using the electric field in Eq. 3.1 and the BC's, it is straightforward to find surface current on the conductor:

$$\mathbf{K}(\mathbf{r}) = \frac{2k}{\mu_0\omega} E_0^{inc}\hat{\mathbf{x}}. \tag{3.2}$$

The field radiated by this current is [53]

$$\mathbf{E}^{rad} = i\omega\mu_0 \int_S \overleftrightarrow{\mathbf{G}}(\mathbf{r},\mathbf{r}')\cdot\mathbf{K}(\mathbf{r}')d^2x', \tag{3.3}$$

where $\overleftrightarrow{\mathbf{G}}(\mathbf{r},\mathbf{r}')$ is the dyadic Green's function.

$$\overleftrightarrow{\mathbf{G}}(\mathbf{r},\mathbf{r}') = \frac{e^{ikR}}{4\pi R}(\overleftrightarrow{I} - \hat{\mathbf{R}}\otimes\hat{\mathbf{R}}), \tag{3.4}$$

where $\mathbf{R} = \mathbf{r} - \mathbf{r}'$. Note that $\mathbf{r}$ represents the position, and $\mathbf{r}'$ represents the position on the sheet. Substituting Eq. 3.4 into Eq. 3.3, one gets

$$\mathbf{E}^{rad} = i\omega\mu_0 \int_S \frac{e^{ikR}}{4\pi R}(\overleftrightarrow{I} - \hat{\mathbf{R}}\otimes\hat{\mathbf{R}})\cdot\mathbf{K}(\mathbf{r}')d^2x', \tag{3.5}$$

which can be simplified by substituting Eq. 3.2 and using $(\hat{\mathbf{R}}\otimes\hat{\mathbf{R}})_{ij} = \hat{\mathbf{R}}_i\hat{\mathbf{R}}_j$ and $(\hat{\mathbf{R}}\otimes\hat{\mathbf{R}})\cdot\hat{\mathbf{x}} = \cos(\alpha)\hat{\mathbf{R}}$ (α is the angle between $\hat{\mathbf{x}}$ and $\hat{\mathbf{R}}$) to

$$\mathbf{E}^{rad} = \frac{ik}{2\pi} E_0 \iint_{-\infty}^{+\infty} \frac{e^{ikR}}{R}(\hat{\mathbf{x}} - \cos(\alpha)\hat{\mathbf{R}})dx'dy'. \tag{3.6}$$

Note that $R^2 = (x - x')^2 + (y - y')^2 + (z - z')^2$. The integral can be solved for $x = y = 0$ without loss of generality. Also, using the assumption that $z >> z'$, we can analytically solve this integral. Using polar coordinates in the $x'y'$ plane and defining $\xi^2 = x'^2 + y'^2$

$$\mathbf{E}^{rad} = ikE_0 \int_{-z}^{\infty} e^{ik\xi} \hat{\mathbf{x}} d\xi, \tag{3.7}$$

for $z < 0$, and

$$\mathbf{E}^{rad} = ikE_0 \int_{z}^{\infty} e^{ik\xi} \hat{\mathbf{x}} d\xi, \tag{3.8}$$

for $z > 0$. Note that it can easily be shown that the integral, including the $\cos(\alpha)$ term, vanishes. So, the radiated electric field is found to be [53]

$$\mathbf{E}^{rad}(\mathbf{r}) = \begin{cases} -(\mathbf{E}^{inc}(\mathbf{r}))^*, & z < 0 \\ -\mathbf{E}^{inc}(\mathbf{r}), & z > 0, \end{cases} \tag{3.9}$$

which results in the total electric field of

$$\mathbf{E}^{tot}(\mathbf{r}) = \begin{cases} \mathbf{E}^{inc}(\mathbf{r}) - (\mathbf{E}^{inc}(\mathbf{r}))^*, & z < 0 \\ \mathbf{E}^{inc}(\mathbf{r}) - \mathbf{E}^{inc}(\mathbf{r}) = 0, & z > 0 \end{cases}. \tag{3.10}$$

Eq. 3.10 shows that the induced surface current radiates a wave traveling away from S with exactly the same magnitude as the incident wave. In front of the sheet, the incident and radiated waves are counter-propagating to form a standing wave. Behind the sheet, the waves co-propagate, and the phase shift causes destructive interference.

Consider the case in which there is a distortion in the electron density of the conductor. Figure 3.1 (c) shows the simplest case. In this case, we cut an aperture in the conductor sheet. This results in a nonzero transmission and a different reflection compared to when there is no cut. If we can modify the electron density on the conductor, its optical properties

can be changed. This modification can be done by altering the spatial electron density, and hence the induced secondary radiation. As will be discussed in detail, we explore this possibility by creating standing waves on the surface of gold metal films. The fringe pattern temporarily alters the electron density of the sample. This modulation is due to the Coulomb force on electrons in the periodic structure of the electric field of a standing wave.

3.2 The basic approach of the theoretical model

In order to develop a theoretical model and design an experiment for EIM, we need to know the timescale on which EIM can be observed. We speculate that the redistribution of electrons depends on how fast the electron density relaxes to equilibrium after alteration. This relaxation time is ∼15 fs for gold [9, 54], which indicates that few-cycle laser pulses are required to observe such a phenomenon.

It is also important to know in what range of laser intensities we can work. While the higher the peak intensity the stronger the proposed phenomenon, the metal can be ionized, and the resulting Coulomb forces within the lattice cause ablation if the laser peak intensity for gold is $\geq 10^{13}$ W/cm^2 [55, 56]. This means that the peak intensity should be well below this limit yet high enough to observe the proposed phenomenon.

Moreover, the imaginary part of the dielectric constant of gold, which is responsible for absorption, has a peak at ∼450 nm [41, 44, 45], as seen in Fig. 2.9 (a). As was discussed before, few-cycle laser pulses are required to study EIM. The FWHM of the wavelength of the laser used in this study spans from ∼715 nm to 840 nm, so no single-photon interband absorption is expected to occur [20, 41], see Figs. 2.9 (a) and 3.2. In order to further rule out any effect of the interband transitions due to multi-photon absorption [57, 58], the estimated peak intensity [59] is kept $< 10^{11}$ W/cm^2. So, we estimate that the effect of two-photon absorption in our experiment is much smaller than the linear processes, and only free electrons in metal are included in our the qualitative model.

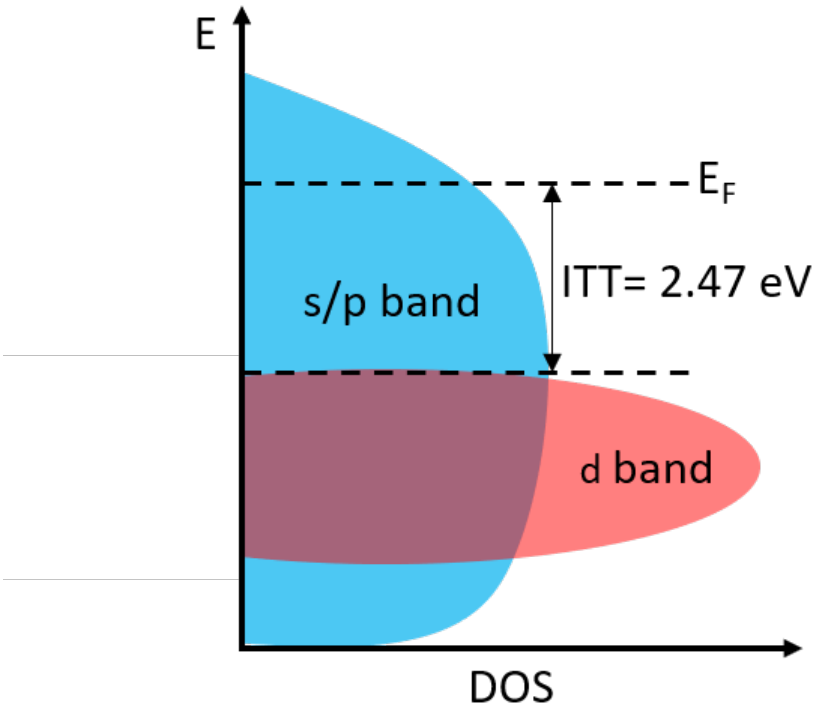

Figure 3.2: Energy as a function of density of states (DOS), adapted from Fig. 1 in Ref. [20]. The electrons that are in s/p band are considered free. Photons that have less energy than the interband transition threshold (ITT), which is 2.47 eV for gold only excite free electrons in the s/p band. This energy corresponds to a wavelength of 502 nm.

The Drude free electron model [7–9] is used to describe metals interacting with ultrafast lasers in EIM. In the framework of the Drude model, the noble metals are described as a gas of non-interacting electrons around positively-charged ions [9], as shown in Fig. 3.3. In the presence of an external electric field, these electrons are driven ballistically in the metal. Two beams form a standing wave on the surface of the metal, as seen in Fig. 3.4 (a) and (b). Consider the fringe pattern shown schematically in Fig. 3.4 (c). The beams creating the standing wave pattern are called "conditioning" beams. The electric field is negligible in the destructive interference regions, as shown in Fig. 3.4 (c). Figure 3.4 (d) shows the undisturbed electron distribution in the metal when no conditioning beams are present, and Fig. 3.4 (e) shows the disturbed and redistributed electron density due to the presence of the conditioning beams.

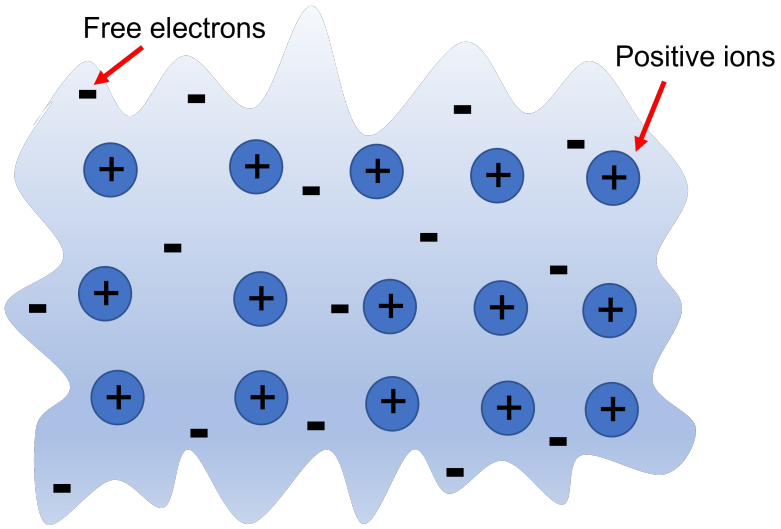

Figure 3.3: A depiction of the Drude model. It shows a metal as ions are surrounded by a gas of non-interacting electrons.

.

In order to estimate the change in electron distribution, consider half of each laser cycle when the electric field is positive in the constructive interference fringe regions. There is a net flow of electrons shown in the inset of Fig. 3.5 (a). This modification in electron density results in a modulation of skin depth. This means that the transmission of a third "signal" beam from the sample is different in regions with different skin depth.

Consider area $A_\perp$ in the yz plane in Fig. 3.5(a). The current density flowing through this area is $\mathbf{J} = -\sigma_0 Re(\mathbf{E}_c)$, where $\mathbf{J}$ is the current density, σ_0 is the DC conductivity of the metal, and $\mathbf{E}_c$ is the electric field of the conditioning beams. Using a plane wave approximation, the electric field can be written as $\mathbf{E}_c = E_{0,c}\mathbf{x}$. This results in $JA_\perp = \frac{dq}{dt}$ which gives us the following rate equation:

$$\frac{dq}{dt} = 2A_\perp \sigma_0 E_{0,c} \sin(\omega_c t). \tag{3.11}$$

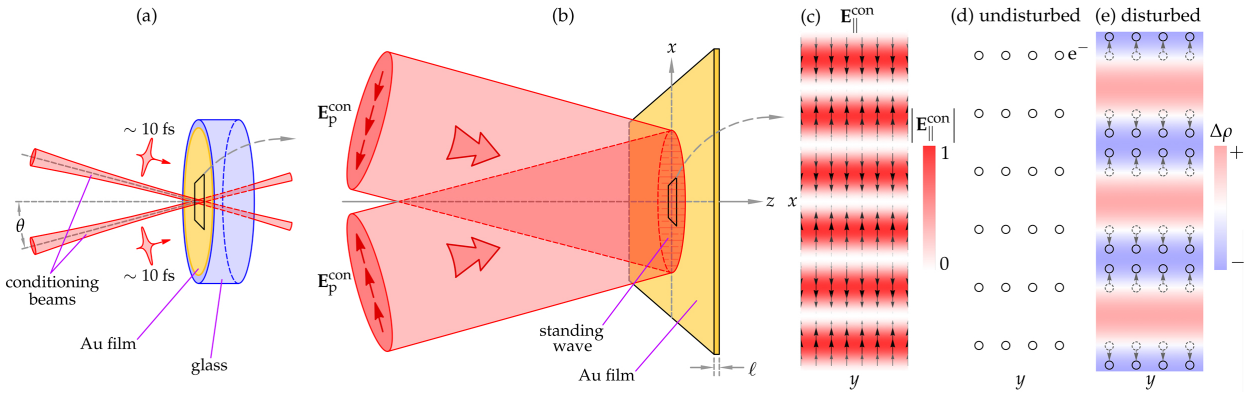

Figure 3.4: Schematic of (a) the two 10 fs conditioning beams focused on the metal film. (b) Formation of the standing wave on the thin film. (c) The fringe pattern and the direction of the electric field (d). Undisturbed electrons when the conditioning beams are blocked, i.e., no fringe pattern present. (e) The disturbed and redistributed electrons due to the presence of the conditioning beams.

Integrating over half the laser cycle we get

$$\Delta q(\lambda) = \frac{2A_{\perp}\sigma_0 E_{0,c}}{\omega_c}\int_0^{\pi} \sin(\omega_c t)\, d(\omega_c t), \tag{3.12}$$

which gives us the following for only half a cycle of the laser pulse:

$$\Delta q(\lambda) = \frac{2\lambda A_{\perp}\sigma_0 E_{0,c}}{\pi c}. \tag{3.13}$$

This equation describes the maximum amount of modulation in half a cycle. To be more exact, we need to consider the temporal behavior of the laser pulses in our estimation. We consider a Gaussian temporal profile

$$E_{0,c}(t) = E_{0,c} e^{(-2ln(2)(\frac{t}{\tau})^2)} \sin(\omega_c t). \tag{3.14}$$

The electric field is symmetric about time zero, as shown in Fig. 2.5. This means that the time integral will be zero. However, this integral represents the electron distribution after the pulse is gone which is expected to be zero. In order to find the effect of the electric

field on the electron distribution while the conditioning beams are present, we calculate the following integral using the magnitude of the electric field:

$$\Delta q_{all}(\lambda) = \frac{1}{2} \times \frac{2A_{\perp}\sigma_0 E_{0,c}}{\omega_c} \int_{-\infty}^{\infty} |e^{(-2Ln(2)(\frac{t}{\tau})^2)} \sin \omega_c t| \, dt. \tag{3.15}$$

The $\frac{1}{2}$ factor is present because the electron redistribution for when the electric field is positive (or negative) only is what is calculated here. Equation 3.15 results in $\Delta q_{all}(\lambda) \sim 10\Delta q(\lambda)$, where $\Delta q_{all}(\lambda)$ is the total electron redistribution.

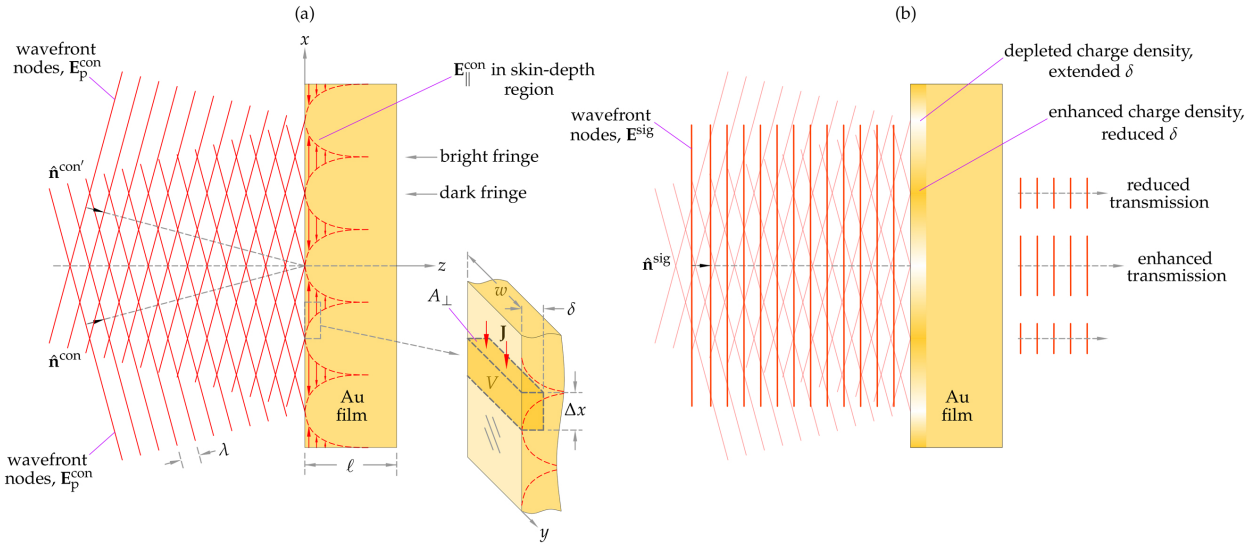

Figure 3.5: Electron redistribution and its effect on transmission. The sketch in (a) shows a cross section of the metal film exposed to the incident conditioning beams. Note that the internal field pattern is a stationary standing-wave pattern. The current flow through $A_{\perp}$ within the skin depth is shown in the zoomed part in the dashed box. (b) Exposure of the same metal film to the signal wave. The electrons are redistributed due to the presence of the conditioning beams. This results in reduced and enhanced transmission due to enhanced and depleted electron density, respectively.

We should compare the electron redistribution, $\Delta q_{all}(\lambda)$, that is calculated over the total number of half cycles in each laser pulse, with the total charge in the volume of one fringe in the absence of the conditioning beams. This value is $q_0 = neA_{\perp}\Delta X$, where n is the electron density, e is the charge of electron, and ΔX is the width of the fringes, which is ~ 3 μm in our experiment. We can now estimate $\Delta q/q_0$ for gold. Using the DC conductivity

$\sigma_0 = 4 \times 10^7 \Omega^{-1}\mathrm{m}^{-1}$, number density of conduction electrons $n = 5.9 \times 10^{28}\mathrm{m}^{-3}$, and a field magnitude of $4 \times 10^8 \mathrm{N/C}$, $\Delta q_{all}/q_0$ is estimated to be about $\sim$1% for a few-cycle laser pulse.

The change in electron density is equivalent to a change in conductivity. Skin depth in metals depends on conductivity as [51]

$$\delta(\lambda) = \sqrt{\frac{\lambda}{\mu\pi c\sigma_0}}, \tag{3.16}$$

where μ is permeability. So, the skin depth is smaller in the regions with higher electron density and larger in the regions with lower electron density.

In the absence of conditioning beams, the transmission of the "signal" beam after propagating through a metal film of thickness ℓ is [51]

$$I_0^{\mathrm{tra}}(\lambda) = 2I_0(\lambda)\exp\left[-\frac{2\ell}{\delta(\lambda)}\right], \tag{3.17}$$

where $I_0(\lambda)$ is the initial intensity of the signal beam. The transmission of light through one region with higher and one with lower electron density in the presence of the conditioning beams is

$$I_1^{\mathrm{tra}}(\lambda) = I_0(\lambda)\exp\left[-\frac{2\ell}{\delta(\lambda)-\Delta\delta(\lambda)}\right] + I_0\exp\left[-\frac{2\ell}{\delta(\lambda)+\Delta\delta(\lambda)}\right], \tag{3.18}$$

where

$$\Delta\delta = \frac{1}{2}\sqrt{\frac{\lambda}{\mu\pi c\sigma_0}}\frac{\Delta q}{q_0}. \tag{3.19}$$

Eq. 3.19 is the magnitude of the change in skin depth due to the conditioning beams. The sign of the change is accounted for in the denominator in Eq. 3.18. The first term in Eq. 3.18 is from a region with higher electron density and smaller skin depth, and the second term is from a region with lower electron density and larger skin depth.

As will be discussed in Chapter 4, the change in transmittance of the signal beam is calculated to investigate any change due to the presence of the conditioning beams. This change is defined as $\Delta T(\lambda) = T_1(\lambda) - T_0(\lambda)$, where $T_1(\lambda) = \frac{I_1^{\mathrm{tra}}(\lambda)}{I_0}$ and $T_0(\lambda) = \frac{I_0^{\mathrm{tra}}(\lambda)}{I_0}$ is the

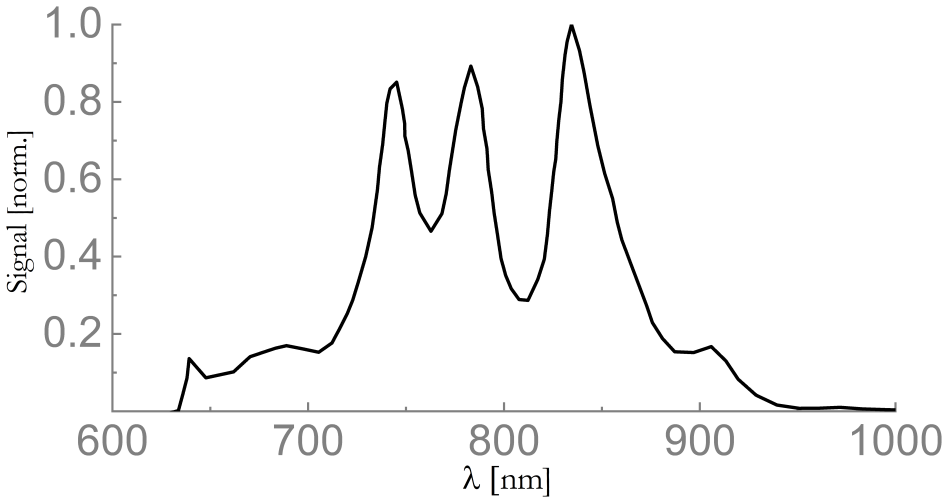

Figure 3.6: Spectrum of the broadband laser used in this experiment. The FWHM of the laser bandwidth is ∼124 nm.

transmittance of the "signal" beam in the presence of conditioning beams, and $T_0(\lambda)$ is its transmittance in the absence of the conditioning beams.

3.2.1 The effect of the laser bandwidth

What we discussed so far is the effect of monochromatic light with the central wavelength of the laser on the optical properties of gold. As mentioned, the ultrafast laser used in this experiment is broadband with a FWHM bandwidth of ∼124 nm. The laser spectrum is shown in Fig. 3.6 . We know from Eq. 3.16 that the skin depth depends on the laser wavelength as shown in Fig. 3.7 (a) . This indicates that the EIM effect is also wavelength dependent. Figure 3.7 (b) shows the EIM effect for three different wavelengths of the laser, 744, 785, and 850 nm, which have the highest spectral intensity. Note that the effect is scaled to one here so that it is easier to compare the position of the dips for the three wavelengths. It is clear that different spectral components of the laser result in a slightly different behavior of the EIM effect, so it is important to include the effect of the whole laser spectrum in the theoretical model.

In order to include the effect of the laser spectrum, we calculate $T_0 = \sum_\lambda T_0(\lambda)$ and

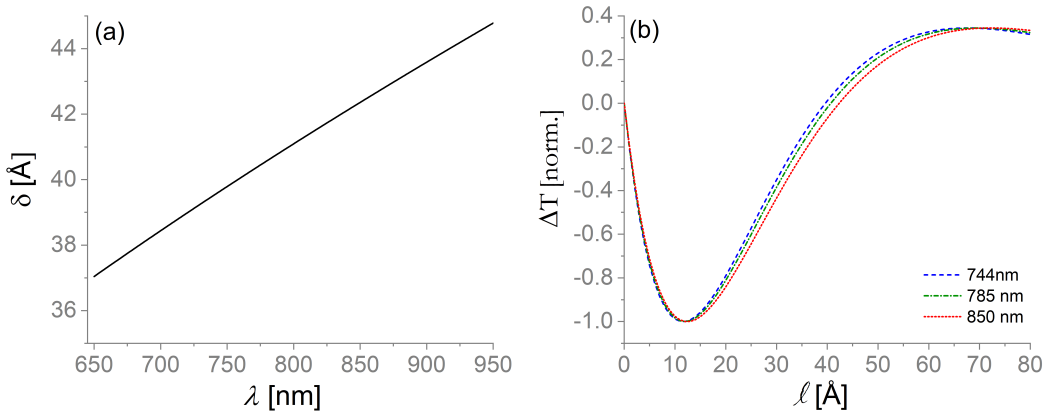

Figure 3.7: (a) The dependence of the skin depth on the wavelength of the light for the broadband laser used in this experiment. (b) EIM effect for three of the spectral components of the laser with the highest intensity, see Fig. 3.6. Note that they are normalized to unity.

$T_1 = \sum_\lambda T_1(\lambda)$, with a weighting factor for each wavelength to account for the wavelength dependent intensity of that spectral components of the laser shown in Fig. 3.6. The modification of the transmittance of the signal beam is then calculated to investigate any change due to the presence of the conditioning beams. The change of the transmittance as a function of gold thickness, considering the full laser spectrum, is plotted in Fig. 3.8.

3.2.2 The effect of the thickness dependant conductivity

The electrical properties of a bulk piece of metal are the intrinsic characteristics of the bulk material. However, melting point, optical characteristics, conductivity, etc., of a nanoscale metal film is different from the bulk, and depend on the size of the metal film [60]. This is due to the significant difference in the surface to volume ratio in a bulk and thin-film metal. Since we are studying thin films of gold, it is important to consider the thickness dependent characteristics, in this case the conductivity.

The thickness-dependent conductivity can be explained using a simple model [61]. In the

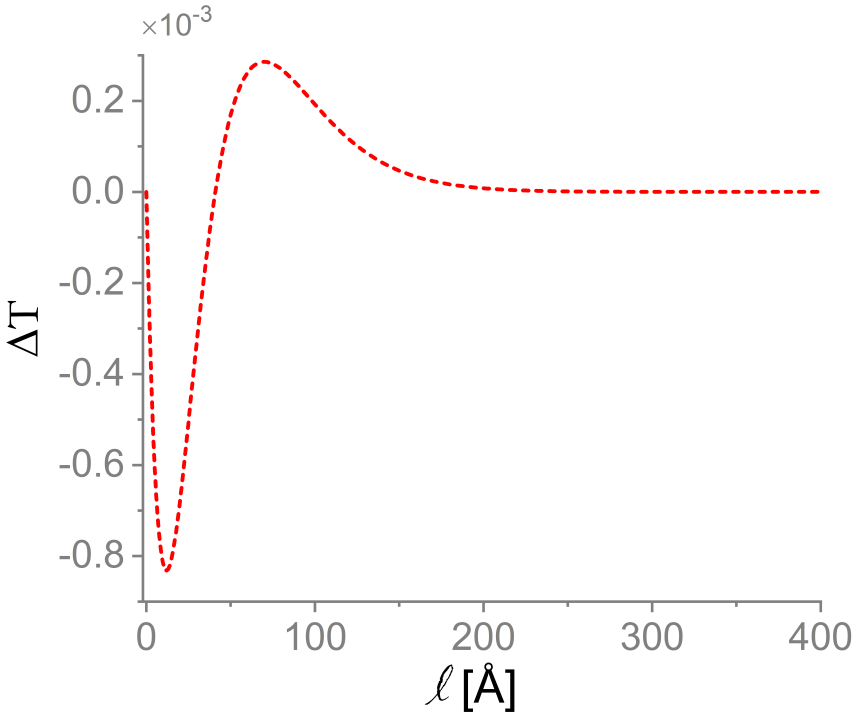

Figure 3.8: Prediction of the behavior of the change in transmittance as a function of the metal film thickness. The result is found by summing over the spectral components of the laser used in the experiment. The conductivity of the gold is considered to be constant in this case.

presence of an external electric field, electrons move in the opposite direction of the electric field. The mean free path, ℓ_{mfp}, is defined as the length of the electron path between two scattering events from the positive ions of the metal [8]. In a bulk metal, most electrons are scattered from positive ions before reaching the surface of the metal, as seen schematically in Fig. 3.9 (a). If the metal film thickness is comparable to this mean free path, ∼10 Å for gold [8], the situation is different. A greater number of electrons do not travel the whole mean free path before they reach the surface of the thin-film metal, as shown in Fig. 3.9 (b). In this case, these electrons are scattered off the surface [61]. This means there is more resistance for the motion of electrons in thin films compared to bulk metal, which results in a smaller conductivity, as shown in Fig. 3.10.

No data for the thickness dependent conductivity for the metal film thicknesses used

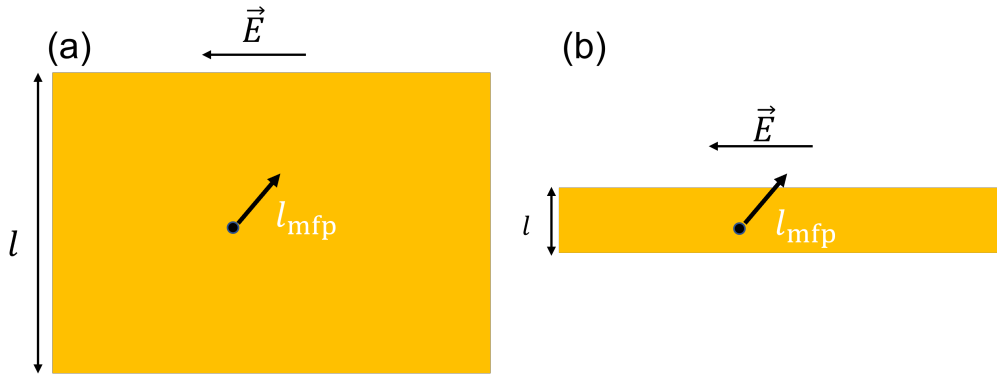

Figure 3.9: Adapted from [61] (a) Bulk gold. The mean free path (ℓ_{mfp}) is much bigger than the metal film thickness. Most electrons are scattered off positive ions, and they are never scattered off the surface. (b) A thin film with a thickness that is comparable to the mean free path of electrons. In this case, many electrons are scattered off the surface before they can travel the whole mean free path. Such metal films have a lower conductivity compared to a bulk sample. So, the conductivity depends on thickness of the sample for thin films with thicknesses comparable to the ℓ_{mfp}

in this experiment (20-400 Å) is available to the best of our knowledge. To resolve this issue, we use the data available, which goes to as thin as 200 Å, and estimate the thickness dependent conductivity of our metal films using extrapolation. Of course, this approach assumes a smooth dependence for metal films thinner than 200 Å. Figure 3.10 shows the thickness-dependent conductivity of gold. As can be seen, the conductivity of thin films is considerably smaller than the conductivity of bulk gold.

The dependence of the transmittance modification to the metal film thickness considering the effect of the whole laser bandwidth and the thickness dependent conductivity is shown in Fig. 3.11. The general behavior considering the thickness dependent conductivity is the same as before. However, the maximum of the absolute value of the predicted effect is bigger by almost an order of magnitude. Moreover, the dip value is shifted to thicker metal films by a factor of about 2 ($\sim$15 Å without the effect of the thickness dependent conductivity and $\sim$ 30 Å considering it).

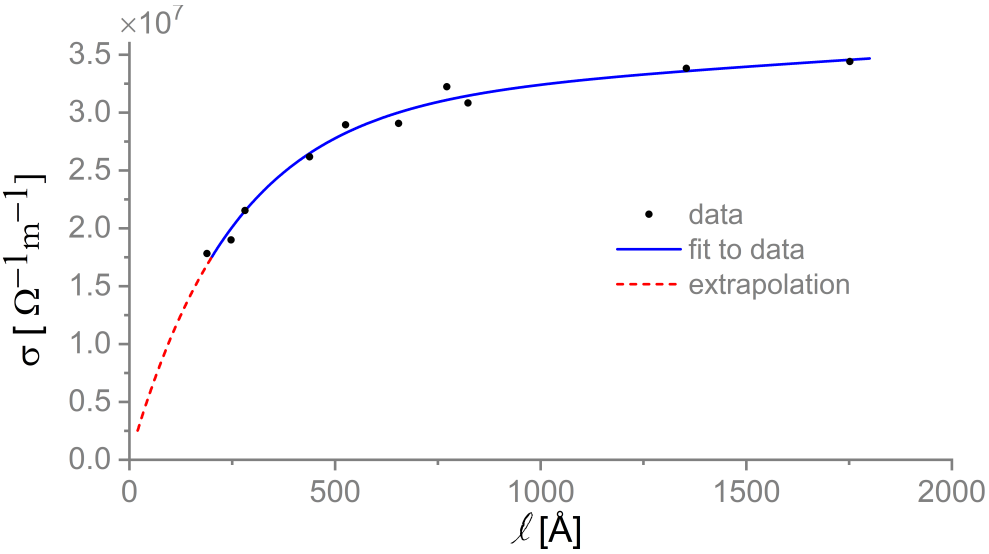

Figure 3.10: Thickness dependent conductivity of gold thin films. Black circles: experimental data from [60]. Blue line: fit to the experimental data. Red dashed line: extrapolation to find conductivity of thinner metal films. The experimental data is from [60]. Since no data for metal films as thin as the ones we use exist, to the best of our knowledge, we extrapolate the conductivity for our metal films from the experimental data. This assumes a smooth behavior of the conductivity, which has been shown to be the case for silver and platinum. [62–64].

3.2.3 A more complete treatment of the skin depth

In what was discussed so far, we simply considered the intensity of the laser light to decrease exponentially as it travels through metal. Here, the behavior of the light transmitting through metal is discussed in a more complete manner [51]. A schematic of the problem is shown in Fig. 3.12. The signal beam is traveling in the z direction. The normal vector of the surface of the metal film going outwards from the metal as shown in Fig. 3.12 is defined as $\hat{\mathbf{n}}$. The following Maxwell's equations can be used to find the electric and magnetic fields of the signal beam inside the metal:

$$\nabla \times \mathbf{E}(\mathbf{r}, t) = -\frac{\partial \mathbf{B}(\mathbf{r}, t)}{\partial t}, \tag{3.20}$$

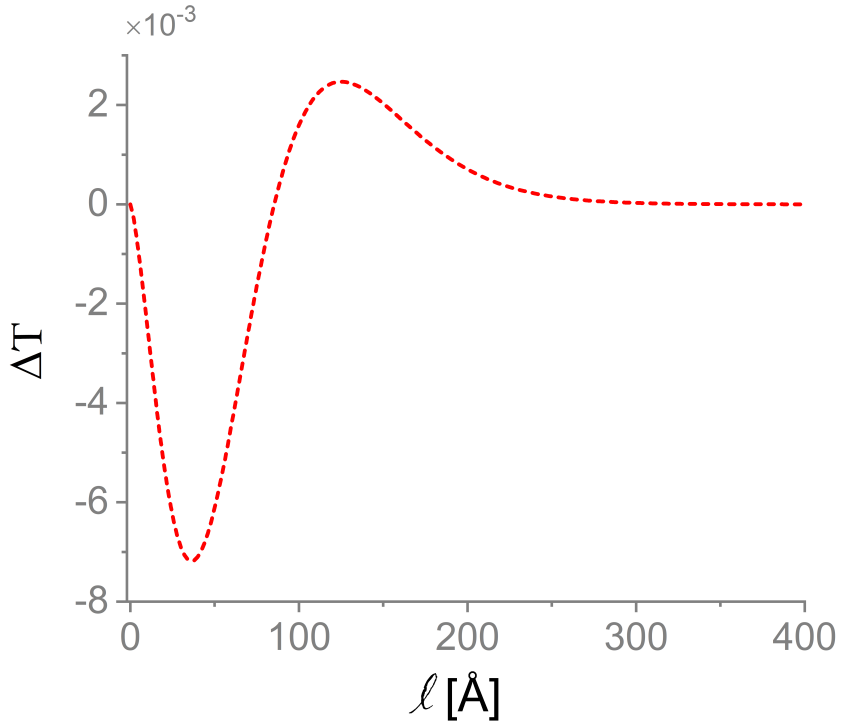

Figure 3.11: EIM in gold considering the effect of the laser bandwidth and the thickness dependent conductivity.

and

$$\nabla \times \mathbf{H}(\mathbf{r},t) = \mathbf{J}(\mathbf{r},t) + \frac{\partial \mathbf{D}(\mathbf{r},t)}{\partial t}. \tag{3.21}$$

Considering a plane wave ($\mathbf{E}(\mathbf{r},t) = \mathbf{E}(\mathbf{r})e^{i\omega t}$ and $\mathbf{B}(\mathbf{r},t) = \mathbf{B}(\mathbf{r})e^{i\omega t}$)

$$\nabla \times \mathbf{E}(\mathbf{r},t) = -i\omega \mathbf{B}(\mathbf{r},t), \tag{3.22}$$

and

$$\nabla \times \mathbf{H}(\mathbf{r},t) = \sigma \mathbf{E}(\mathbf{r},t) + i\epsilon_0 \omega \mathbf{E}(\mathbf{r},t). \tag{3.23}$$

For a good conductor, such as gold, irradiated by visible light, $\sigma \sim 10^7\ \Omega^{-1}m^{-1}$ [60] and $\epsilon_0\omega \sim 10^2 - 10^3$, so we can ignore the second term in Eq. 3.23, which is the displacement current term.

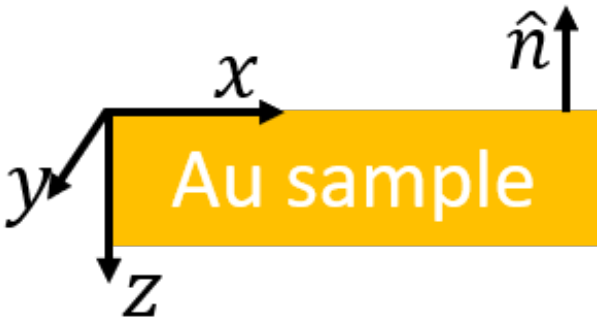

Figure 3.12: Coordinate system for a more complete treatment of the skin depth. Light is traveling in the $+z$ direction.

In the problem that is being solved, the spatial change in the propagation direction is much more significant than in the change in the xy plane. This leads to using the following approximation:

$$\nabla = -\hat{\mathbf{n}}\frac{\partial}{\partial z}. \tag{3.24}$$

So

$$\mathbf{E}_c = -\frac{1}{\sigma}\frac{\partial}{\partial z}(\hat{\mathbf{n}} \times \mathbf{H}_c), \tag{3.25}$$

and

$$\mathbf{H}_c = -\frac{i}{\mu_0\omega}\frac{\partial}{\partial z}(\hat{\mathbf{n}} \times \mathbf{E}_c), \tag{3.26}$$

where $\mathbf{E}_c$ and $\mathbf{H}_c$ are the electric and magnetic fields inside a good conductor, respectively. From Eqs. 3.25 and 3.26, it is clear that $\hat{\mathbf{n}}.\mathbf{H}_c = 0$ and $\hat{\mathbf{n}}.\mathbf{E}_c = 0$.

Taking a partial z derivative of both sides of Eq.3.25 :

$$\frac{\partial \mathbf{E}_c}{\partial z} = -\frac{1}{\sigma}\frac{\partial^2}{\partial z^2}(\hat{\mathbf{n}} \times \mathbf{H}_c). \tag{3.27}$$

Also, the cross product of Eq. 3.26 and $\hat{\mathbf{n}}$ results in:

$$\hat{\mathbf{n}} \times \mathbf{H}_c = -\frac{i}{\mu_0\omega}\frac{\partial}{\partial z}(\hat{\mathbf{n}} \times (\hat{\mathbf{n}} \times \mathbf{E}_c)) = \frac{i}{\mu_0\omega}\frac{\partial}{\partial z}(\hat{\mathbf{n}}(\hat{\mathbf{n}}.\mathbf{E}_c) - \mathbf{E}_c) = -\frac{i}{\mu_0\omega}\frac{\partial \mathbf{E}_c}{\partial z}. \tag{3.28}$$

Combining Eq. 3.27 and Eq. 3.28 and rearranging, we get

$$\frac{\partial^2}{\partial z^2}(\hat{\mathbf{n}} \times \mathbf{H}_c) + \frac{2i}{\delta^2}(\hat{\mathbf{n}} \times \mathbf{H}_c) = 0. \tag{3.29}$$

The solution to Eq. 3.29 can be found to be

$$\hat{\mathbf{n}} \times \mathbf{H}_c = \mathbf{A}e^{\frac{iz}{\delta}\sqrt{2i}} + \mathbf{B}e^{-\frac{iz}{\delta}\sqrt{2i}}. \tag{3.30}$$

We know that $\sqrt{i} = e^{\frac{i\pi}{4}}$. So

$$\hat{\mathbf{n}} \times \mathbf{H}_c = \mathbf{H}_{||}e^{-\frac{z}{\delta}}e^{\frac{iz}{\delta}}. \tag{3.31}$$

Note that $\mathbf{B} = 0$ due to the boundary condition requirement at infinity, and $\mathbf{A} = \mathbf{H}_{||}$. Also, $\hat{\mathbf{n}} \times \mathbf{H}_c$ is parallel to the surface of the metal. That is why the first term on the right hand side of Eq. 3.31 is labeled as $\mathbf{H}_{||}$.

From Eq. 3.25 and Eq. 3.31, we can find $\mathbf{E}_c$ to be

$$\mathbf{E}_c = \sqrt{\frac{\mu_0\omega}{2\sigma}}(1-i)\mathbf{H}_{||}e^{-\frac{z}{\delta}}e^{\frac{iz}{\delta}}. \tag{3.32}$$

Eq. 3.32 shows that the electric field decays exponentially as the thickness of the metal increases with respect to the skin depth. It also shows a phase shift for the light after propagating through metal. The magnitude of the phase shift depends on the skin depth and the thickness of the metal. Recall that the change in electron density results in modification of the skin depth. So, aside from the exponential decay that was considered in calculating ΔT, the phase shift should be considered as well. This is straightforward to do, we can

write:

$$I_1^{\text{tra}}(\lambda) = I_0(\lambda)\left\{\exp\left[-\frac{\ell}{\delta(\lambda)-\Delta\delta(\lambda)}\right]\exp\left[\frac{i\ell}{\delta(\lambda)-\Delta\delta(\lambda)}\right]+\exp\left[-\frac{\ell}{\delta(\lambda)+\Delta\delta(\lambda)}\right]\right.$$
$$\left.\times\exp\left[\frac{i\ell}{\delta(\lambda)+\Delta\delta(\lambda)}\right]\right\}\left\{\exp\left[-\frac{\ell}{\delta(\lambda)-\Delta\delta(\lambda)}\right]\exp\left[\frac{i\ell}{\delta(\lambda)-\Delta\delta(\lambda)}\right]\right.$$
$$\left.+\exp\left[-\frac{\ell}{\delta(\lambda)+\Delta\delta(\lambda)}\right]\exp\left[\frac{i\ell}{\delta(\lambda)+\Delta\delta(\lambda)}\right]\right\}^*, \tag{3.33}$$

and

$$I_0^{\text{tra}}(\lambda) = I_0(\lambda)\left\{2\exp\left[-\frac{\ell}{\delta(\lambda)}\right]\exp\left[\frac{i\ell}{\delta(\lambda)}\right]\right\}\left\{2\exp\left[-\frac{\ell}{\delta(\lambda)}\right]\exp\left[\frac{i\ell}{\delta(\lambda)}\right]\right\}^*. \tag{3.34}$$

Eq. 3.33 can be simplified and rewritten as

$$I_1^{\text{tra}}(\lambda) = I_0(\lambda)\left\{\exp\left[\frac{-2\ell}{\delta(\lambda)-\Delta\delta(\lambda)}\right]+\exp\left[\frac{-2\ell}{\delta(\lambda)+\Delta\delta(\lambda)}\right]\right.$$
$$\left.+2\exp\left[\frac{-2\ell\delta(\lambda)}{\delta(\lambda)^2-\Delta\delta(\lambda)^2}\right]\cos\left[\frac{2\ell\Delta\delta(\lambda)}{\delta(\lambda)^2-\Delta\delta(\lambda)^2}\right]\right\}. \tag{3.35}$$

Including the phase shift term, ΔT can be defined as before considering the laser bandwidth and the thickness-dependent conductivity:

$$\Delta T = T_1 - T_0. \tag{3.36}$$

Again, here $T_0 = \sum_\lambda T_0(\lambda)$ and $T_1 = \sum_\lambda T_1(\lambda)$. Figure 3.13 shows the EIM effect as a function of the thickness of the metal film considering all corrections. It shows a dip in the transmission of light as before. Note that the position of maximum change is shifted to larger thicknesses by considering different corrections in the model described here.

This general behavior of the change in transmission is the motivation to design an experiment to test and see if this phenomenon that is predicted by a simple classical model

can be observed or not.

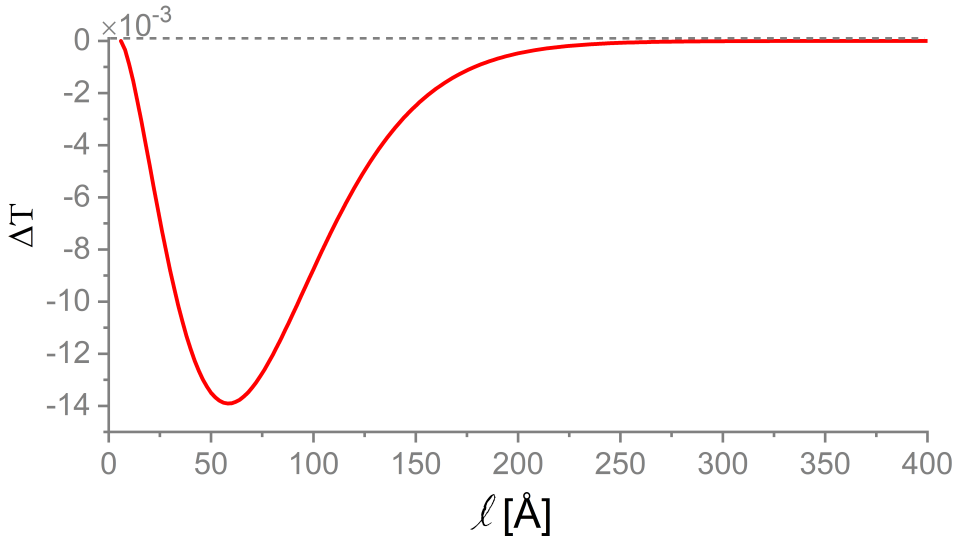

Figure 3.13: Prediction of the EIM as a function of the metal film thickness from Eq. 3.36 considering all the corrections discussed here.

The theoretical model predicts a decrease in transmission of light due to the presence of conditioning beams. One might find this surprising as when electrons go from one region to the other, the lack of electrons in one region is compensated by the extra electrons in the other region. However, note that there is an exponential dependence of the transmission of light through gold on the skin depth, see Eq. 3.17. So, the effect of an increased electron density in one region and a decrease in the other do not cancel each other.

3.2.4 Angle of incidence

The model for the EIM compares the electron redistribution due to the action of the conditioning beams with the total charge in a volume. The volume V is shown in Fig. 3.5(a) and corresponds to one fringe across the metal film and the skin depth into it. The electron redistribution in V depends on the conductivity, which depends on the electron density, as shown by Eq. 3.13. Yet, the total charge available to be redistributed depends on the geometry of V. Thus, by changing the fringe spacing, we can vary V and vary the amount

of charge redistributed. The result would be a variation of the transmittance change seen in Fig. 5.2(a). A straightforward way to achieve this is to change the angle of incidence α of the two conditioning beams on the metal film.

It is possible to use the model to estimate the effect that varying α would have. Consider Fig. 3.14, showing the two conditioning beams incident on the metal film. Summing the fields of the two beams gives

$$E(x) = E_1(x) + E_2(x) = E_\mathrm{o} \exp(ik_{1,x}x) + E_0 \exp(ik_{x,2}x), \tag{3.37}$$

where $k_{x,1} = -k \sin\alpha$ and $k_{x,1} = -k \sin\alpha$. Equation 3.37 simplifies to

$$E(x) = 2E_\mathrm{o} \cos\left[k \sin\left(\alpha\right)x\right],$$

from which it is seen that the fringe spacing Δx will be

$$\Delta x = \frac{2\pi}{k \sin\alpha}. \tag{3.38}$$

In the experiments that will be discussed later, $\alpha = 15°$, which corresponds to $\Delta x \approx 3\,\mu$m for a wavelength of $\lambda = 790\,$nm and produces the ΔT measurements in Fig. 5.2(a). Figure 3.14, however, shows how the model predicts ΔT to change with different α. Increasing α results in a smaller fringe separation Δx, and thus an increase in the magnitude of the dip in ΔT.

Observing the behavior in Fig. 3.14, even for a single α, would be important evidence for the EIM effect. It would show that one can change the optical properties of a metal film by simply changing the fringe spacing of the conditioning beams, at least in the context of an arrangement like Fig. 4.1 where the conditioning beam pulse duration must remain short, i.e., $\tau < \tau_\mathrm{e}$. One could then consider more complex fringe patterns and the consequence their structures could have on ΔT. In other words, it may be possible to demonstrate a "dynamic

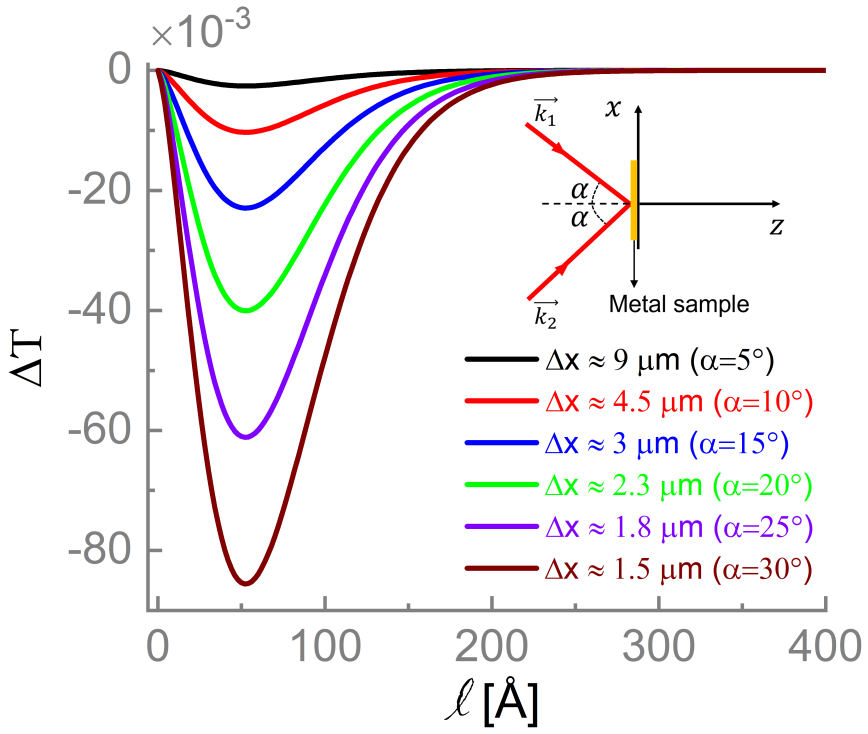

Figure 3.14: Model prediction for the variation of ΔT versus ℓ for different values of the fringe spacing Δx. The inset shows a schematic defining the angle of incidence α, which is used to calculate Δx in Eq. 3.38. The two conditioning beams with wave vectors $\mathbf{k}_1$ and $\mathbf{k}_2$ are overlapped at the surface of the metal.

metamaterial" where the optical properties of a metal film are adjustable externally.

3.3 EIM in platinum

What was discussed so far was about the possibility of observing EIM in gold. However, the concept of EIM implies that the effect should occur for any metal with high conductivity across the laser spectrum. Observation of EIM for metals other than gold would further support the validity of EIM and provide more clear evidence that plasmonic effects are not significant. That is, because plasmon resonances are exquisitely sensitive to the material supporting them [41], it is unlikely that they could be responsible for similar changes in transmittance or reflectance for different metals. While many metals exhibit the high con-

ductivity needed for EIM, not all will be practical for the experiment due to the potential for oxidation. An oxide layer forming on the metal film would mean that the metal is between two dielectrics: the oxide layer and the glass window substrate. It is known that for such a configuration the momentum conservation requirements that are needed for the excitation of surface plasmon resonances can be satisfied, as discussed in Chapter 2, in Platinum is therefore an excellent candidate to test, other than gold, as its oxidation propensity is very low. Other metals, which have greater tendency to oxidize, can also be investigated in the future by placing the metal film in a cell with inert gas such as N_2. The thickness-dependent conductivity of platinum reported in [65] is shown in Fig. 3.15. The theoretical treatment for platinum is the same as what was discussed in detail for gold. With the thickness dependent conductivity, we can estimate the magnitude of the EIM effect that should be observed, which is presented in Fig. 3.16. Note that the same measurement conditions are assumed for finding the EIM effect for gold and platinum.

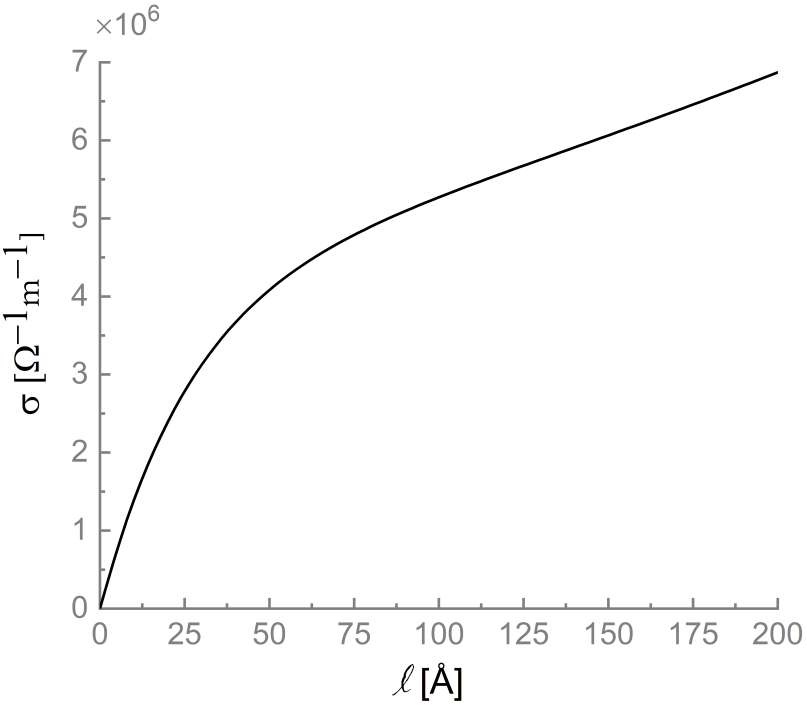

Figure 3.15: Theoretical thickness dependant conductivity of platinum from [65].

The similarity of the effect between gold and platinum here can be understood from the similarity of their conductivity values. Yet, there are differences between the metals. In particular, the model predicts that platinum would support EIM for greater film thicknesses as demonstrated by the broader dip in Fig. 3.16. There will be particular interest for metals with significantly different conductivity than gold and platinum. Studying such metals would allow us to test the role of conductivity in the EIM process.

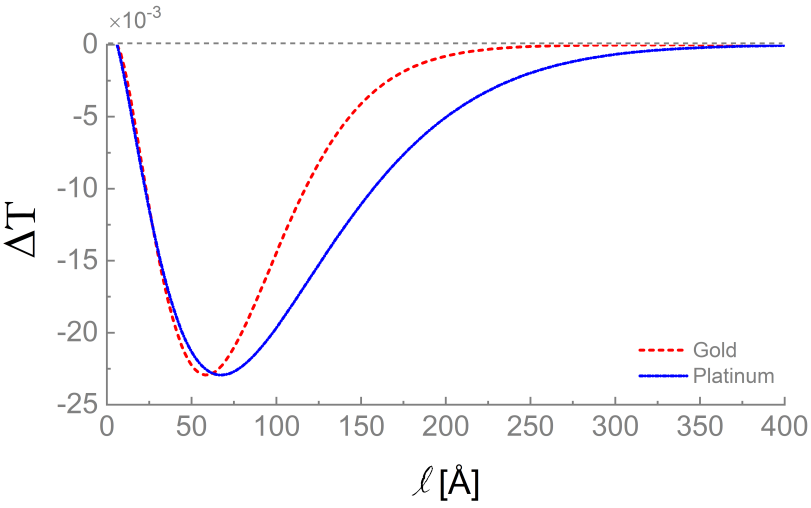

Figure 3.16: Theoretical prediction of the EIM effect for gold and platinum as a function of film thickness ℓ. The same measurement conditions and arrangement are assumed here. Note that the two metals exhibit similar-magnitude EIM effects but differ with regard to the ℓ dependence.

Chapter 4

Experiment

In this chapter, the experimental setup proposed in order to study EIM of reflection and transmission of light from metals is explained. A schematic of the setup is shown in Fig. 4.1. Note that due to the fact that we are working with ultrashort pulses, transmissive optics should be avoided as much as possible, unless they are necessary and optimized for ultrashort pulses, so that we do not end up with longer pulses than are needed in our experiment (laser pulse duration, τ should be shorter than 15 fs). This chapter starts with a general description of the experimental setup. Then all the important elements of the setup are briefly described.

4.1 Experimental setup

The experimental setup used to study EIM is shown in Fig. 4.1. An 80 MHz repetition rate Ti:Sapphire laser source that delivers ∼10 fs duration pulses (FWHM in intensity), right before the thin metal film, is used in this experiment. Multiple ultrafast optimized flat mirrors (FM) are used in the setup. To characterize the laser pulses, an interferometric autocorrelator [36, 37] that is pre-compensated is used.

The central wavelength of the linearly-polarized pulses is 790 nm. The FWHM of the

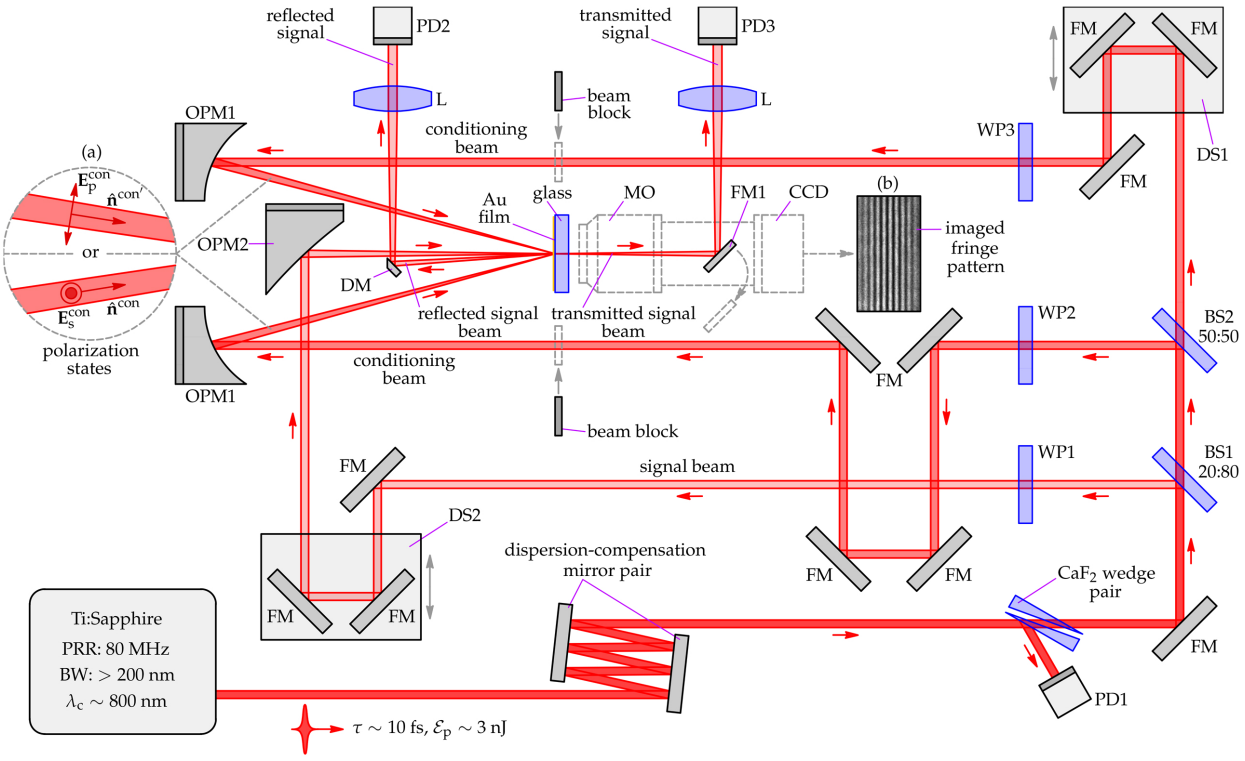

Figure 4.1: Optical layout used to test the EIM concept experimentally. As described in the text, a GDD pre-compensated beam of $\tau \sim 10$ fs pulses from a Ti:Sapphire laser is split into the signal beam and two conditioning beams. The beams are brought to a focus on the gold film, where photodiodes PD2 and PD3 measure the film's reflectance and transmittance, respectively. The inset (a) shows the two linear polarization states of the conditioning beams, where both beams are either s- or p-polarized. Inset (b) shows an example of an observed fringe pattern due to the conditioning-beams standing wave as image through the removable microscope objective (MO) by a CCD sensor.

wavelength of the laser used in this study spans from ∼715 nm to 840 nm. As discussed before, the greater the intensity of these pulses, the stronger the EIM effect should be. However, ablation occurs if the intensity is greater than $\sim 10^{13}$ W/cm^2 [55, 56, 66]. So, the peak pulse intensity [59] in the measurements is kept $\leq 10^{11}$ W/cm^2, and ablation is avoided.

A set of dispersion-compensation mirrors [38] are used for group delay dispersion (GDD) compensation, i.e. managing the chromatic dispersion of air and optical elements in the beam path [37], as shown in Fig. 4.1. Using chirped mirrors is critical because short pulses in the visible range become longer due to the GDD added by air or the optical elements [36, 37]. For example, for the central wavelength of the laser (∼790 nm), the GDD of air is ~ 65 fs^2. This means that a 10 fs laser pulse becomes ∼20 fs after traveling in three meters of air. Each optical element in the beampath also adds a small amount of GDD, so one might end up with a much longer pulse than the laser output if no GDD compensation is done. A CaF_2 compensation wedge pair is also used to fine tune the GDD and obtain the shortest pulses at the metal film.

A 20:80 Reflection:Transmission (R:T) low GDD beamsplitter (Thorlabs UFBS2080), BS1, reflects 20% of the beam that will be used as the signal. A 50:50 (R:T) beamsplitter (Thorlabs UFBS5050), BS2, splits the transmitted beam from BS1 into two conditioning beams. A delay stage is used in the beam path of one of the conditioning beams and another one in the signal beam path to find the temporal overlap of the three beams. These delay stages are labeled DS1 and DS2 in Fig. 4.1, respectively. The polarization of the three beams is controlled using three identical low GDD half waveplates (WP). To ensure that the conditioning and signal beams have the same pulse duration, identical optical elements are used in the three arms. Figure 4.2 shows the temporal characteristics of the two conditioning beams. All the measurements are done with cross-polarized conditioning and signal beams in order to eliminate any effect from interference between conditioning beams and the signal beam [67].

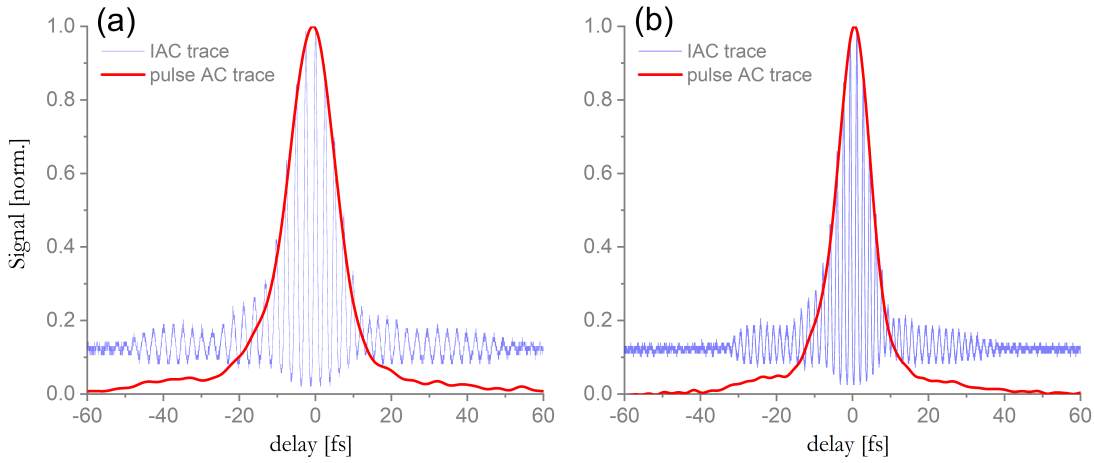

Figure 4.2: Pulse characterization of the two conditioning beams. (a) Pulse transmitted through BS2 with a FWHM pulse duration of 10.2 fs. (b) Pulse reflected from BS2 with a pulse duration of 9.7 fs. Note that the error bar of the interferometric autocorrelator reported by the company is ∼10%.

The conditioning beams are focused onto the metal film using two 15° off-axis parabolic mirrors (OPM1) with a focal length of 381 mm. The spatial separation between two consecutive bright fringes of the standing wave created on the metal film is ∼3 μm. A 90° off-axis parabolic mirror (OPM2) focuses the signal beam on the metal film.

The metal films used in this experiment, made by Ferrotec-Temescal, are different thicknesses of gold thin films deposited on fused silica. The metal film thickness has a typical error, reported by Ferrotec-Temescal, of $< \pm 10$ Å (for a 60 Å thick sample).

Three photodiodes with a rise time of about 1 ns are used for data collection. The first, PD1, shown in Fig. 4.1, is close to the laser source and monitors the pulse-to-pulse laser power fluctuations. Monitoring the laser output pulse-to-pulse allows us to correct the collected data properly if there is a significant change in the laser output. The second photodiode, PD2, is used to record the reflected light from the metal films, and PD3 is used for recording the transmitted light. A sensitive power meter Gentec XLP12-3S-H2-D0, with

Figure 4.3: Inside of the Venteon One laser from Laser Quantum

a noise equivalent power of 0.5 μW, is used in order to calibrate the photodiodes that record reflectance and transmittance. Having calibrated photodiodes allows us to gain information about absorption of light by the thin metal films.

In order to align the three beams temporally and spatially, we need to monitor them on the metal film surface. To do so, a long working distance microscope objective (MO) is placed in the beam path of the signal and conditioning beams to find the overlap and optimize the spatial and temporal overlap each time after changing the metal film thickness, as seen in Fig. 4.5. Having the microscope objective in the beam path during the data collection however, results in unwanted background noise on the photodiodes from the conditioning beams. To avoid that, the objective is removed from the path before data collection. The microscope objective is mounted independently from the metal film so that removing it does not change the experimental conditions. This allows us to make sure that the background from the conditioning beams on the PD2 and PD3 is minimal.

4.1.1 Ultrafast Ti:Sapphire laser

A Venteon One Ti:Sapphire laser from Laser Quantum is used as the source of ultrafast pulses. This is an 80 MHz repetition rate laser source with 3 nJ energy per pulse. The FTL

pulses have a pulse duration of 8 fs FWHM in intensity at the output of the laser. Figure 4.4 shows a schematic of the laser. M1 and M2 are on piezo stages and can be adjusted from the main laser control panel in order to align the beam path of the 532 nm pump laser. The elements named in blue are the intracavity elements. M3 and M4 are dichroic concave mirrors. M5–10 are flat mirrors, where M10 is the output coupler.

It is not usually needed to open the oscillator lid for alignment. The laser can usually be mode locked and the output can be optimized using the pump steering mirrors (M1 and M2) and laser pump power. If the laser performance cannot be optimized externally, due to for example extreme temperature or humidity fluctuations or simply as time passes, more fine tuning of the laser cavity is required in order to mode lock the laser or improve the laser output power. This cannot be done by only adjusting with M1 and M2 using the laser control panel, and we need to open the laser box and align the laser cavity. Extreme care is required when the laser box is open. This is because the sensitive optical elements are now exposed to dust in air. Also, one should be careful not to damage the elements in the laser box. Another important point is that the green pump laser light can easily burn a piece of paper that is usually used for alignment purposes. The resulting smoke from such event can damage the optical elements. So, extra care is required when aligning the laser cavity.

Only M7 and M10 mirrors can be adjusted in the laser cavity. Small adjustments of these mirrors improve the performance of the laser. M11–14 are steering mirrors to send the laser beam to the output aperture. The Ti:sapphire crystal is mounted on a motorized stage and is located between the focusing mirrors M3 and M4. In order to avoid damage to the crystal, from for example possible dust particles on it, the stage automatically readjusts the position of the crystal periodically.

4.1.2 GDD compensation

A combination of a pair of chirped mirrors, DCM-7 GVD-Mirror pair from Laser Quantum, and a pair of CaF_2 compensation wedges from Laser Quantum is used in our setup, as shown

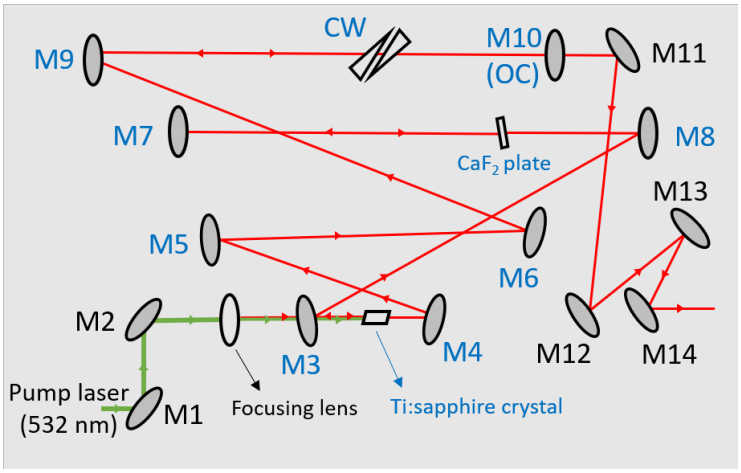

Figure 4.4: Schematic of the optical layout of the Venteon one laser. M1 and M2 are on piezo stages and can be adjusted from the main laser control panel in order to align the beam path of the 532 nm pump laser. Only M7 and M10 mirrors can be adjusted in the laser cavity.

in Fig. 4.1. The chirped mirrors have a high reflectively of $> 99.2\%$ and a GDD per pair of -120 fs^2. In our experiment, the beam reflects from each chirped mirror three times which results in -360 fs^2 of GDD. This is an overcompensation of GDD for our setup. In order to have the FTL laser pulses at the surface of the thin metal films, 1 mm of UVFS glass is added to the setup. The pair of compensation wedges are used in the beam path for fine tuning the GDD.

One should keep in mind that the angle of incidence on the chirped mirrors should be less than 10°, and the damage threshold of these mirrors is $\sim$0.05 J/cm^2. Aligning chirped mirrors is simpler than a compressor. However, as discussed before chirped mirrors do not usually provide a wide range of tunability of GDD. We are the sole users of our laser, and there is no need for us to have a wide range of GDD tunability because FTL or positively-chirped pulses are used for this experiment. The latter can be easily obtained by adding glass to the beam path.

4.1.3 Imaging the interference patterns

We need to be able to look at the focal spot of the three beams on the metal films. To do this, a 20X long working-distance microscope objective is used. It is focused on the surface of the metal films, and the image of the surface can be monitored using a CCD. To align the microscope objective, we first place a piece of bare glass as our sample. We place a fingerprint, or something similar, on one side of the glass, the side on which the metal coating would otherwise reside, and then ensure that the objective is properly focused on that "dirty" spot.

After aligning the objective, we find the spatial and temporal overlap of the three beams. To find the temporal overlap between the conditioning beams, we block the signal beam and change the delay of the DS1, shown in Fig. 4.1, in the beam path of one of the conditioning beams, until we see and fine tune the interference fringes on the CCD. We then block one of the conditioning beams and unblock the signal beam and find the temporal overlap of those two beams. Note that in this step, the three beams have the same polarization and one can see clear interference fringes once the overlap is found. Figure 4.5 shows a set of images of the fringe patterns recorded.

4.1.4 Imaging the focal spot of the laser beams

We need to measure the laser power, pulse duration, the spot size of the laser after being focused on the target, and the repetition rate of the laser in order to estimate the peak intensity on the metal films. Here we discuss how the latter is measured. The distance between the microscope objective and the CCD used for imaging determines how much of the active area of the CCD is covered by light. So, we need to have a method in order to extract the real focal spot size on our metal films from the CCD images. To do so, we replace our sample by a 1951 USAF resolution test target. The dimensions of the patterns on the calibration target are known. For example, the lines in the red box have a spatial density of 228 lines per millimeter. So, by imaging this target, we can find the scaling factor

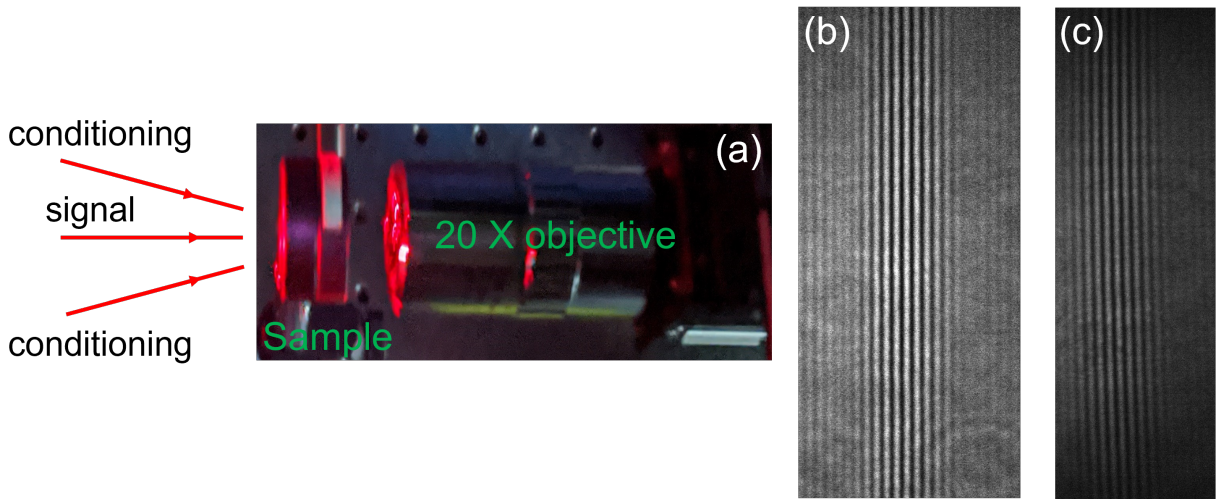

Figure 4.5: (a) Microscope objective imaging the surface of the metal films. (b) Observed fringes from the two conditioning beams. The separation between two constructive or destructive fringes is about 3μm. (c) Observed fringes from one of the conditioning beams and the signal beam.

that relates the focal spot of the laser on our metal films and the image recorded on the CCD. A calibration factor is found and used to estimate the laser focal spot size. Having a calibrated imaging system, we can now image the focal spot size of the laser of the two conditioning beams. We then use the spot size to estimate the laser peak intensity of the conditioning beams on the metal films. Figure 4.7 (a) and (d) shows the imaged laser focal spots of the two conditioning beams. Figure 4.7 (b,e) and (c,e) show the projection of the spot size on x and y axis, respectively.

4.2 Pulse characterization

As mentioned before, it is critical for this experiment that the pulse duration of the laser pulses is shorter than 15 fs. In this section, we discuss how τ is measured in order to make sure the shortest pulses are used in the experiment.

We use a Thorlabs' FSAC interferometric autocorrelator that can normally measure pulses longer than 40 fs. Figure 4.8 shows a schematic of the interferometric autocorrelator.

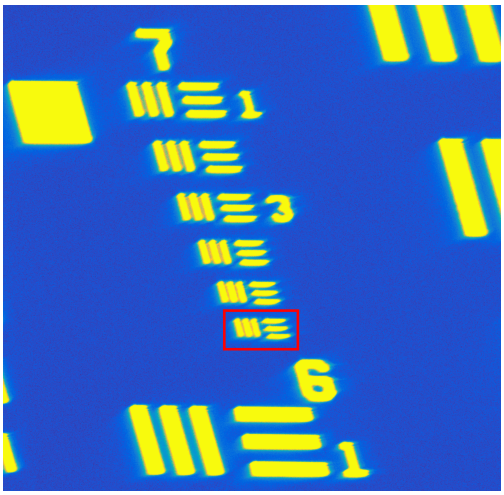

Figure 4.6: Image of a 1951 USAF resolution test target from our setup. For example, the density of the lines in the red box is 228 lines per millimeter. A calibration factor is found and used in order to estimate the focal spot size of the laser in the configuration used for this work.

The optical configuration of it is similar to but slightly more complicated than a Michelson interferometer. For alignment, the light from the two arms should be on top of each other in the center of the alignment target. The alignment target is an IR card that makes it easy to see the dim light reflected from the two arms and directed to it for alignment purposes. M2 is on a linear stage. FM is a 90° off axis parabolic mirror that focuses the light from the two arms on the photodiode. In order to measure shorter τ, we need to pre-compensate for the GDD of the autocorrelator using a pair of chirped mirrors.

4.2.1 Pre-compensated interferometric autocorrelator

As mentioned before, the interferometric autocorrelator used in this experiment can measure pulses that are longer than 40 fs. If one wants to measure pulses shorter than that (in this case 8-10 fs), then the internal GDD of the autocorrelator starts to play an important role. This internal GDD can result in a pulse duration measurement far from the real value. However, because the optical elements that are used can support the bandwidth of the laser, it is possible to measure shorter pulses by managing the GDD of the optical elements.

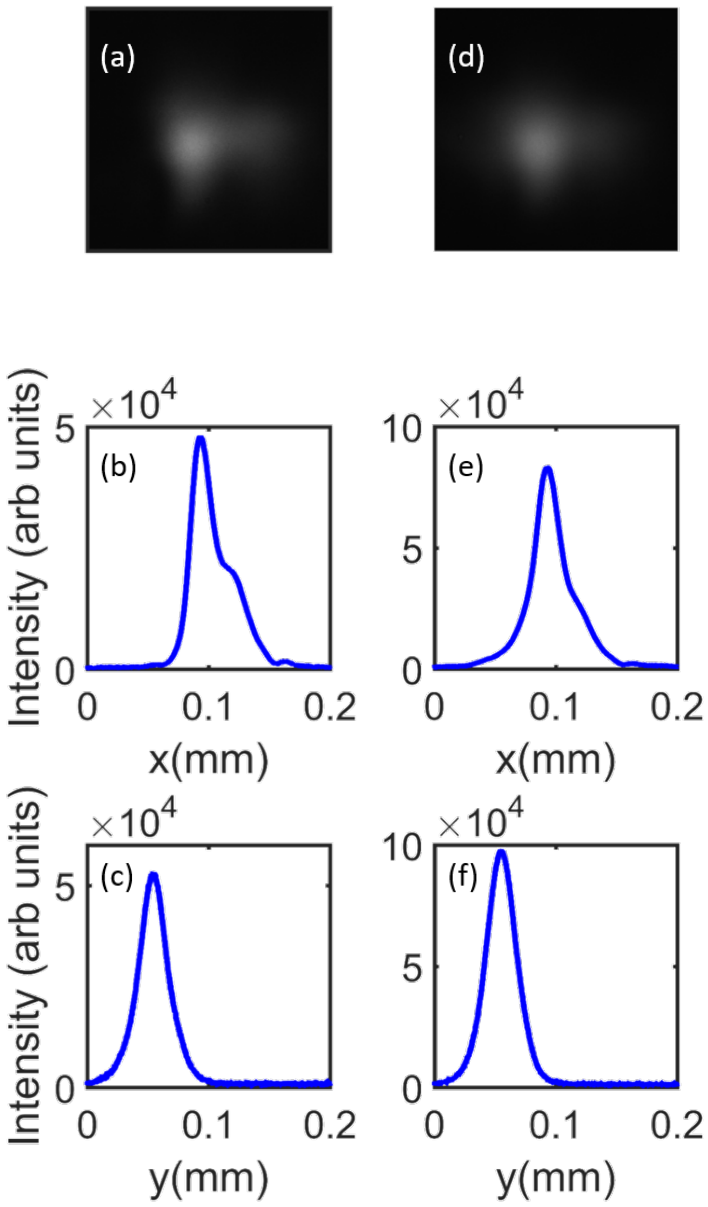

Figure 4.7: (a) and (d) The imaged focal spots of the two conditioning beams. (b) and (d) and (c) and (e) The projection of the spot size on x and y axis, respectively. This is the focus analysis for estimating the peak intensity of the conditioning beams.

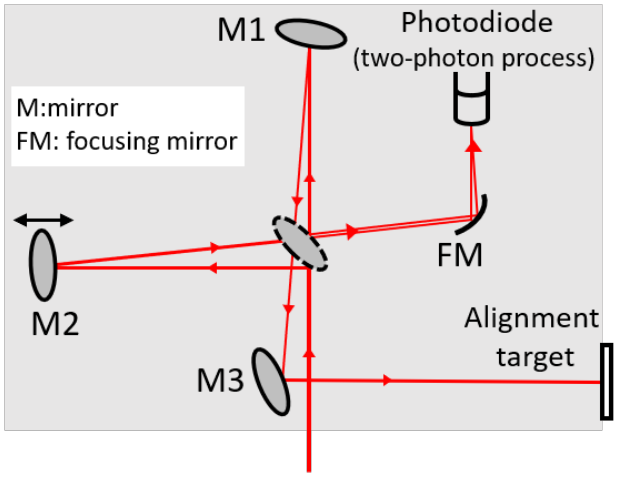

Figure 4.8: Schematic of the optical arrangement of the interferometric autocorrelator. For alignment, the light from the two arms should be on top of each other in the center of the alignment target. The alignment target is an IR card that makes it easy to see the dim light reflected from the two arms and directed to it for alignment purposes.

Moreover, the mirrors used in the setup before the autocorrelator have a nonzero GDD that should be compensated for. Also, it is important to consider the fact that for the central wavelength of ~800 nm, air introduces positive GDD that makes the pulses longer. One pair of chirped mirrors is used to compensate for the positive GDD discussed above. DCM-7 GVD-Mirror pair from Laser Quantum are used to pre-compensate, i.e., negatively chirp the pulses. The GDD per pair of these mirrors is -120 fs^2. The light bounces four times off each mirror in the pair, as seen in Fig. 4.10, which introduces -480 fs^2 negative chirp. By doing this, pulses with temporal duration of the order of 10 fs are successfully characterized. Note that glass is added using a wedge pair for GDD fine tuning. Adding the wedge pair to get the shortest pulse means that the pulses are negatively chirped after the chirped mirrors. The chirped mirror pair, interferometric autocorrelator, and the wedge pair are all mounted on a breadboard, which is called a pre-compensated interferometric autocorrelator. Having the setup on a breadboard makes the process of characterizing the pulses at different positions more convenient. Figure 4.11 shows the interferometric autocorrelator trace of these pulses from Venteon One. The τ extracted from the autocorrelation trace assuming a

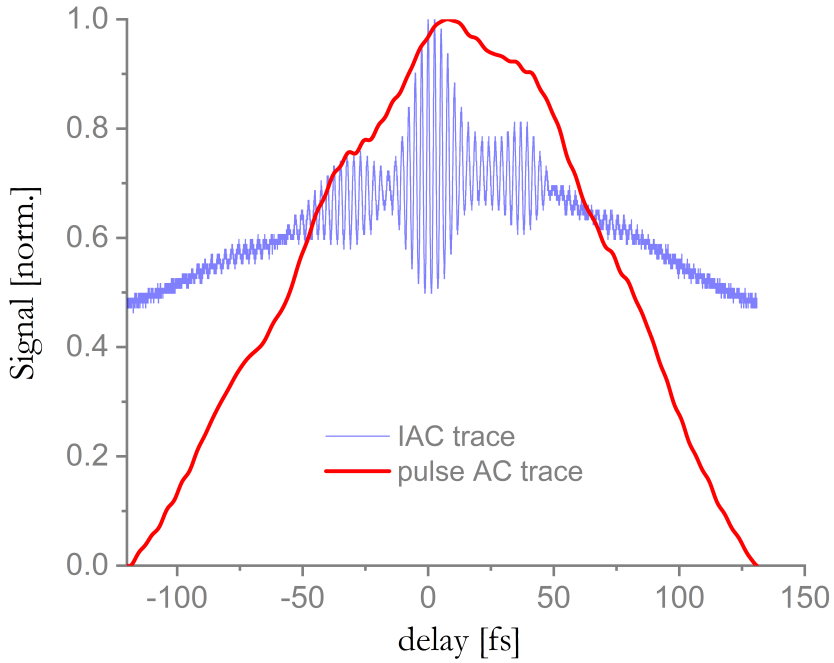

Figure 4.9: Characterization of a 8-10 fs pulse using the interferometric autocorrelator without pre-compensation. As can be seen, the pulse is excessively chirped due to the optical elements of the interferometric autocorrelator. The autocorrelation trace shows ∼100 fs FWHM pulse duration which is obviously not correct. Based on the interferometric autocorrelation trace, the pulse duration is much longer.

sech^2 temporal profile is 9.4 fs (full width half maximum [FWHM] in intensity).

A few more details about the pre-compensated interferometric autocorrelator can be useful. First, when aligning the setup, there was about 60 cm of air between the output of the laser and the entrance iris. Moreover, the mirrors used have a nonzero GDD. In this case, the two mirrors on the breadboard before the autocorrelator have a GDD of <5 fs^2 per mirror. There were five mirrors with a GDD of <5 fs^2 before the first iris (I1). Knowing all these details is important for measuring τ properly as a small amount of GDD can alter the pulse duration of a short pulse laser dramatically. As an example, adding $+100$ fs^2 of GDD to a 8 fs FTL pulse with a central wavelength of 800 nm will increase the pulse duration to about 50 fs. This amount of GDD corresponds to adding ∼2 mm of glass to the optical

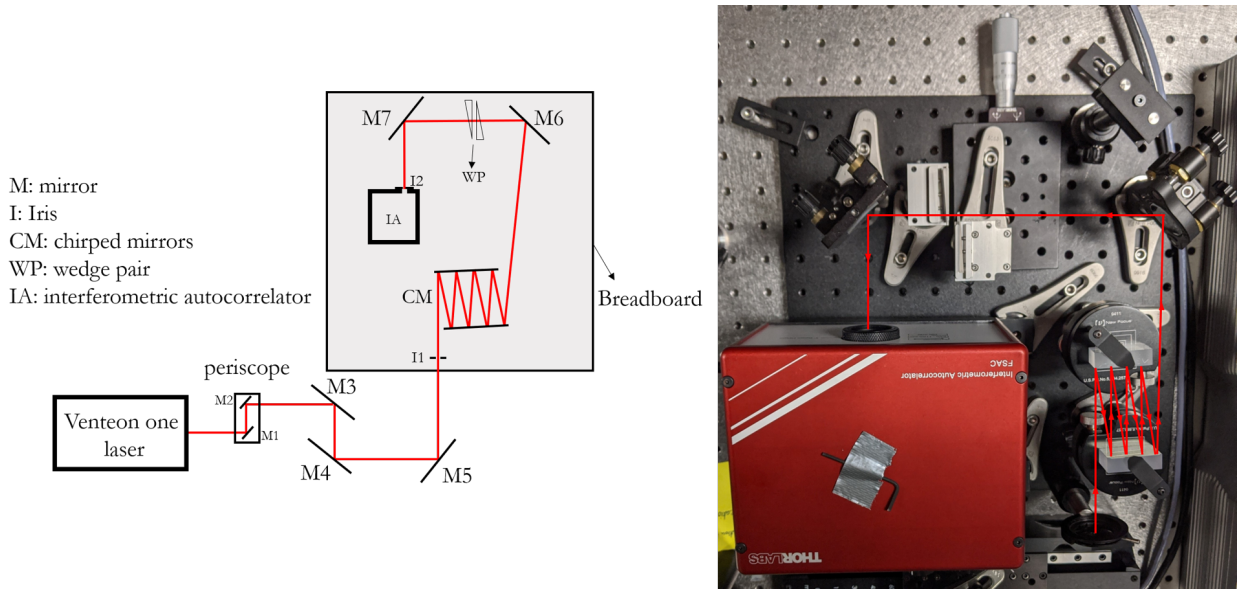

Figure 4.10: Schematic and a picture of the pre-compensated interferometric autocorrelator setup.

path. So, one must design the setup for performing the experiment with extreme care.

4.2.2 Estimating the GDD of optical elements in the setup

As was discussed in Section 4.2.1, managing the GDD added to the laser pulses is very important. The ideal case is that the pulse duration of the laser pulses in both arms are the same and shorter than ∼15 fs. That is why we carefully characterized the GDD of each optical element. This is particularly important for transmissive optics because the GDD added from transmission can significantly alter the pulse duration.

GDD added by the steering flat-mirrors

We estimate the GDD of each mirror to be about 4.5 fs^2. This is done by characterizing the pulses after bouncing off four mirrors and estimating the GDD of each mirror. Figure 4.12 shows the traces recorder after four mirrors. As there are a few mirrors in the setup before the two beams reach the interaction region as well as a few meters of air, we need a set of chirped mirrors to compensate for the extra GDD. Note that this is another pair of chirped

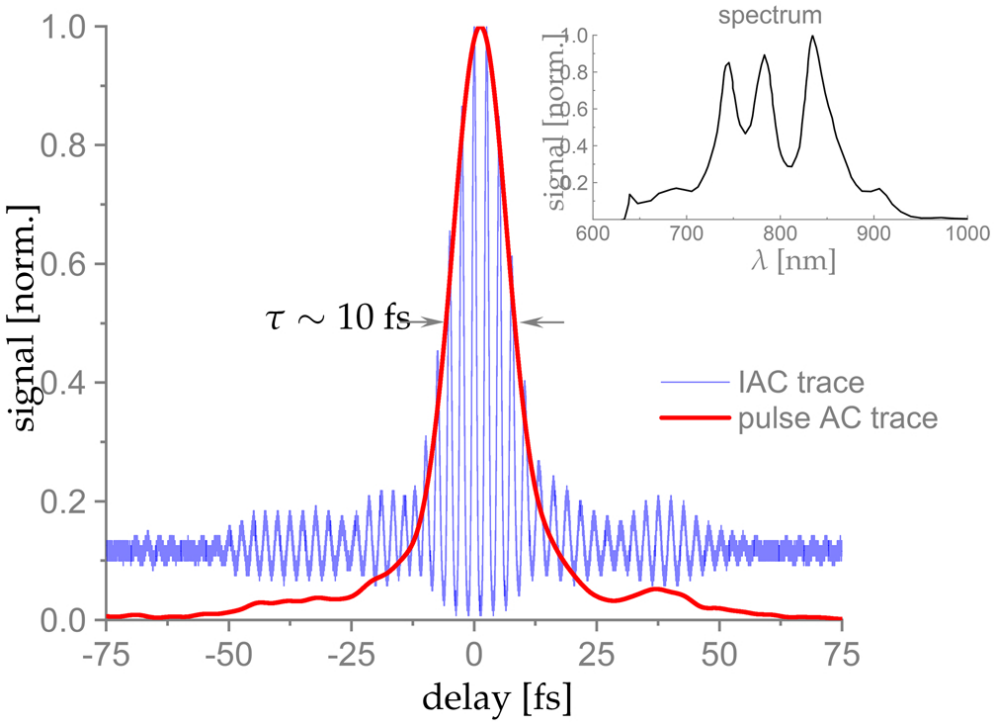

Figure 4.11: Characterizing the laser pulses used in the experiment before the thin metal films. IAC: Interferometric Autocorrelation trace. Pulse AC trace: the autocorrelation trace used to extract the FWHM laser pulse duration to be $\sim$ 10 fs. The inset of the figure shows the broadband laser spectrum.

mirrors in addition to the ones used to compensate for the GDD of the interferometric autocorrelator. Figure 4.1 shows a schematic of the whole setup.

GDD added by the parabolic mirrors

A parabolic mirror is used in each arm to focus the ultrafast laser pulses on the metal films. The estimated GDD of the parabolic mirrors, from a measurement, is about 20 fs^2, (see Fig. 4.13) which should be compensated for using the chirped mirrors.

GDD of the beamsplitters

There are two beamsplitters in the setup for generating the signal and the two conditioning beams, as shown in Fig. 4.1. In order to know the GDD added to the pulses following trans-

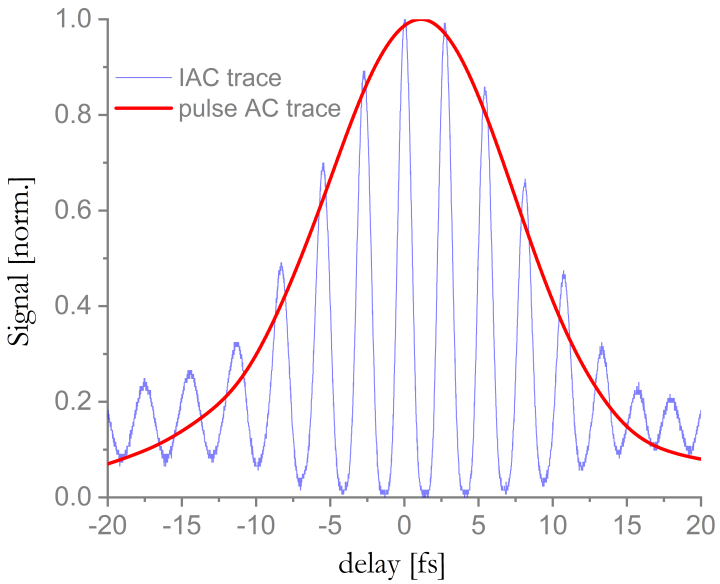

Figure 4.12: Characterizing the laser pulses after bouncing off four ultrafast optimized mirrors. IAC: Interferometric Autocorrelation trace. Pulse AC trace: the autocorrelation trace used to extract the FWHM laser pulse duration to be $\sim$ 12 fs

mission through the beamsplitters, the pulse duration after the beamsplitter is measured using the pre-compensated interferometric autocorrelator, as shown in Fig. 4.14. Comparing the pulse duration with and without the beamsplitter in the optical path suggests that there is $\sim$ 50 fs^2 GDD added by the beamsplitter when the beam is transmitted through it. This extra GDD should be matched in the other arm, where the beam is reflected from this beamsplitter.

Now that we roughly know the GDD added by each optical element, we can estimate how many bounces are required off the chirped mirrors. Considering all the elements discussed above, we end up with about 200-300 fs^2 GDD, an overestimate, added to the laser pulses right before the interaction region. Considering the negative GDD of the chirped mirrors, -120 fs^2, it is expected that 3-4 bounces per mirror result in a negatively chirped pulse. A pair of compensation wedges are then used for fine tuning and achieving FTL laser pulses at the interaction region.

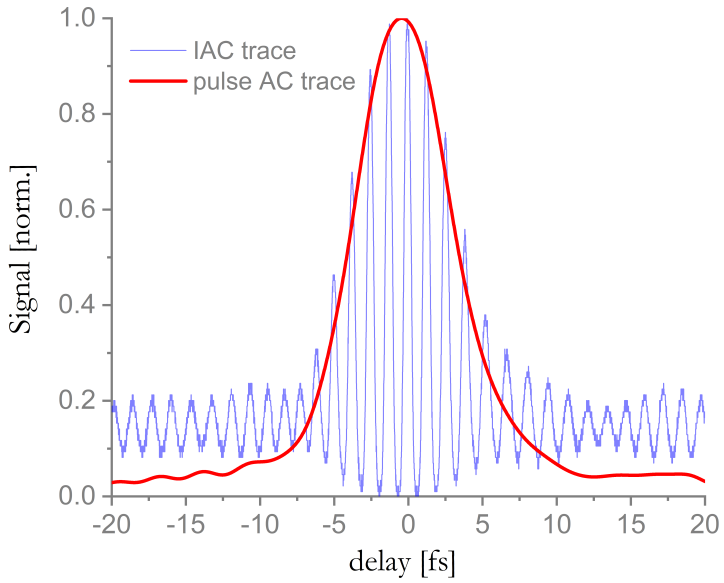

Figure 4.13: Characterizing the laser pulses after bouncing off three ultrafast optimized mirrors and one off-axis parabolic mirror. IAC: Interferometric Autocorrelation trace. Pulse AC trace: the autocorrelation trace used to extract the FWHM laser pulse duration to be $\sim$ 15 fs

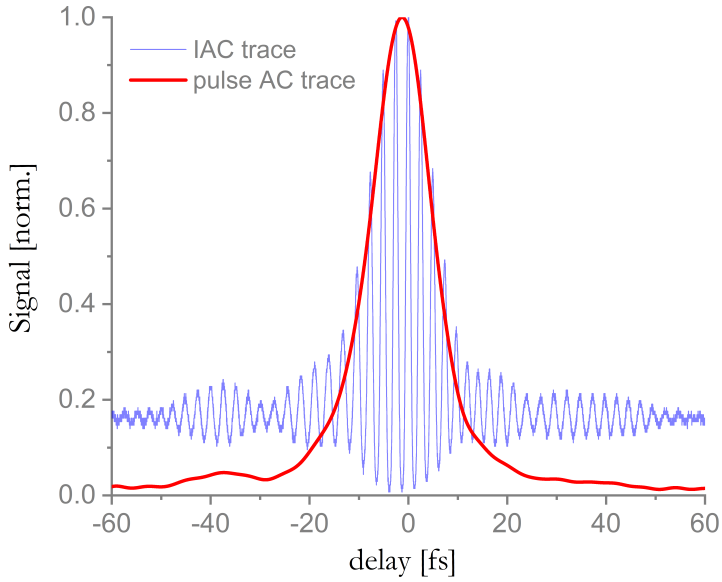

Figure 4.14: Characterizing the laser pulses after a beamsplitter. IAC: Interferometric Autocorrelation trace. Pulse AC trace: Pulse AC trace: the autocorrelation trace used to extract the FWHM laser pulse duration to be $\sim$ 16 fs

4.3 Calibrating the photodiodes

The goal is to have as much information as possible about the EIM effect on the optical properties of the thin gold films due to the presence of the conditioning beams. To do so, we need to measure reflection and transmission of the signal beam from the metal films using fast photodiodes. If the photodiodes are not calibrated, they show the voltage proportional to the signal light power, and it is not possible to find the absorption of the metal films and the effect of the EIM on it unless it is assumed that their response is identical. In other words, if one wants to extract information regarding the absorption of light from the recorded data, the photodiodes used in the experiment should be calibrated. On the other hand, we want to perform the experiments in a single shot manner. So, two fast photodiodes are calibrated in the laboratory. This approach is cheaper and more convenient than finding and purchasing two fast calibrated photodiodes.

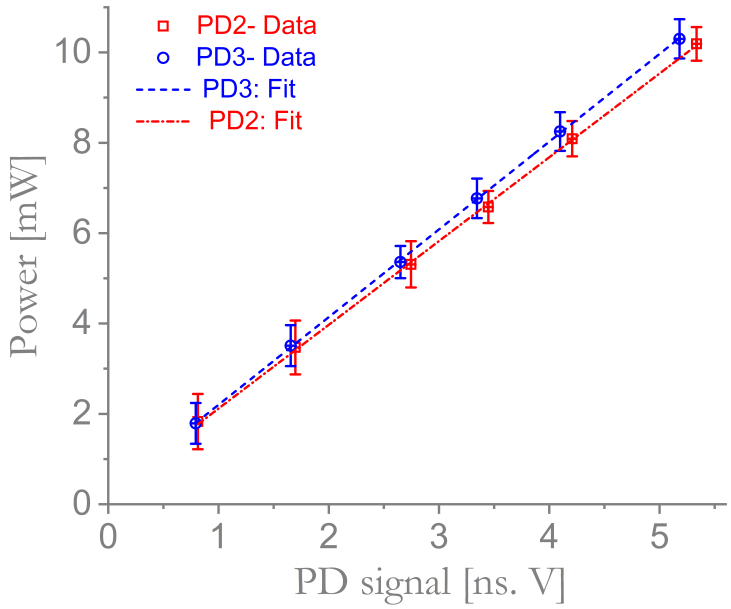

Figure 4.15: The calibration of the two photodiodes used to monitor the transmission of reflection of the gold metal films. PD2 and PD3 are used for recording the reflected and transmitted light, respectively.

A 50:50 (R/T) beamsplitter sends half of the beam to a photodiode, to be calibrated, and the other half to a sensitive power meter, Gentec XLP12-3S-H2-D0. The noise equivalent power of the power meter is 0.5 μW, which is orders of magnitude smaller than the power modulation we expect to measure. This allows us to calibrate the photodiodes precisely in order to measure the change in reflection and transmission due to the presence of the conditioning beams. Figure 4.15 shows the laser power as a function of the photodiode signal datapoints for the two photodiodes used for data collection. As can be seen in Fig. 4.15, although there is a small difference, the behavior of the two photodiodes is the same within the experimental error bars. This is not surprising as the same kind of photodiodes from the same company, Thorlabs, are used for data collection. The lines are linear fits to the datapoints for each photodiode. This linear dependence is then used in order to convert the signal of the transmitted and reflected light to laser power.

4.4 Data collection

After aligning the setup and ensuring that the pulses near the metal film are the shortest, data collection is began. For reflection data, a pick off mirror is used in order to collect the reflected signal beam from the metal film. The light is then focused on a fast photodiode (PD2), as seen in Fig. 4.1, using a lens. A lens is used here because after the signal beam is reflected off the metal film, pulse duration is not a concern, so transmissive optics can be used.

Collecting transmission data is more challenging. This is because there is background from the conditioning beams reaching the photodiode that collects transmission data due to the fact that a microscope objective is in the beampath. In other words, the microscope objective is needed to make sure that the spatial and temporal overlap are optimized. This results in unwanted noise for transmission data. In order to overcome this issue, the microscope objective is on a flip mount. In this way, temporal and spatial overlap is checked right before the start of the data collection process, and then the microscope objective is removed from the beam path. In this way, there is no background from the conditioning beams on the photodiodes used for data collection, as shown in Fig. 4.20.

For both reflection and transmission data collection, three data sets are recorded for each thickness of the metal film. Each data set consists of three photodiode signals which are reflection (PD2), transmission (PD3), and the monitor (PD1) signal. Having a monitor signal is important for analyzing data, as it will be discussed later. Also, it is better not to trigger the oscilloscope, Tektronix MDO3054, using the reflected or transmitted signals as the amplitude of them changes by changing the thickness of the metal film. The monitor signal on the other hand, is recorded close to the laser source. This signal is independent of the metal film thickness, and it is only correlated with the output of the laser and its possible fluctuations. So, the oscilloscope is triggered using the monitor signal.

The reflection and transmission of the signal beam are first recorded in the presence of the conditioning beams. See Fig. 4.16 for a schematic of the data collection process.

We should make sure that there is no background from the conditioning beams on the photodiodes. To check that, we block the signal beam and check to see that the reflection and transmission photodiodes produce no signal. The conditioning beams are then blocked,

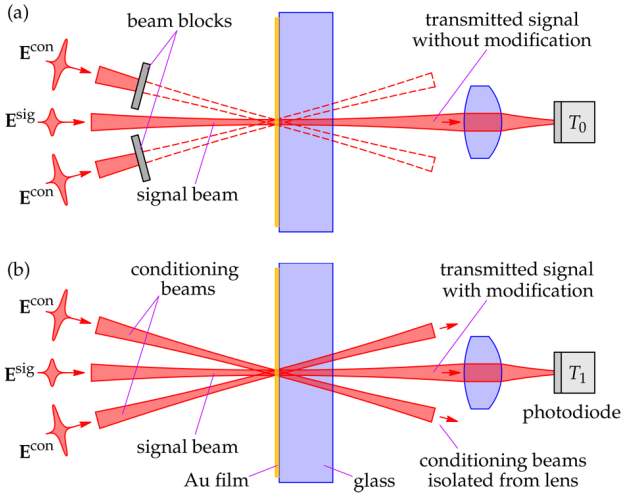

Figure 4.16: Schematic of the procedure used to search for a change of the transmittance of the film due to EIM. In (a), the conditioning beams are blocked from reaching the film and photodiode measures the transmittance of signal beam, T_0. In (b), the same measurement is performed except with the conditioning beams illuminating the film simultaneous with the signal beam. The photodiode again responds only to the signal beam, but may have a different response, T_1, if EIM occurs.

and the reflection and transmission of the signal beam is recorded. This is required so that we can compare the reflection and transmission of the metal film with and without the presence of the conditioning beams. Another data set is also collected in which the signal beam is blocked while conditioning beams are not blocked. We make sure that there is no background on the photodiode when the signal beam is blocked. Removing the microscope objective before data collection works in the way we intended. There is a difference between the case in which the conditioning beams are present and when they are blocked in the transmission of the signal beam, which is the evidence of the EIM effect.

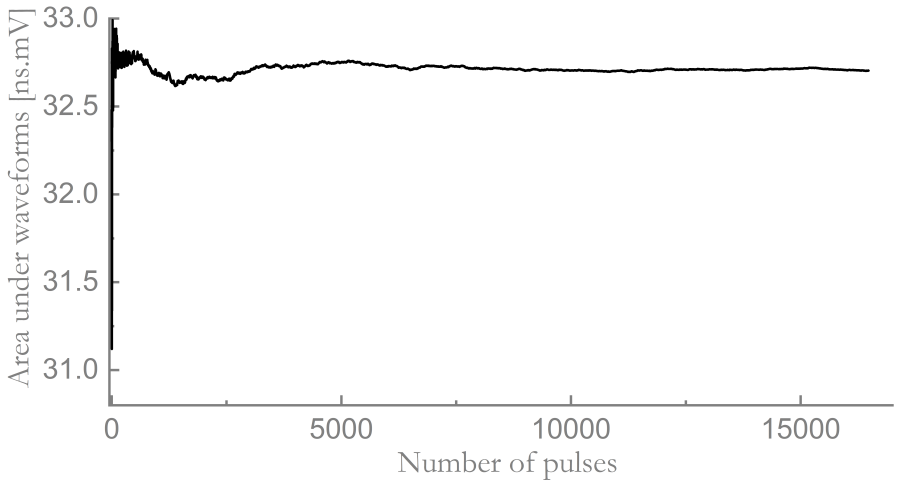

Figure 4.17: The stability of the laser recorded by PD1. The plot shows the integral of the output waveform from the monitor photodiode as a function of number of pulses. After averaging over enough pulses, the fluctuations in the signal diminish. The standard deviation of the data is ~ 0.015 %.

4.4.1 Triggering the oscilloscope

The output of the PD1 is used for two purposes. It is from a reflection from one of the optical elements in the setup, as seen in Fig. 4.1. PD1 is close to the laser, which allows us to monitor the power fluctuations of the laser source. This is important as we should know if there is a significant power fluctuation when recording the signal beam with or without the conditioning beams as this affects the outcome of the experiment. The power fluctuation of the laser source is measured to be $\sim$0.015%, as shown in Fig. 4.17. PD1 serves another purpose as well. We should trigger the data collection instrument, in this case an oscilloscope. Also, the trigger should be independent of the signals that are recorded so that a possible change in the signal, due to the presence of the conditioning beams for example, does not affect whether that signal is recorded or not. The output of PD1 satisfies both conditions. It is much closer to the laser than PD2 and PD3, and it is independent of the alignment of the off-axis parabolic mirrors, metal film thickness or position, and anything else that can affect the signal beam. So, it is used to trigger the data collection process.

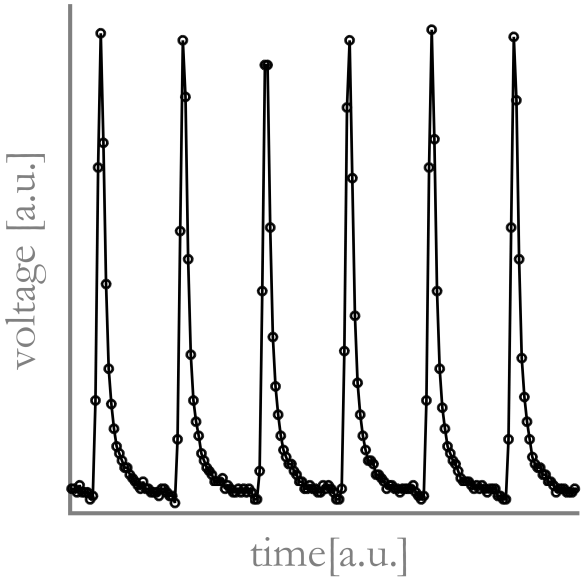

Figure 4.18: An example of a few waveforms recorded by PD2 from the laser. The open circles are the points recorded by the oscilloscope to generate the waveform.

4.5 Data analysis

The pulse train of PD2 and PD3 are used for data analysis if there is no significant laser power change recorded by PD1. Figure 4.18 shows an example of a few laser pulses recorded using PD3. Two methods are discussed for data analysis in the next sections. For both of these methods, the peaks of the waveforms recorded need to be determined. A Matlab code is used for data analysis. Matlab includes a peak finding function that can be used for the analysis of our data. This algorithm simply finds the local maxima of the input signal. Figure 4.19 shows an example of the output of this function. As can be seen, while it can effectively find peaks, some points with very small voltage are also local maxima and determined to be peaks. In order to eliminate these false peaks, a threshold, the red dashed line, is defined in the code so that any peak detected with a voltage below the threshold is ignored. We should be careful when defining this threshold. This is because the magnitude of the photodiode signal is different for each thickness of the metal film. Thinner metal films have higher transmittance and lower reflectance for example, so the threshold needs to be

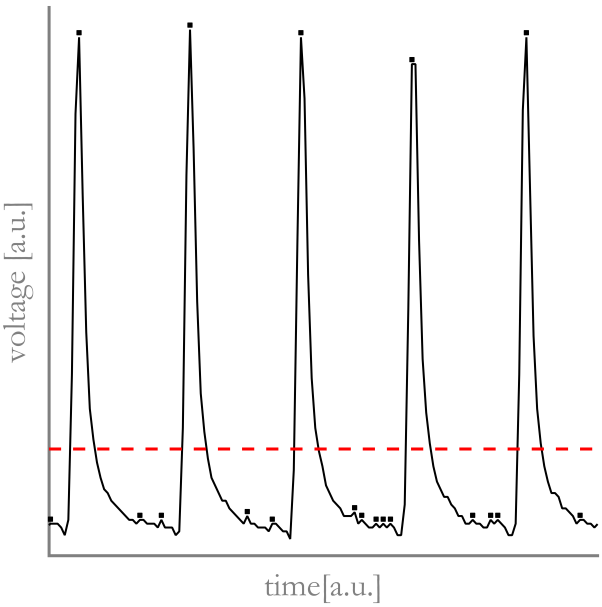

Figure 4.19: An example of the output of the peak finding function in Matlab. The squares show the peaks that has been found by Matlab. Note that a threshold, the red dashed line, is defined to eliminate any local maxima that are not meaningful peaks in our analysis.

determined for each thickness carefully. In the next step, the waveforms are reconstructed. We know the position of the peak of the waveforms and the approximate width of each one of them. These points are then used to define the waveform. This allows us to reconstruct the waveforms and average them one by one. Note that this eliminates any effect from possible jitters in the signal as the peak of each waveform is found separately. Moreover, it also suppress the effect of the small noise present in the time between two signals.

It is worth mentioning that a faster way for data analysis is to find one arbitrary peak, then find an appropriate window around that peak and use that window to define the other waveforms. This is possible because the temporal separation between the laser pulses is 11.5 ns. However, this method has a drawback. There might be some jitter in the data. This means that having just a time window does not provide us with accurate results. That is why this method is not used for data analysis.

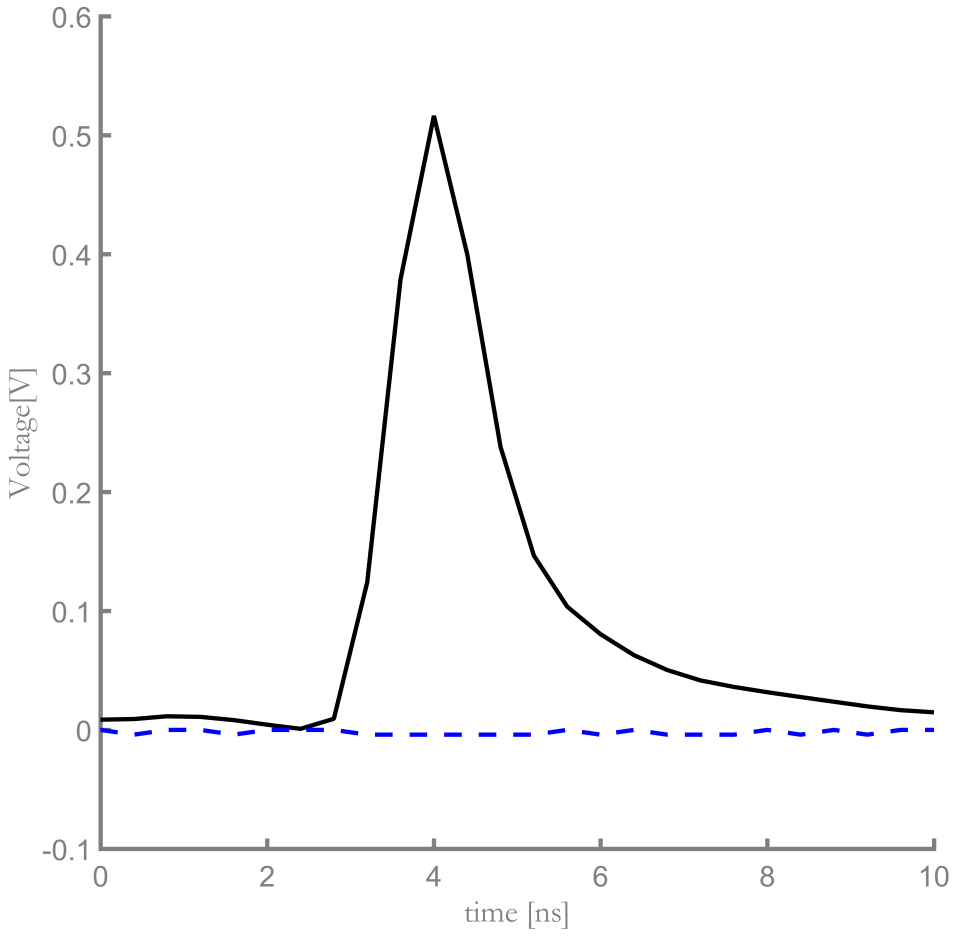

Figure 4.20: Black: An example of reconstructing the waveform using the proper peaks found in the analysis process. Blue: The photodiode output when the signal beam is blocked. This shows that no noise from the conditioning beams affect the photodiode signal.

4.5.1 Data analysis based on the peak value of each waveform

Now that the real peaks are separated in the data from noise, peak values can be used in order to find the transmittance and reflectance of the metal films. One way to look at the data is to find the peak of each signal waveform and use that value. For example, one can compare this peak value in the presence of the conditioning beams and when they are blocked. While this method might be faster, it can be less accurate. Just as an example, consider the hypothetical case shown in Fig. 4.21. This is the same waveform as shown in Fig. 4.20 but with artificial noise added to it that adds a narrow peak to the data. This sharp peak can come from an unknown noise source. The point assigned as the peak of this waveform using a peak detecting algorithm will be larger than the real peak. The relative difference in the peak value of Figs. 4.20 and 4.21 is $\sim$15%. Note that this difference is very large as we exaggerate in the magnitude of the artificial error added to the data to convey the point. This will result in possible incorrect conclusions if we do not average enough pulses to suppress the effect of this kind of noise. So, one should find a more reliable data analysis method.

4.5.2 Data analysis based on the area under each peak

If one finds the area under the waveform in Fig. 4.21, the sharp peak will have a much smaller contribution as it is relatively narrow. The relative difference in the area of Figs. 4.20 and 4.21 here is $\sim$3%. Again, averaging many laser pulses can suppress this error, but the important point is that in this case, less averaging is required. This makes the data analysis more accurate and less time consuming.

So, a better way to analyze the data is to find the area under each waveform, convert it to the power read by the photodiode using the calibration factors, and then proceed. This is a better method since finding the area under a curve is more precise than using the peak of the waveform.

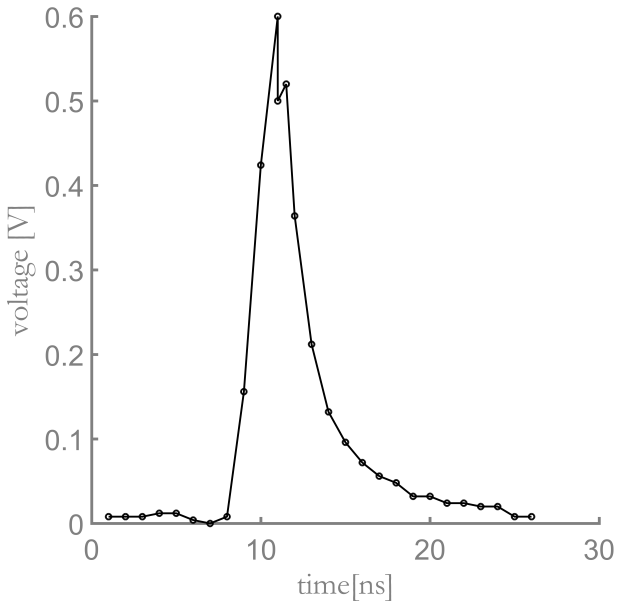

Figure 4.21: An example of reconstructing the waveform using the proper peaks found in the analysis process with added artificial noise.

4.6 Convergence of the data analysis

PD2 and PD3 record many pulses of the signal beam with and without the presence of the conditioning beams. One question is that what is the minimum number pulses to average over in order to minimize the effect of the noise from different sources in the experiment. Figure 4.22 shows the integral of the waveforms of a typical pulse train as a function of number of pulses recorded by PD3. This signal represents the stability of the whole setup as PD3 is the furthest photodiode from the laser. The fluctuations after averaging over 2000 pulses is ~ 0.02 %.

4.7 Error analysis

Since the effect of the presence of the conditioning beams is weak based on the theoretical model, calculating the experimental error bars is crucial. This is because it is possible that the observed modulation due to conditioning beams is smaller than the calculated error

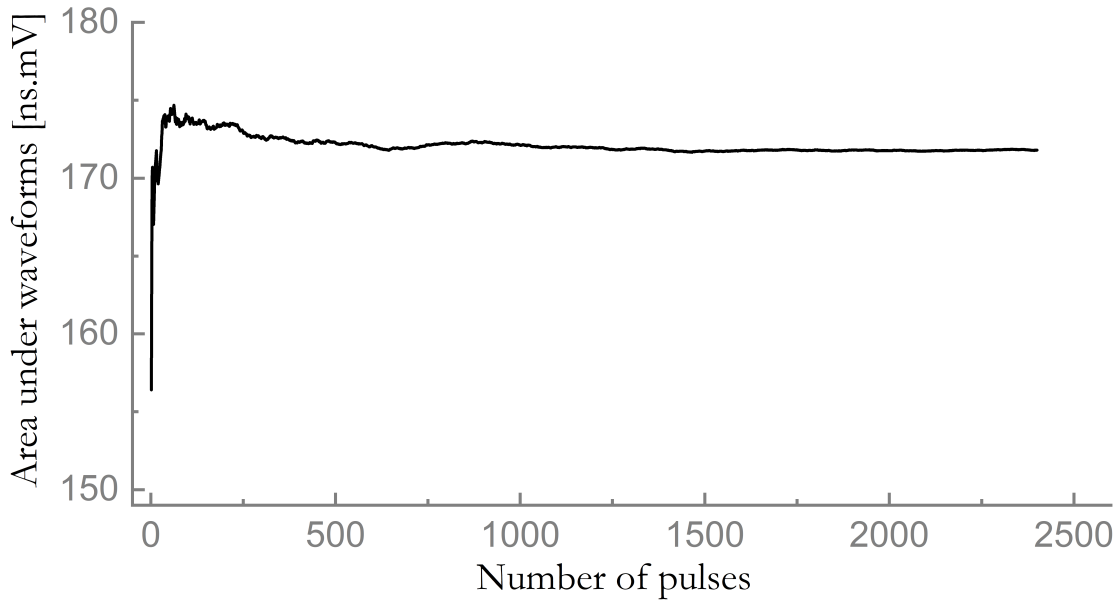

Figure 4.22: Convergence of the signal. The fluctuations after averaging over 2500 pulses is ∼0.02%. In the data analysis, we usually average over 2000 laser pulses or more in order to keep the standard deviation of the signal small.

bars. In this case, one cannot conclude that the observed effect is real. Note that the power recorded by the calibrated photodiodes is $P_{0,1}^{\text{tra}} = I_{0,1}^{\text{tra}}\mathcal{A}$, where $\mathcal{A}$ is the area of the photodiode.

4.7.1 Error associated with ΔT and ΔR

As discussed before, the change in transmittance and reflectance, ΔT and ΔR, of the signal is found for each metal film thickness. Let's calculate the error bar in ΔT first. We know that $\Delta T = \frac{I_1^{\text{tra}} - I_0^{\text{tra}}}{I_0} = \frac{P_1^{\text{tra}} - P_0^{\text{tra}}}{P_0}$. So, first, the statistical error bars in $P_1^{\text{tra}}, P_0^{\text{tra}}$ and P_0 are found. Having these statistical error bars allows us to calculate the error bar in the transmittance modification. The values of P_1^{tra} and P_0^{tra} are found by calculating the integral under the waveforms that are recorded by the photodiode. As discussed before, the average over many thousands of laser pulses is used in order to find them. This means that the standard deviation of P_1^{tra} and P_0^{tra}, which are the statistical error bars δP_1^{tra} and δP_0^{tra}, can

be determined. In order to find δP_0, the laser power is recorded using a power meter, and the standard deviation is calculated. Having δP_1^{tra}, δP_0^{tra}, and δP_0, we can now propagate the error bars in order to find the error of calculating $\alpha = \frac{P_1^{\text{tra}} - P_0^{\text{tra}}}{P_0}$. The general form for calculating this error bar is

$$(\delta\alpha)^2 = (\frac{\partial\alpha}{\partial P_1^{\text{tra}}})^2(\delta P_1^{\text{tra}})^2 + (\frac{\partial\alpha}{\partial P_0^{\text{tra}}})^2(\delta P_0^{\text{tra}})^2 + (\frac{\partial\alpha}{\partial P_0})^2(\delta P_0)^2. \tag{4.1}$$

It is easy to see that $\frac{\partial\alpha}{\partial P_1^{\text{tra}}} = \frac{1}{P_0}$, $\frac{\partial\alpha}{\partial P_0^{\text{tra}}} = -\frac{1}{P_0}$, and $\frac{\partial\alpha}{\partial P_0} = -\frac{P_1^{\text{tra}} - P_0^{\text{tra}}}{P_0^2}$. So

$$\delta\alpha = \frac{1}{P_0}\sqrt{(\delta P_1^{\text{tra}})^2 + (\delta P_0^{\text{tra}})^2 + \frac{(P_1^{\text{tra}} - P_0^{\text{tra}})^2}{P_0^2}(\delta P_0)^2} \tag{4.2}$$

gives us the error bar in the transmittance change. Similarly, the error bar of the reflectance modulation ($\beta = \frac{P_1^{\text{ref}} - P_0^{\text{ref}}}{P_0}$) can be found to be

$$\delta\beta = \frac{1}{P_0}\sqrt{(\delta P_1^{\text{ref}})^2 + (\delta P_0^{\text{ref}})^2 + \frac{(P_1^{\text{ref}} - P_0^{\text{ref}})^2}{P_0^2}(\delta P_0)^2} \tag{4.3}$$

So, $\gamma = \frac{\Delta A}{P_0}$, where A is the absorption of the metal film, can be found to be

$$\gamma = -\Delta T - \Delta R, \tag{4.4}$$

and the error bar of γ is simply

$$\delta\gamma = \sqrt{\delta\alpha^2 + \delta\beta^2}. \tag{4.5}$$

4.7.2 Error associated with $\frac{P_1^{\text{tra}} - P_0^{\text{tra}}}{P_0^{\text{tra}}}$

As it will be discussed briefly in the next chapter, $\frac{P_1^{\text{tra}} - P_0^{\text{tra}}}{P_0^{\text{tra}}}$ is also used as another way to look at the experimental data. The process of finding the errors here is exactly the same as what was discussed before. The expressions for the errors are different, so we discuss how

they are found. To find the error bar, the average over many T_0 and T_1 signals is found and the standard deviation is calculated. Then the error bars are propagated as discussed here.

Again, the general form for calculating the error of $\alpha = \frac{P_1^{\mathrm{tra}} - P_0^{\mathrm{tra}}}{P_0^{\mathrm{tra}}}$ is

$$(\delta\alpha)^2 = (\frac{\partial\alpha}{\partial P_1^{\mathrm{tra}}})^2(\delta P_1^{\mathrm{tra}})^2 + (\frac{\partial\alpha}{P_0^{\mathrm{tra}}})^2(\delta P_0^{\mathrm{tra}})^2. \tag{4.6}$$

We find $\frac{\partial\alpha}{\partial P_1^{\mathrm{tra}}} = \frac{1}{P_0^{\mathrm{tra}}}$ and $\frac{\partial\alpha}{\partial P_0^{\mathrm{tra}}} = -\frac{P_1^{\mathrm{tra}}}{(P_0^{\mathrm{tra}})^2}$. So

$$\delta\alpha = \frac{1}{P_0^{tra}}\sqrt{(\delta P_1^{\mathrm{tra}})^2 + \frac{(P_1^{\mathrm{tra}})^2}{(P_0^{\mathrm{tra}})^2}(\delta P_0^{\mathrm{tra}})^2} \tag{4.7}$$

gives us the error bar in change in transmittance. Similarly, the error bar of the reflectance modulation ($\beta = \frac{P_1^{\mathrm{ref}} - P_0^{\mathrm{ref}}}{P_0^{\mathrm{ref}}}$) can be found to be

$$\delta\beta = \frac{1}{P_0^{\mathrm{ref}}}\sqrt{(\delta P_1^{\mathrm{ref}})^2 + \frac{(P_1^{\mathrm{ref}})^2}{(P_0^{\mathrm{ref}})^2}(\delta P_0^{\mathrm{ref}})^2} \tag{4.8}$$

These errors are used when discussing the effect of the conditioning beams on the transmittance and reflectance of the metal films.

Chapter 5

Experimental results

In this section, the main experimental results of this work regarding how the presence of the conditioning beams affects the optical properties of metals (the EIM effect) are discussed. The data is presented to show the difference of the transmission and reflection of the signal beam interacting with metal films with and without conditioning beams present. A change in the optical properties of metals is observed that is in qualitative agreement with the EIM model discussed in Chapter 3.

There are two ways that the collected experimental results are presented in a plot. Note that these are similar, with each having advantages and disadvantages. The first method gives a change of the photodiode signal, that represents the transmission and reflection peak of the signal beam, with and without conditioning beams. While this analysis method shows the presence of the EIM effect in the transmitted light, no information about the EIM effect on the absorption of light can be extracted from it. In order to study the possible EIM effect on the absorption of light, more work is done. This includes collecting data with carefully calibrated photodiodes. We also discuss a slightly different analysis method.

The experiments have been performed on two different metals, gold and platinum. While the experimental results on gold are rather complete, which helps us understand the EIM effect, the experimental results with platinum are preliminary. More work is required in the

future to complete the study of EIM in platinum.

5.1 EIM in gold

Gold is selected to avoid the issues introduced by sample oxidation mainly to rule out the possibility of surface plasmonic effects. Also, gold is highly reflective for the whole bandwidth of our laser [68], which makes it an ideal sample for the first proof-of-principle measurements.

5.1.1 First analysis method

The first analysis method is to plot $\frac{P_1^{\text{tra}}-P_0^{\text{tra}}}{P_0^{\text{tra}}}$ as a function of sample thickness. Note that in this case, the denominator does change as a function of thickness. This is because the reflectance and transmittance of thicker metal films are higher and lower, respectively. This analysis method is useful to study the change in reflectance and transmission but cannot be used for a possible change in absorption of light. We initially used this method to look at the data collected in the experiment. Then, the calibration of the photodiodes was included. Figure5.1 shows $\frac{P_1^{\text{tra}}-P_0^{\text{tra}}}{P_0^{\text{tra}}}$ as a function of sample thickness. There is a clear change in the light transmission due to the presence of the conditioning beams. Also, this change depends sensitively on the thickness of the sample. Both of these observations have been qualitatively predicted in the model presented for EIM.

5.1.2 Second analysis method

The second, and preferred method for discussing the result is by looking at $\Delta T = T_1 - T_0$ and $\Delta R = R_1 - R_0$. The only change here is that the denominator is P_0, which is the incident signal power on the sample. Note that P_0 does not depend on the sample thickness. It is measured using the two calibrated photodiodes in the setup. In order to do so, the reflected and transmitted signal beam from the glass substrate without a metal film is recorded. The

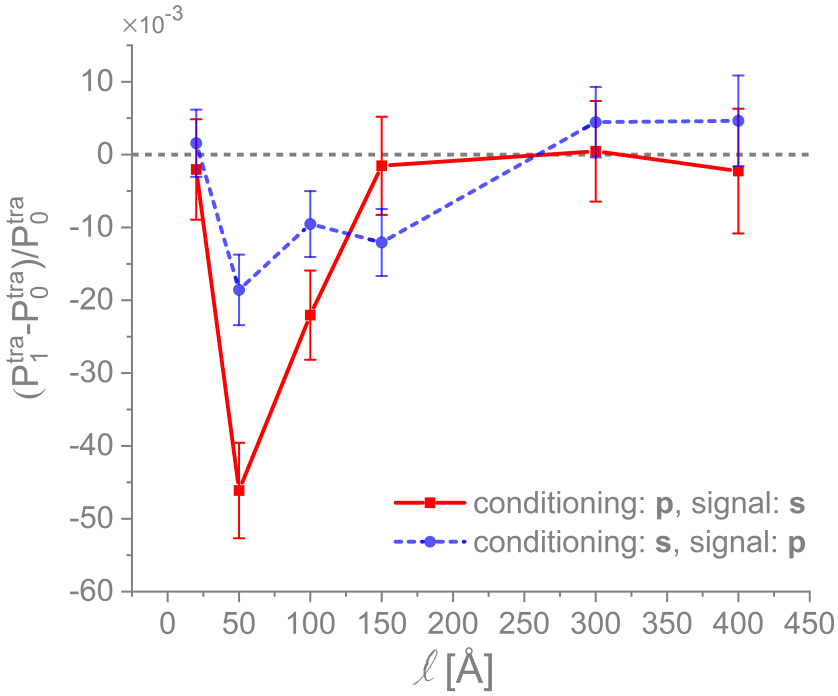

Figure 5.1: $\Delta R = R_1 - R_0$ as a function of sample thickness. The difference in transmission with and without the conditioning beams present is ΔT . The transmission of each sample when the conditioning beams are blocked is T_0. Note that T_0 is different for each sample thickness as the transmission is less for thicker films. This plot shows a clear change in the transmission of light due to the EIM effect with the two polarization combinations.

sum of the two measurements is the power of the signal beam P_0. The latter method is used because the denominator is constant. This aids the study of possible changes in the absorption of sample as will be discussed later.

We first focus on the blue curve in Fig. 5.2(a). This is for the case with the laser pulse duration of ∼10 fs and the peak intensity in the bright fringes of $\leq 10^{11}$ W/cm^2. The conditioning beams are p-polarized, and the signal beam is s-polarized. The transmission of light is smaller in the presence of the conditioning beams. As can be seen, ΔT depends sensitively on the sample thickness. The maximum change occurs at a thickness of 50 Å, which is the closest available sample thickness to the skin depth of gold at 790 nm [51].

ΔT is much smaller for thin and thick metal films, which can be qualitatively understood.

In the extreme case of no gold thin film, no modulation is expected as there are no free electrons to be redistributed due to the electric field of the conditioning beams. On the other hand, in thick films, compared to the skin depth, changing the skin depth by a few percent does not affect the overall transmission. In other words, metal films thinner and much thicker than the skin depth do not "see" the effect of the conditioning beams.

The polarization of the conditioning beams is such that plasmonic effects on light transmission [41, 46–49, 69–78] can play a role in the observed effect. However, plasmonic effects result in an enhancement of transmission. This is not the case in the presented results. Moreover, plasmonic effects are very sensitive to the sample thickness [41]. As discussed before, the optimum thickness for gold is ∼500 Å to see maximum plasmonic effects [41], so it is not expected to see strong plasmonic effects for the sample thicknesses we consider.

To double check the absence of enhanced transmission due to the plasmonic effects, the experiment is performed with the other possible crossed polarization combinations (signal/-conditioning: p/s). With this polarization combination, no plasmonic effects are expected to happen at all even if the experiment was designed to observe them. The result with 10 fs pulses is shown in Fig. 5.2(a) in blue. The observation of nonzero ΔT for *both* polarization combinations suggest that plasmonic effects are unlikely to explain these measurements.

As shown in Fig. 5.2(a), the theoretical and experimental results have very similar functional dependence on the film thickness. Figure 5.2(b) shows the experimental and theoretical results that are normalized to -1 so that it is easier to compare the general behavior of the two. The disagreement in overall magnitude of the curves in Fig. 5.2(a) is partially due to the fact that there is $< \pm 10$ Å error bar on the thickness of the metal films. Moreover, although other possible mechanisms such as what is reported in [19–31, 79–82] are not expected to play a role here, the EIM model is still a simple classical description of the observed phenomenon. From the experimental point of view possible uncertainties, such as estimating the peak pulse intensity, makes matching the experimental and theoretical results challenging. These all can result in the disagreement in the magnitude of the theoretical

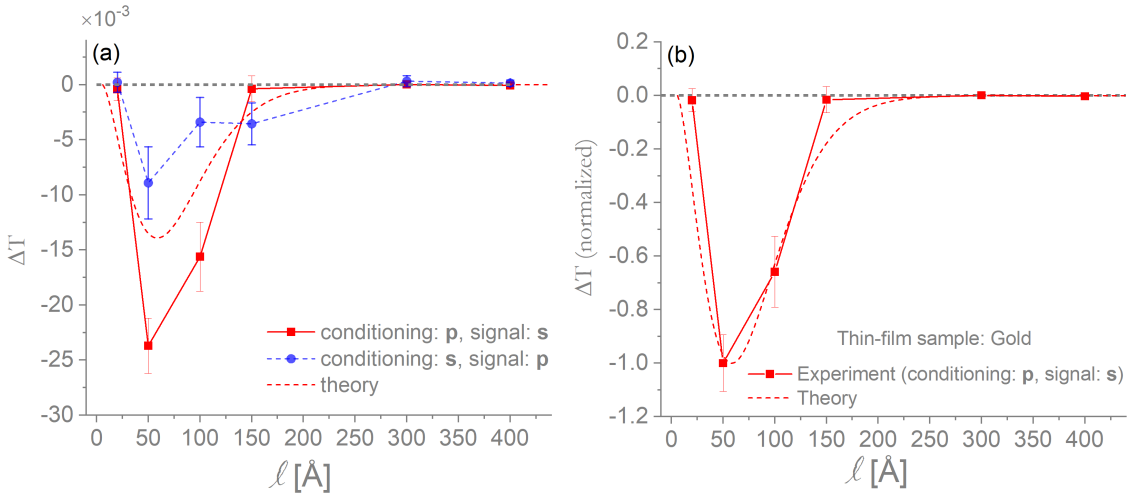

Figure 5.2: Measurements of EIM. In (a) is shown the change in transmittance ΔT as a function of sample thickness ℓ. Two cases are presented: In blue, the conditioning beams are s-polarized, while the signal beam is p-polarized. The solid red curve shows the opposite case, conditioning beams p-polarized and the signals s-polarized. These polarization directions are defined in Fig. 4.1(a). The red dashed curve in (a) is the theoretical prediction for ΔT for the latter polarization combination. In (b), the model and measurement data are re-plotted after normalizing each curve to -1 for the same polarization case as in (a). The good agreement here illustrates that the model and measurement share similar functional dependence on ℓ.

and experimental results of EIM.

The change in reflectance of the metal films is also found from the recorded experimental data which is shown in Fig. 5.3. This is important if one wants want to study the effect of the conditioning beams on the absorption of the gold films. We know that $T+R+A+S = 1$, where T is transmission, R is reflection, A is absorption, and S is scattering of light from the sample. Assuming that the change in thickness of the sample does not change the scattering behavior of it, we have

$$\Delta A = -\Delta R - \Delta T, \tag{5.1}$$

which means that recording the transmittance and reflectance of light provides us with information about the absorption of the sample.

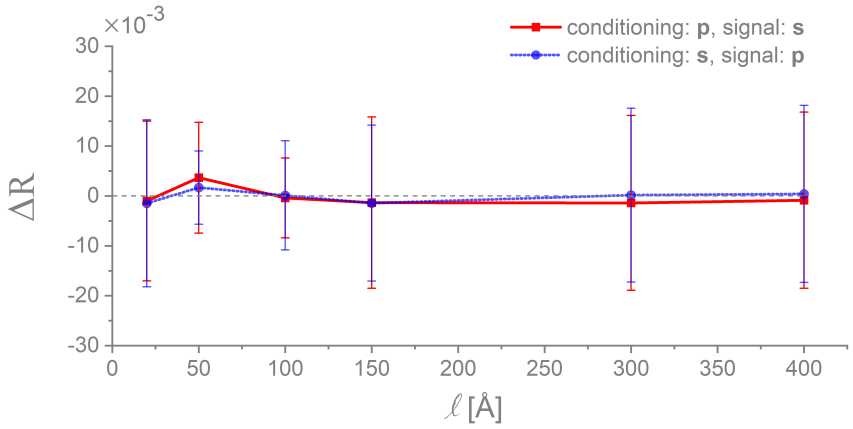

Figure 5.3: Measured dependence of ΔR as a function of sample thickness ℓ. In blue the conditioning beams are p-polarized and the signal beam is s-polarized. In red the conditioning are s-polarized and the signal beam is p-polarized. Note that any changes are within the measurement error bars.

The error bars on the ΔR are too large. This is because of the error of our experimental setup and the fact that the effect under study, if it exists, is very small. This means that we cannot conclude whether there is a modulation of the reflection due to the presence of conditioning beams given the error bars.

Measuring both transmission and reflection using calibrated photodiodes allows us to study the modification of the absorption of gold due to conditioning beams. As the change in reflection is not significant within the experimental error bars, the modification of absorption is simply the opposite of the transmission modulation which is shown in Fig. 5.4. One can argue that the presence of the conditioning beams temporarily transforms gold into a "better" conductor.

5.1.3 Pulse duration dependence of EIM in gold

The effect of pulse duration on the observed phenomenon is shown in Fig. 5.5. This is with both possible polarization combinations of the conditioning and signal beams. As was discussed before, it is expected for the ΔT to become smaller as the pulse duration

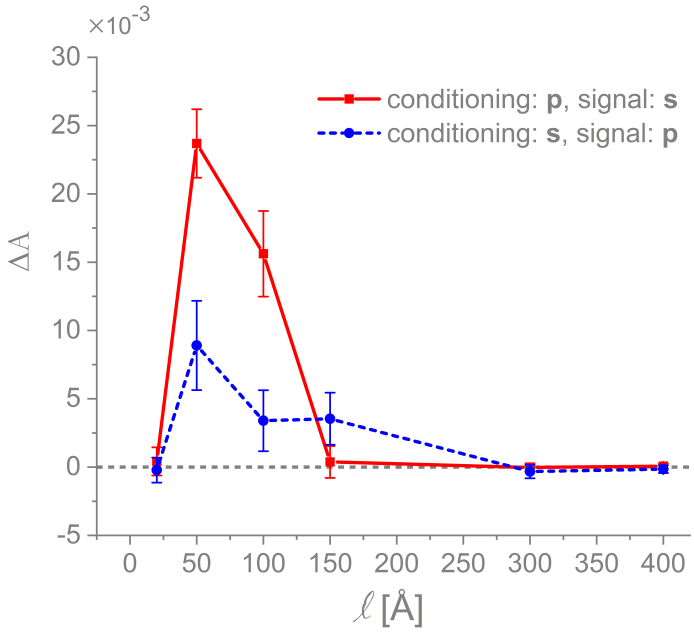

Figure 5.4: The effect of the presence of conditioning beams on the absorption of thin gold films. This is calculated from the reflection and transmission data. Due to the fact that the error bar on ΔR is too big, ΔA is simply equal to $-\Delta T$

becomes longer. This is because the relaxation time of electrons in gold is short, i.e., ∼15 fs. The experimental result is in agreement with the predicted behavior. Increasing the pulse duration suppresses the change in transmittance. We also perform the experiment with different laser pulse duration. As shown in Fig. 5.5, ΔT becomes smaller by increasing the laser pulse duration in agreement with the model.

5.2 EIM in platinum

The second metal used for this study is platinum. Gold and platinum have similar optical properties, and both do not oxidize easily, which is an important characteristic for the metal used in this study. The theoretical prediction of the EIM for gold and platinum was discussed before and can be seen in Fig. 3.16. Briefly, we expect to see similar EIM effects in platinum, i.e., a decrease in transmission of the signal beam in the presence of the

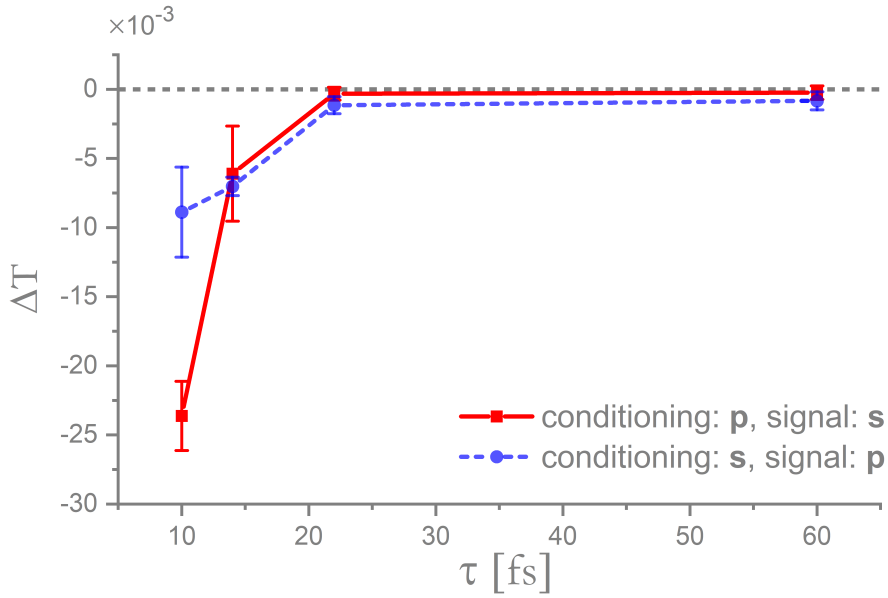

Figure 5.5: Measured dependence of ΔT as the pulse duration τ of the conditioning beams is changed. The sample here is a 50 Å thick gold. Glass is introduced in the beam to add varying amounts of GDD, which broadens the pulse duration. The model for EIM predicts $\Delta T \to 0$ as τ exceeds the metal's relaxation time τ_e; behavior that is seen here.

conditioning beams.

In order to estimate the laser peak intensity of the conditioning beams, we use the imaged focal spot size, as shown in Fig. 5.6. We estimate the peak intensity of the conditioning beams for the experiments on platinum to be about an order of magnitude smaller than the experiments involving gold. So, the peak intensity is $\leq 10^{10}$ W/cm^2.

5.2.1 EIM of transmission in platinum thin films

The EIM effect on the transmission of the signal beam is studied with the same method as was done for gold. As was mentioned, the intensity of the conditioning beams is lower than the case with gold films. Figure 5.7 shows a comparison between the theoretical and experimental results. Note that the model and measurement data are re-plotted after normalizing each curve to -1, as more work is required to understand the behavior of the EIM in platinum. The experimental effort with a 20 Å sample resulted in a positive ΔT,

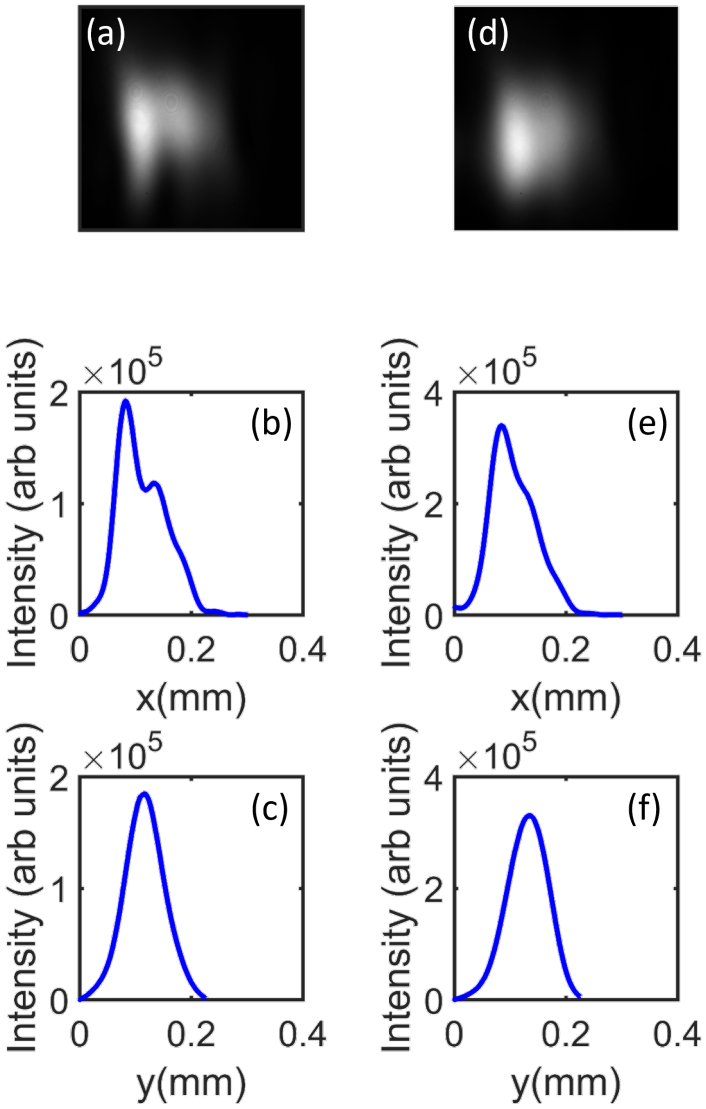

Figure 5.6: (a) and (d) the imaged focal spots of the two conditioning beams. (b) and (d) and (c) and (e) show the projection of the spot size on x and y axis, respectively. This is the focus analysis for estimating the peak intensity of the conditioning beams with platinum thin films.

and it is not shown here. This is mainly because the results for platinum are preliminary, and more work is required to ensure no significant error is present. The behavior in Fig. 5.7 is similar with what is reported of gold and qualitatively agrees with the theoretical results of the EIM effect for platinum. A decrease in transmission of the signal beam is observed due to the presence of the conditioning beams. The fact that the EIM effect here is smaller than gold could be partially due to the lower intensity of the conditioning beams.

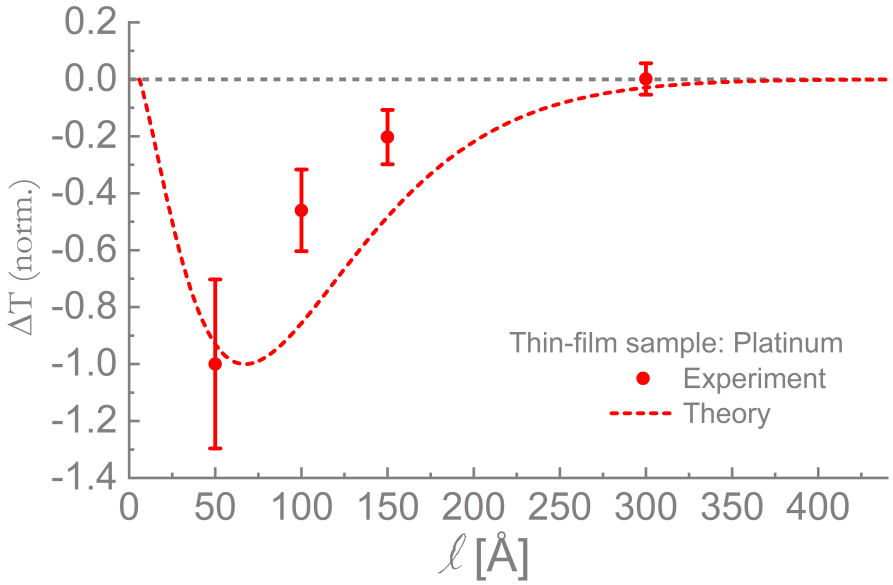

Figure 5.7: Measurements of EIM in platinum. In (a) is shown ΔT as a function of sample thickness ℓ. The data point of 20 Å sample thickness shows a drastic difference from what was reported for gold. More work is required to understand what causes this difference. In (b), the model and measurement data are re-plotted after normalizing each curve to -1 for the same polarization case as in (a). The data point of 20 Å sample is not shown here. There is a qualitative agreement between the model and the experimental results. However, more work is required to understand EIM in platinum.

5.3 Other possible effects

It is well known that the optical properties of metals can be temporarily altered by the thermalization of conduction electrons [19–31, 79–82]. After excitation, electrons will eventually thermalize with the lattice via, e.g., electron-phonon relaxation. This process happens over about a few hundred femtoseconds to a few picoseconds [19–31, 79–82]. So, we do not expect such slow processes to play a role in the observed effect.

Surface plasmonic effects are the other candidate for describing the observed phenomena that were briefly introduced in Chapter 2. For them to be excited [41, 46–49, 69–78], both momentum and energy conservation conditions should be satisfied [41]. This requires the excitation of surface plasmons to happen at an interface between the thin-film metal sample and a medium with $n > 1$, where n is the refractive index. For this condition to be satisfied, there should be a layer of oxide on the gold or platinum sample. But they do not oxidize easily, which makes the presence of plasmonic effects less probable. Also, plasmonic effects are very sensitive to the thin-film metal sample thickness [41]. For gold, the optimum thickness is $\sim$500 Å to see maximum plasmonic effects [41], which is substantially greater than the thickness in our study. From the experimental data, one can rule out the presence of the plasmonic effects as well. Surface plasmonic effect result in a decrease in the reflected light [41], which is not is observed.

Another possibility for the excitation of surface plasmons is the presence of sub-wavelength holes in metal films. The presence of such holes however, results in an enhancement of the transmittance [41, 46–49] rather than the reduction we see in the experiments. To further rule out plasmonic effects, the experiment is performed with two crossed polarization combinations (signal/conditioning: s/p and p/s). Because surface plasmons are excited on a smooth metal film only with p-polarized light [41], the observation of nonzero ΔT in Fig. 5.2(a) for both polarization combinations suggests that plasmonic effects are unlikely to be significant.

Chapter 6

Conclusion and future work

The possibility of altering the optical properties of thin metal films using few-cycle laser pulses with a central wavelength of 790 nm is explored. We call this phenomenon electromagnetically induced modification (EIM) of metal optical properties. It occurs due to the electron redistribution in the sample because of the presence of a standing wave pattern formed on the sample using the ultrafast laser. A theoretical model based on classical arguments is used to predict the behavior of EIM as a function of sample thickness. The transmission of a third signal beam is expected to decrease due to the presence of the conditioning beams. One can thus argue that the presence of the conditioning beams temporarily transforms gold into a "better" conductor.

In order to test this predicted phenomenon, a proof-of-principle experiment is performed on thin gold films. The experimental results are consistent with the prediction of the theoretical model of EIM. The experiments are done with two polarization combinations to argue that the presence of plasmonic effects is unlikely. Also, a pulse duration study reveals that the EIM effect decreases as the laser pulse duration increases, which is also in agreement with the model.

To further study EIM, preliminary studies of the effect with platinum are also presented. EIM is observed for platinum. This makes the possibility of any plasmonic effects further

less likely as they are very sensitive to the sample material. More work is planned to study and understand the EIM effect in platinum films.

For both gold and platinum, good qualitative agreement between the experimental and theoretical results is found. In other words, the functional behaviors of the experimental and theoretical results are the same, but the magnitudes are different, which we think is because of experimental uncertainties and the simplicity of the model used. More experiments are planned in order to further understand the EIM effect. This includes performing the experiment using another metal and changing the geometrical configuration of the standing wave pattern. We hope that these additional experiments help us understand the EIM effect even further.

To summarize, a new phenomenon is reported here that occurs at a timescale as short as $\sim$10 fs, that we hypothesize it is only due to the free electrons in the metal sample. This process makes the alteration of the optical properties of a gold and platinum thin film on a short timescale possible. We believe that it is the first time, to the best of our knowledge, that such phenomenon is reported.

This phenomenon could be observed, in principle, using any wavelength of light for which the metal film is highly reflective as long as no interband transitions occur. This means that EIM can have many possible applications. For example, one could consider more complex fringe patterns and the consequence their structures could have on ΔT. In other words, it may be possible to demonstrate a "dynamic metamaterial" where the optical properties of a metal film are adjustable externally. A simple version of this idea will be used to study the dependence of EIM on the fringe pattern. This will be done by simple changing the angle of incidence of the conditioning beams, which results in different fringe spacing that could alter the electron density redistribution in different ways. Moreover, the possibility of studying EIM using metal films other than gold and platinum will be explored. This is challenging as other possible candidates, such as silver for example, oxidize faster and easier than gold and platinum which is not desirable for studying EIM.

Bibliography

[1] S. Svanberg, *Atomic and molecular spectroscopy* (Springer-Verlag Berlin An, 2012).

[2] W. Demtröder, *Laser spectroscopy: Basic principles* (Springer, 2014).

[3] W. Demtröder, *Laser spectroscopy: Experimental techniques* (Springer, 2015).

[4] W. Demtroder, *Atoms, molecules and photons* (Springer, 2010).

[5] M. Shapiro and P. Brumer, *Quantum control of molecular processes* (Wiley-VCH, 2012).

[6] D. J. Tannor and S. A. Rice, "Control of selectivity of chemical reaction via control of wave packet evolution," The Journal of Chemical Physics **83**, 50135018 (1985).

[7] C. Kittel and P. McEuen, *Introduction to solid state physics* (Wiley, 2018).

[8] M. Ashcroft, *Solid State Physics: Revised Edition* (Cengage Learning, 2016).

[9] R. L. Olmon, B. Slovick, T. W. Johnson, D. Shelton, S.-H. Oh, G. D. Boreman, and M. B. Raschke, "Optical dielectric function of gold," Phys. Rev. B **86**, 235147 (2012).

[10] A. Schiffrin, T. Paasch-Colberg, N. Karpowicz, V. Apalkov, D. Gerster, S. Mhlbrandt, M. Korbman, J. Reichert, M. Schultze, S. Holzner, and et al., "Optical-field-induced current in dielectrics," Nature **493**, 7074 (2012).

[11] M. Schultze, E. M. Bothschafter, A. Sommer, S. Holzner, W. Schweinberger, M. Fiess, M. Hofstetter, R. Kienberger, V. Apalkov, V. S. Yakovlev, and et al., "Controlling dielectrics with the electric field of light," Nature **493**, 7578 (2012).

[12] G. Wachter, C. Lemell, J. Burgdörfer, S. A. Sato, X.-M. Tong, and K. Yabana, "Ab initio simulation of electrical currents induced by ultrafast laser excitation of dielectric materials," Phys. Rev. Lett. **113**, 087401 (2014).

[13] B. Nagler and et al., "Turning solid aluminium transparent by intense soft x-ray photoionization," Nature Physics **5**, 693696 (2009).

[14] X. Cui, C. Wang, A. Argondizzo, S. Garrett-Roe, B. Gumhalter, and H. Petek, "Transient excitons at metal surfaces," Nature Physics **10**, 505509 (2014).

[15] X. Cui, C. Wang, A. Argondizzo, S. Garrett-Roe, B. Gumhalter, and H. Petek, "Transient excitons at metal surfaces," Nature Physics **10**, 505509 (2014).

[16] M. Reutzel, A. Li, Z. Wang, and H. Petek, "Coherent multidimensional photoelectron spectroscopy of ultrafast quasiparticle dressing by light," Nature Communications **11** (2020).

[17] K. Kato, H. Mashiko, Y. Kunihashi, H. Omi, H. Gotoh, and K. Oguri, "Highly sensitive transient reflection measurement in extreme ultraviolet region for tracking carrier and coherent phonon dynamics," Opt. Express **28**, 1595–1602 (2020).

[18] M. Scalora, J. P. Dowling, C. M. Bowden, and M. J. Bloemer, "Optical limiting and switching of ultrashort pulses in nonlinear photonic band gap materials," Phys. Rev. Lett. **73**, 1368–1371 (1994).

[19] R. H. M. Groeneveld, R. Sprik, and A. Lagendijk, "Effect of a nonthermal electron distribution on the electron-phonon energy relaxation process in noble metals," Phys. Rev. B **45**, 5079–5082 (1992).

[20] L. Guo and X. Xu, "Ultrafast spectroscopy of electron-phonon coupling in gold," Journal of Heat Transfer **136** (2014).

[21] J. Hohlfeld, S.-S. Wellershoff, J. Gdde, U. Conrad, V. Jhnke, and E. Matthias, "Electron and lattice dynamics following optical excitation of metals," Chemical Physics **251**, 237258 (2000).

[22] R. H. M. Groeneveld, R. Sprik, and A. Lagendijk, "Femtosecond spectroscopy of electron-electron and electron-phonon energy relaxation in ag and au," Phys. Rev. B **51**, 11433–11445 (1995).

[23] S. K. Sundaram and E. Mazur, "Inducing and probing non-thermal transitions in semiconductors using femtosecond laser pulses," Nature Materials **1**, 217224 (2002).

[24] A. Giri and P. E. Hopkins, "Transient thermal and nonthermal electron and phonon relaxation after short-pulsed laser heating of metals," Journal of Applied Physics **118**, 215101 (2015).

[25] P. E. Hopkins, J. C. Duda, B. Kaehr, X. W. Zhou, C.-Y. P. Yang, and R. E. Jones, "Ultrafast and steady-state laser heating effects on electron relaxation and phonon coupling mechanisms in thin gold films," Applied Physics Letters **103**, 211910 (2013).

[26] B. Rethfeld, A. Kaiser, M. Vicanek, and G. Simon, "Ultrafast dynamics of nonequilibrium electrons in metals under femtosecond laser irradiation," Phys. Rev. B **65**, 214303 (2002).

[27] I. Razdolski, A. L. Chekhov, A. I. Stognij, and A. Stupakiewicz, "Ultrafast transport and relaxation of hot plasmonic electrons in metal-dielectric heterostructures," Phys. Rev. B **100**, 045412 (2019).

[28] Y. Sivan and M. Spector, "Ultrafast dynamics of optically induced heat gratings in metals," ACS Photonics **7**, 12711279 (2020).

[29] M. Ortolani, A. Mancini, A. Budweg, D. Garoli, D. Brida, and F. de Angelis, "Pump-

probe spectroscopy study of ultrafast temperature dynamics in nanoporous gold," Phys. Rev. B **99**, 035435 (2019).

[30] N. Del Fatti, C. Voisin, M. Achermann, S. Tzortzakis, D. Christofilos, and F. Vallée, "Nonequilibrium electron dynamics in noble metals," Phys. Rev. B **61**, 16956–16966 (2000).

[31] C.-K. Sun, F. Vallée, L. H. Acioli, E. P. Ippen, and J. G. Fujimoto, "Femtosecond-tunable measurement of electron thermalization in gold," Phys. Rev. B **50**, 15337–15348 (1994).

[32] A. V. Lugovskoy and I. Bray, "Ultrafast electron dynamics in metals under laser irradiation," Phys. Rev. B **60**, 3279–3288 (1999).

[33] P. W. Milonni and J. H. Eberly, *Laser physics* (Wiley-Blackwell, 2010).

[34] A. E. Siegman, *Lasers* (University of Science Books., 1986).

[35] O. Svelto, *Principles of lasers* (Springer, 2016).

[36] J.-C. Diels and W. Rudolph, *Ultrashort laser pulse phenomena* (Academic Press, 2014).

[37] A. M. Weiner, *Ultrafast optics* (Wiley, 2009).

[38] R. Szipöcs, K. Ferencz, C. Spielmann, and F. Krausz, "Chirped multilayer coatings for broadband dispersion control in femtosecond lasers," Opt. Lett. **19**, 201–203 (1994).

[39] M. Born and E. Wolf, *Principles of optics: electromagnetic theory of progagation, interference and diffraction of light* (Cambridge University Press, 2009).

[40] C. F. Bohren and D. R. Huffman, *Absorption and scattering of light by small particles* (Wiley, 1983).

[41] L. Novotny and B. Hecht, *Principles of Nano-Optics* (Cambridge University Press, 2006).

[42] S. A. Maier, *Plasmonics: fundamentals and applications* (Springer, 2007).

[43] "Near-field optics and surface plasmon polaritons," Topics in Applied Physics (2001).

[44] H. Moosmller, R. Giri, C. M. Sorensen, and M. J. Berg, "Black metal nanoparticles from abrasion processes in everyday life: Bicycle drivetrains and rock-climbing ropes," Optics Communications **479**, 126413 (2020).

[45] P. B. Johnson and R. W. Christy, "Optical constants of the noble metals," Phys. Rev. B **6**, 4370–4379 (1972).

[46] C. Genet and T. W. Ebbesen, "Light in tiny holes," Nature **445**, 3946 (2007).

[47] T. Thio, K. M. Pellerin, R. A. Linke, H. J. Lezec, and T. W. Ebbesen, "Enhanced light transmission through a single subwavelength aperture," Opt. Lett. **26**, 1972–1974 (2001).

[48] W. L. Barnes, W. A. Murray, J. Dintinger, E. Devaux, and T. W. Ebbesen, "Surface plasmon polaritons and their role in the enhanced transmission of light through periodic arrays of subwavelength holes in a metal film," Phys. Rev. Lett. **92**, 107401 (2004).

[49] U. Schröter and D. Heitmann, "Surface-plasmon-enhanced transmission through metallic gratings," Phys. Rev. B **58**, 15419–15421 (1998).

[50] D. J. Griffiths, *Introduction to electrodynamics* (Cambridge University Press, 2019).

[51] J. D. Jackson, *Classical electrodynamics* (Wiley, 2016).

[52] E. Hecht, *Optics* (Pearson, 2017).

[53] M. J. Berg and C. M. Sorensen, "A review and reassessment of diffraction, scattering, and shadows in electrodynamics," Journal of Quantitative Spectroscopy and Radiative Transfer **210**, 225–239 (2018).

[54] D. Gall, "Electron mean free path in elemental metals," Journal of Applied Physics **119**, 085101 (2016).

[55] E. G. Gamaly, A. V. Rode, B. Luther-Davies, and V. T. Tikhonchuk, "Ablation of solids by femtosecond lasers: Ablation mechanism and ablation thresholds for metals and dielectrics," Physics of Plasmas **9**, 949–957 (2002).

[56] X. Liu, D. Du, and G. Mourou, "Laser ablation and micromachining with ultrashort laser pulses," IEEE Journal of Quantum Electronics **33**, 17061716 (1997).

[57] R. W. Boyd, *Nonlinear optics* (Academic Press is an imprint of Elsevier, 2007).

[58] P. Wang, Y. Lu, L. Tang, J. Zhang, H. Ming, J. Xie, F.-H. Ho, H.-H. Chang, H.-Y. Lin, and D.-P. Tsai, "Surface-enhanced optical nonlinearity of a gold film," Optics Communications **229**, 425 – 429 (2004).

[59] B. E. A. Saleh and M. C. Teich, *Fundamentals of photonics* (Wiley-Interscience, 2007).

[60] D. I. Yakubovsky, A. V. Arsenin, Y. V. Stebunov, D. Y. Fedyanin, and V. S. Volkov, "Optical constants and structural properties of thin gold films," Opt. Express **25**, 25574–25587 (2017).

[61] F. Lacy, "Developing a theoretical relationship between electrical resistivity, temperature, and film thickness for conductors," Nanoscale Research Letters **6** (2011).

[62] D. Dayal, P. Rudolf, and P. Wißmann, "Thickness dependence of the electrical resistivity of epitaxially grown silver films," Thin Solid Films **79**, 193199 (1981).

[63] H. J. K. Kim, K. E. Kaplan, P. Schindler, S. Xu, M. M. Winterkorn, D. B. Heinz, T. S. English, J. Provine, F. B. Prinz, and T. W. Kenny, "Electrical properties of ultrathin platinum films by plasma-enhanced atomic layer deposition," ACS Applied Materials & Interfaces **11**, 9594–9599 (2019).

[64] S. Dutta, K. Sankaran, K. Moors, G. Pourtois, S. V. Elshocht, J. Bmmels, W. Vandervorst, Z. Tkei, and C. Adelmann, "Thickness dependence of the resistivity of platinum-group metal thin films," Journal of Applied Physics **122**, 025107 (2017).

[65] H. J. K. Kim, K. E. Kaplan, P. Schindler, S. Xu, M. M. Winterkorn, D. B. Heinz, T. S. English, J. Provine, F. B. Prinz, and T. W. Kenny, "Electrical properties of ultrathin platinum films by plasma-enhanced atomic layer deposition," ACS Applied Materials & Interfaces **11**, 9594–9599 (2019).

[66] A. Plech, V. Kotaidis, M. Lorenc, and J. Boneberg, "Femtosecond laser near-field ablation from gold nanoparticles," Nature Physics **2**, 4447 (2005).

[67] C. W. Luo, Y. T. Wang, F. W. Chen, H. C. Shih, and T. Kobayashi, "Eliminate coherence spike in reflection-type pump-probe measurements," Opt. Express **17**, 11321–11327 (2009).

[68] M. A. Ordal, L. L. Long, R. J. Bell, S. E. Bell, R. R. Bell, R. W. Alexander, and C. A. Ward, "Optical properties of the metals al, co, cu, au, fe, pb, ni, pd, pt, ag, ti, and w in the infrared and far infrared," Appl. Opt. **22**, 1099–1119 (1983).

[69] A. M. Dykhne, A. K. Sarychev, and V. M. Shalaev, "Resonant transmittance through metal films with fabricated and light-induced modulation," Phys. Rev. B **67**, 195402 (2003).

[70] T. W. Ebbesen, H. J. Lezec, H. F. Ghaemi, T. Thio, and P. A. Wolff, "Extraordinary optical transmission through sub-wavelength hole arrays," Nature **391**, 667669 (1998).

[71] H. Liu and P. Lalanne, "Microscopic theory of the extraordinary optical transmission," Nature **452**, 728731 (2008).

[72] S. Weis, R. Rivière, S. Deléglise, E. Gavartin, O. Arcizet, A. Schliesser, and T. J. Kippenberg, "Optomechanically induced transparency," Science **330**, 1520–1523 (2010).

[73] J. A. Hutchison, D. M. O'Carroll, T. Schwartz, C. Genet, and T. W. Ebbesen, "Absorption-induced transparency," Angewandte Chemie International Edition **50**, 2085–2089 (2011).

[74] S. G. Rodrigo, F. J. García-Vidal, and L. Martín-Moreno, "Theory of absorption-induced transparency," Phys. Rev. B **88**, 155126 (2013).

[75] N. Bonod, S. Enoch, L. Li, E. Popov, and M. Nevière, "Resonant optical transmission through thin metallic films with and without holes," Opt. Express **11**, 482–490 (2003).

[76] W. Cao, R. Singh, C. Zhang, J. Han, M. Tonouchi, and W. Zhang, "Plasmon-induced transparency in metamaterials: Active near field coupling between bright superconducting and dark metallic mode resonators," Applied Physics Letters **103**, 101106 (2013).

[77] X. Zhang, B. Sun, J. M. Hodgkiss, and R. H. Friend, "Tunable ultrafast optical switching via waveguided gold nanowires," Advanced Materials **20**, 4455–4459 (2008).

[78] J. Zhang, S. Xiao, C. Jeppesen, A. Kristensen, and N. A. Mortensen, "Electromagnetically induced transparency in metamaterials at near-infrared frequency," Opt. Express **18**, 17187–17192 (2010).

[79] H. J. Sielcken and H. J. Bakker, "Probing the ultrafast electron and lattice dynamics of gold using femtosecond mid-infrared pulses," Phys. Rev. B **102**, 134301 (2020).

[80] J. G. Fujimoto, J. M. Liu, E. P. Ippen, and N. Bloembergen, "Femtosecond laser interaction with metallic tungsten and nonequilibrium electron and lattice temperatures," Phys. Rev. Lett. **53**, 1837–1840 (1984).

[81] H. E. Elsayed-Ali, T. Juhasz, G. O. Smith, and W. E. Bron, "Femtosecond thermoreflectivity and thermotransmissivity of polycrystalline and single-crystalline gold films," Phys. Rev. B **43**, 4488–4491 (1991).

[82] H. E. Elsayed-Ali, T. B. Norris, M. A. Pessot, and G. A. Mourou, "Time-resolved observation of electron-phonon relaxation in copper," Phys. Rev. Lett. **58**, 1212–1215 (1987).